

**Electrical Engineering Department**

**Fayetteville, Arkansas**

**DESIGN OF A SWITCHED-RELUCTANCE MOTOR DRIVE  
FOR ELECTRIC PROPULSION**

Grant No. N00014-98-1-0617

Research Project 98PR05665 – 00

Period of Performance: May 01, 1998 – April 30, 2001

---

**Final Report –Part 1: Aspects of Switched Reluctance Motor Drive  
Application for Electric Vehicle Propulsion**

Shyam S.Ramamurthy and Juan Carlos Balda

University of Arkansas  
Department of Electrical Engineering  
3217 Bell Engineering Center  
Fayetteville, AR 72701 – 1201  
(501) 575-3005

Prepared for

Office of Naval Research  
Ballston Center Tower One  
800 North Quincy Street  
Arlington, VA 22217-5660

Program Officer: Mr. Terry Ericson

**DISTRIBUTION STATEMENT A**  
Approved for Public Release  
Distribution Unlimited

May 2001

**20020124 455**

**REPORT DOCUMENTATION PAGE**Form Approved  
OMB No. 0704-0188

Public reporting burden for this collection of information is estimated to average 1 hour per response, including the time for reviewing instructions, searching data sources, gathering and maintaining the data needed, and completing and reviewing the collection of information. Send comments regarding this burden estimate or any other aspect of this collection of information, including suggestions for reducing this burden to Washington Headquarters Service, Directorate for Information Operations and Reports, 1215 Jefferson Davis Highway, Suite 1204, Arlington, VA 22202-4302, and to the Office of Management and Budget, Paperwork Reduction Project (0704-0188) Washington, DC 20503.

**PLEASE DO NOT RETURN YOUR FORM TO THE ABOVE ADDRESS.**

|  |             |   |                                   |  |  |
|--|-------------|---|-----------------------------------|--|--|
| <b>1. REPORT DATE (DD-MM-YYYY)</b><br>17/01/2002   |             | <b>2. REPORT DATE TYPE</b><br>Final Report - Part 1 |                                   | <b>3. DATES COVERED (From - To)</b><br>May 1998 to December 2001 |  |
| <b>4. TITLE AND SUBTITLE</b><br>Final Report - Part 1: Aspects of Switched Reluctance Motor Drive Application for Electric Vehicle Propulsion.   |             |   |                                   | <b>5a. CONTRACT NUMBER</b>                                       |  |
|  |             |   |                                   | <b>5b. GRANT NUMBER</b><br>N00014-98-1-0617                      |  |
|  |             |   |                                   | <b>5c. PROGRAM ELEMENT NUMBER</b>                                |  |
| <b>6. AUTHOR(S)</b><br>S. S. Ramamurthy, J. C. Balda   |             |   |                                   | <b>5d. PROJECT NUMBER</b><br>98PR05665-00                        |  |
|  |             |   |                                   | <b>5e. TASK NUMBER</b>   |  |
|  |             |   |                                   | <b>5f. WORK UNIT NUMBER</b><br>ONR 334                           |  |
| <b>7. PERFORMING ORGANIZATION NAME(S) AND ADDRESS(ES)</b><br>University of Arkansas<br>120 Ozark Hall<br>Fayetteville, AR 72701  |             |   |                                   | <b>8. PERFORMING ORGANIZATION REPORT NUMBER</b>                  |  |
| <b>9. SPONSORING/MONITORING AGENCY NAME(S) AND ADDRESS(ES)</b><br>Office of Naval Research<br>Program Officer: Dr. George Campisi<br>Ballston Centre Tower One<br>800 North Quincy Street<br>Arlington, VA 22217-5660  |             |   |                                   | <b>10. SPONSOR/MONITOR'S ACRONYM(S)</b><br>ONR                   |  |
|  |             |   |                                   | <b>11. SPONSORING/MONITORING AGENCY REPORT NUMBER</b>            |  |
| <b>12. DISTRIBUTION AVAILABILITY STATEMENT</b><br>Approved for Public Release; distribution is UNLIMITED   |             |   |                                   |  |  |
| <b>13. SUPPLEMENTARY NOTES</b>   |             |   |                                   |  |  |
| <b>14. ABSTRACT</b><br>The part 1 of the final report develops a new sizing procedure to calculate the SRM peak and continuous power ratings and introduces new coefficients that consider multi-phase operation. It then proposes a new Feed-Forward ANN-based system to map the SRM terminal variables and the SRM mutual interaction and torque. It also proposes a ANN-based on-line torque estimator which does not require a torque transducer and adapts to the characteristic of the individual SRM. Finally, this report concludes by considering an implementation of the ANN on the Texas Instrument express DSP TMS320C6701. |             |   |                                   |  |  |
| <b>15. SUBJECT TERMS</b><br>Switched Reluctance Motor Design, Electric Propulsion  |             |   |                                   |  |  |
| <b>16. SECURITY CLASSIFICATION OF:</b>   |             |   | <b>17. LIMITATION OF ABSTRACT</b> | <b>18. NUMBER OF PAGES</b>                                       | <b>19a. NAME OF RESPONSIBLE PERSON</b>           |
| a. REPORT  | b. ABSTRACT | c. THIS PAGE  |                                   |  | <b>19b. TELEPHONE NUMBER (include area code)</b> |
| U  | U           | U   | U                                 | 155  | J. C. Balda<br>501-575-6578                      |

## TABLE OF CONTENTS

|                               |    |
|-------------------------------|----|
| <b>TABLE OF CONTENTS.....</b> | ii |
|-------------------------------|----|

### **Chapter One – INTRODUCTION**

|  |   |
|--|---|
| 1.1 General Overview.....  | 1 |
| 1.2 Basic Operating Principle of the SRM and Associated Terminology..... | 1 |
| 1.3 EV Propulsion Application.....                                       | 6 |
| 1.4 SRM Application Issues and Contributions of this Report.....         | 8 |

### **Chapter Two – SIZING A SWITCHED RELUCTANCE MOTOR FOR ELECTRIC VEHICLES**

|   |    |
|---|----|
| 2.1 Introduction.....                             | 12 |
| 2.2 Procedure for Sizing the SRM.....             | 14 |
| 2.3 Results of the Sizing Calculations.....       | 17 |
| 2.4 SRM Loss Trends.....                          | 20 |
| 2.5 Comparison with Other EV Electric Motors..... | 22 |
| A PMSM Discussion.....                            | 23 |
| B IM Discussion.....                              | 24 |
| C DC Motor Discussion.....                        | 24 |

### **Chapter Three – DESIGN APPROACH UNDER MULTI-PHASE EXCITATION**

|  |    |
|--|----|
| 3.1 Introduction.....                                  | 26 |
| 3.2 Nomenclature.....                                  | 26 |
| 3.3 SRM Magnetic Circuit and Excitation Modes.....     | 27 |
| 3.4 Design Coefficients for Multi-Phase Operation..... | 36 |
| A Number of turns/pole $N$ .....                       | 36 |

|  |  |    |
|--|--|----|
| <i>B</i>   | <i>Peak torque per pole pair <math>T_{peak}</math></i> .....                       | 37 |
| <i>C</i>   | <i>Peak winding current <math>I_{peak}</math></i> .....                            | 38 |
| <i>D</i>   | <i>RMS winding current <math>I_{rms}</math></i> .....                              | 39 |
| 3.5  | <b>SRM Design Steps and Prototype Design</b> .....                                 | 40 |
| 3.6  | <b>Description Of the Experimental Results</b> .....                               | 43 |
| <i>A</i>   | <i>Comparison of Measurements vs. FEA Simulations</i> .....                        | 43 |
| <br><b>Chapter Four – ARTIFICIAL NEURAL NETWORKS FOR</b>         |  |    |
| <b>MODELING THE MULTIPLY EXCITED SRM</b>                         |  |    |
| 4.1  | <b>Introduction</b> .....  | 49 |
| 4.2  | <b>The Multi-Phase Modeling of the SRM</b> .....                                   | 50 |
| <i>A</i>   | <i>Mutual-Flux Linkage and Torque Behavior</i> .....                               | 51 |
| <i>B</i>   | <i>The Mutual Flux Interaction Function <math>M(i_1, i_2, \theta)</math></i> ..... | 55 |
| <i>C</i>   | <i>ANN-based Representation of <math>M</math> and Torque</i> .....                 | 56 |
| 4.3  | <b>ANN Training using Measurements of <math>M</math> and Torque</b> .....          | 57 |
| 4.4  | <b>Simulations And Results</b> .....   | 63 |
| <br><b>Chapter Five – ADAPTIVE ON-LINE TORQUE ESTIMATION</b>     |  |    |
| 5.1  | <b>Introduction</b> .....  | 68 |
| 5.2  | <b>Novel Torque Estimation Technique</b> .....                                     | 70 |
| 5.3  | <b>The Inversion Algorithm</b> .....   | 72 |
| 5.4  | <b>Simulation and Implementation Results</b> .....                                 | 75 |
| <br><b>Chapter Six – DSP IMPLEMENTATION OF ANN BASED CONTROL</b> |  |    |
| <b>SOLUTIONS</b>   |  |    |
| 6.1  | <b>Introduction</b> .....  | 79 |

|  |               |
|--|---------------|
| <b>6.2 Description of the ANN Implementation.....</b>                              | <b>79</b>     |
| <b>6.3 Testing of the ANN using Probe Points.....</b>                              | <b>83</b>     |
| <b>6.4 Interfacing the C6701 EVM to the C240 EVM.....</b>                          | <b>84</b>     |
| <b>6.5 Preliminary Implementation of Adaptive Estimation ANN and DSP/BIOS.....</b> | <b>88</b>     |
| <b>Chapter Seven – CONCLUSIONS AND SUGGESTED<br/>FUTURE WORK.....</b>              | <b>90</b>     |
| <br><b>Appendix A – DERIVATIONS OF SIZING EQUATIONS.....</b>                       | <br><b>93</b> |
| <b>Appendix B – C++ PROGRAM FOR SIZING THE SRM.....</b>                            | <b>101</b>    |
| <b>MATLAB CODE FOR SIZING OTHER MOTORS.....</b>                                    | <b>106</b>    |
| <b>Appendix C – ANSYS CODE.....</b>  | <b>110</b>    |
| <b>Appendix D – SIMULINK MODELS.....</b>   | <b>145</b>    |

## ABSTRACT

The Final Report of ONR Grant N00014-98-1-0617 – “Design of a Switched Reluctance Motor Drive for Electric Propulsion” – has been divided into two parts. Part 1 is entitled “Aspects of Switched Reluctance Motor Drive Application for Electric Vehicle Propulsion”. Part 2 is entitled “Operation, System Design and Control of Switched Reluctance Motor with Multiphase Excitation”.

Electric motor drives applied to propulsion of Electric Vehicle (EV) have to typically traverse a wide range of speeds and power levels during their operation. It is then essential to determine and verify the adequacy of the motor design during each assumed operating condition. Also, it is necessary to determine and state the required SRM continuous power rating for the intended EV propulsion application before starting the design. Towards this end, the Part 1 of the Final Report has developed a new sizing procedure to determine the SRM peak and continuous power rating. New equations were developed to estimate the SRM losses at any operating condition based on assumed losses at one condition.

Recent literature has identified that multi-phase operation of SRM can lead to advantages in terms of torque density, efficiency, torque ripple and acoustic noise. The Part 1 of the Final Report introduces new coefficients that were derived with the help of ANSYS<sup>TM</sup> based FEA studies and take the operation of each multi-phase configuration into account. These coefficients are useful when designing SRM under multi-phase operation. The design ideas are then verified by designing, building and testing the prototype of a 1-hp four-phase 8/6 SRM for EV propulsion.

Torque feedback improves the performance of the SRM drive and aids in aspects such as torque ripple minimization. Also, position sensorless SRM drives are currently being widely investigated due to their increased reliability. Under multi-phase operation, it is essential to account for the mutual flux interactions between phases in order to get high accuracy in these tasks. The Part 1 of the Final Report proposes a new Feed-Forward Artificial Neural Network (ANN) based system to provide mapping between the SRM terminal variables and the SRM mutual interaction function and torque.

Building upon the previous modeling research work, the Part 1 of this Final Report proposes a simple ANN based on-line torque estimator that eliminates the need for a torque transducer, adapts to the characteristics of the individual SRM and can be easily extended to the multi-phase case.

Finally, the Part 1 of the Final Report concludes by considering an implementation of the ANN on the Texas Instruments expressDSP<sup>TM</sup> TMS320C6701. The pipelining features of the TMS320C6701 and the Code Composer Studio features are used to obtain low execution times for the ANN. The implementation verifies the feasibility of the proposed ANN-based methods.

# Chapter One

## INTRODUCTION

### 1.1 General Overview

The main advantages of the Switched Reluctance Motor (SRM) in terms of a simple construction (hence higher reliability), high torque densities and high fault tolerance have been recognized for a long time. In addition, the required power electronics converters may have simple unipolar configurations that are simpler to design and operate [1]. SRM drives have been gaining popularity ever since the advances in power electronics technologies have made it feasible to utilize their advantages. These drives are now considered as having great potential for application as variable speed drives.

Section 1.2 presents the basic operating principle of a SRM and introduces the related terminology. One of the potential applications for SRM being widely investigated is for the propulsion of Electric Vehicles (EV). Towards this end, Section 1.3 will include a discussion on Electric Vehicle (EV) propulsion applications. Finally, Section 1.4 will identify some of the current applications, design and operation issues that need better understanding, and highlight the research efforts in these areas.

### 1.2 Basic Operating Principle of the SRM and Associated Terminology

The SRM like any other electric motor has a *stator* (the stationary part) and a *rotor* (the rotating part) that are illustrated in Figure 1.1. Both the stator and the rotor have a *salient* structure. The windings are present only in the stator and their basic unit is a *coil*. Each coil has two *sides*. There can be several winding arrangements determined by the pitch of the coil sides forming a coil. The most commonly used arrangement is the *short-pitch* winding in which both coil sides are present over the same pole (that is, a coil is wound around a pole).

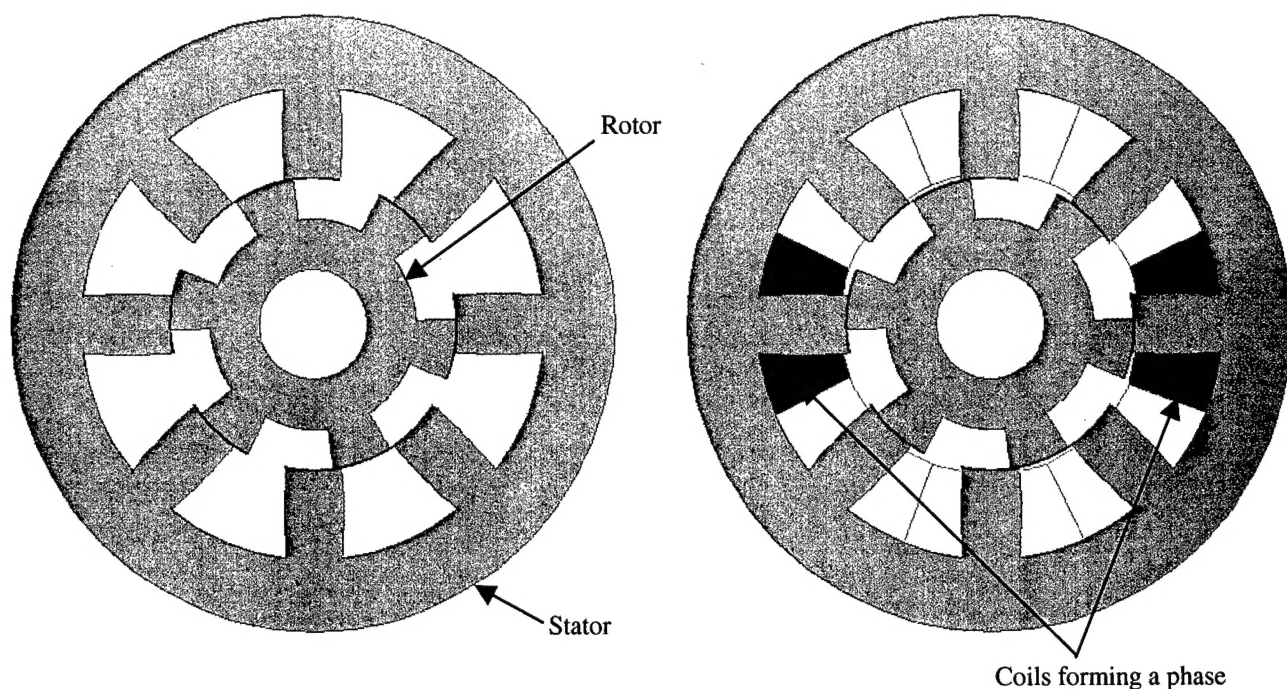


Figure 1.1 SRM cross-section and phase winding.

In this arrangement, coils on physically opposing poles are connected together to form a *phase* such that their magneto-motive force (mmf) aid in setting up the flux throughout these two poles. The other winding arrangements that have been reported are the *full* and *fractional pitches* [2- 3]. Due to the structure of the SRM cross-section, the rotor movement causes a change in the reluctance of the magnetic circuit, and hence, a change in the inductance seen by the stator phase. To understand this change better, we now consider two extreme positions of the rotor with respect to a stator phase. Figure 1.2 shows the first position, which is the *unaligned* position in which two rotor poles have equal angular displacement with respect to the center of a stator phase; in particular, the one indicated in Figure 1.1. In the ideal case of a perfectly balanced construction, exactly equal and opposite tangential force will act on the two rotor poles when this stator phase is excited. As a result, the net shaft torque is zero. A small perturbation in any of the two possible directions results in increased torque in that direction and one of the two rotor poles will move towards the stator pole of the excited phase until it is aligned with it as shown in Figure 1.3.

A Finite-Element Analysis (FEA) derived plot of the flux distribution shows that it is symmetric about the center of the excited stator phase (see Figure 1.2). Figure 1.3 shows the other extreme position, which is the *aligned* position in which a rotor pole is aligned with a stator pole. When the stator phase is excited in this position, the tangential force acting on the rotor poles is zero. So, the shaft torque is again zero.

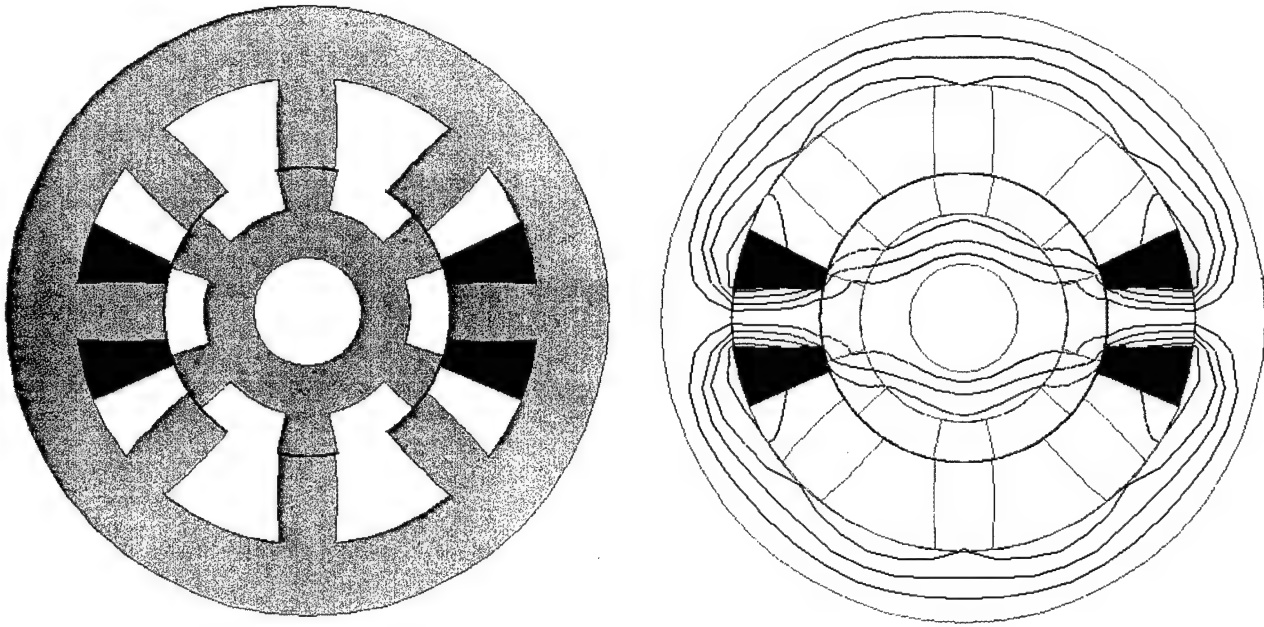


Figure 1.2 SRM unaligned position.

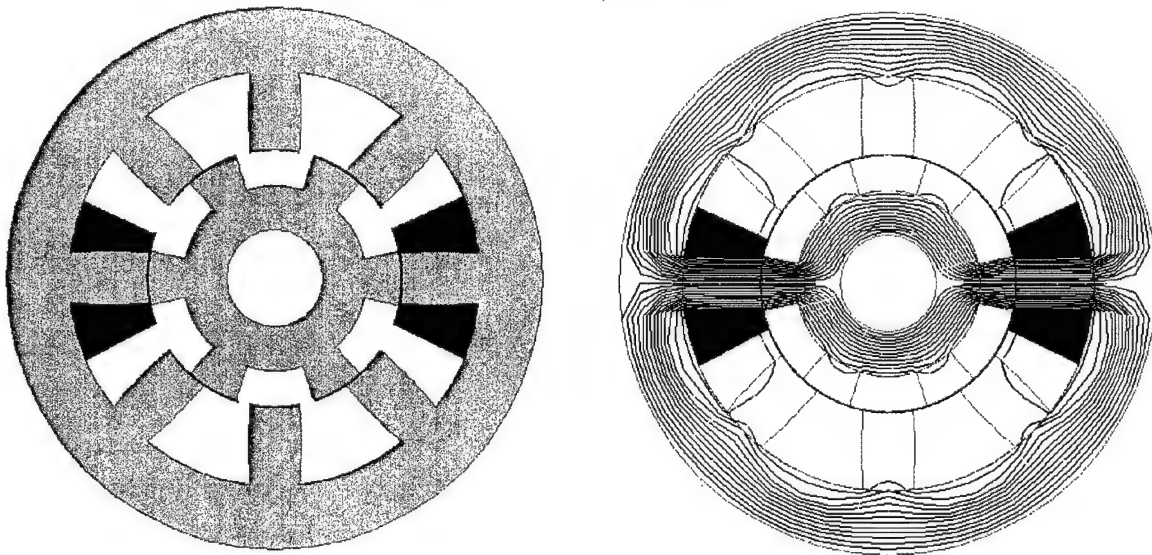
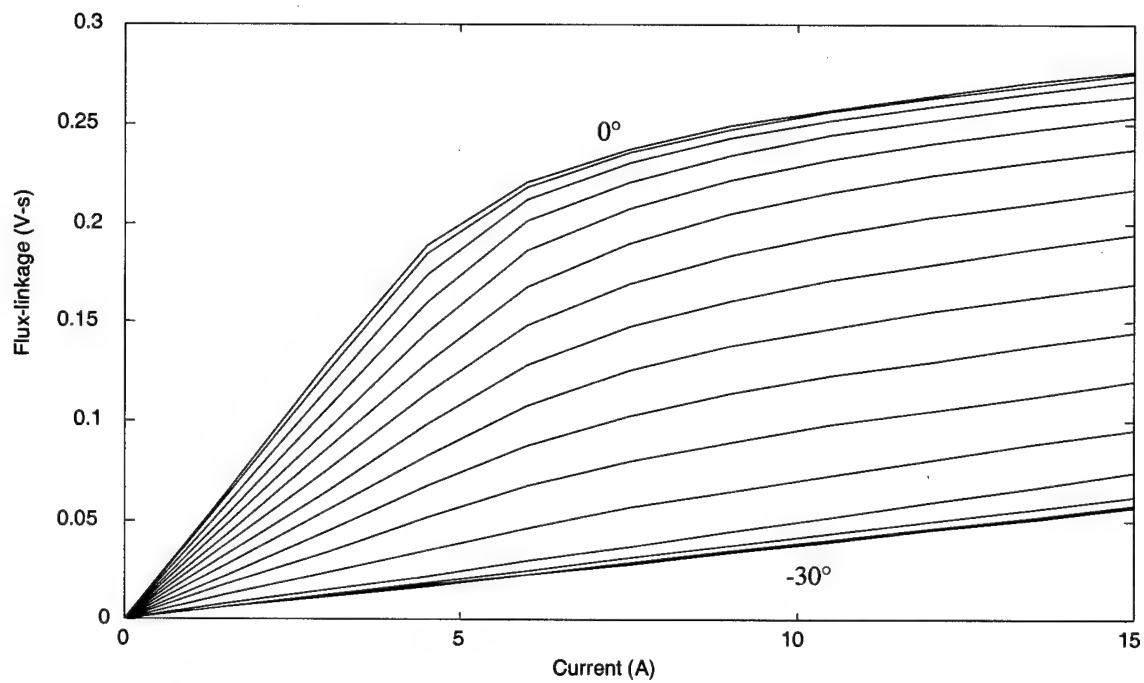


Figure 1.3 SRM aligned position.

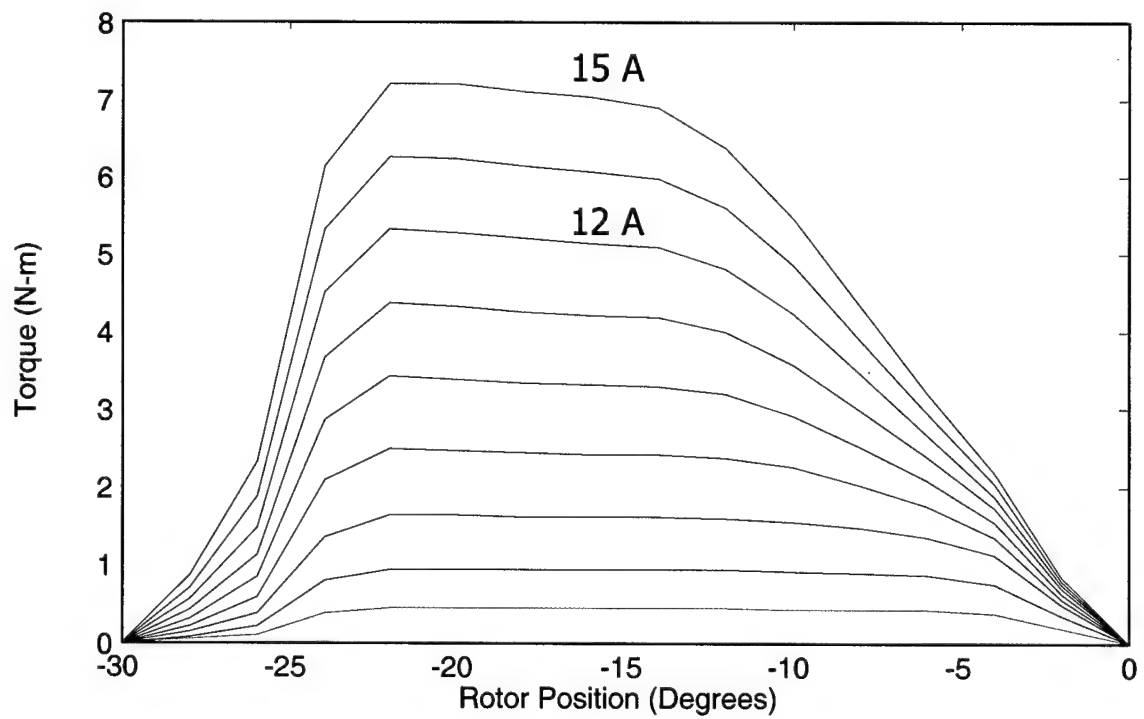
A FEA plot of the flux distribution in this case shows that it is again symmetric about the center of the excited stator phase and the number of flux lines are much higher in value than those at the unaligned position. Hence, the *flux linkage* (the product of the flux and the number of circuit turns linked by it) is much higher in the latter case. These two positions are equilibrium points for the rotor with respect to an excited stator phase. The SRM thus uses the simple principle that forces in any magnetic circuit forces act to align the system in the position of minimum reluctance. The corresponding forces are due to the change in reluctance of the magnetic circuit and the associated torque acting on the poles is known as *reluctance torque*.

The flux linkage of a phase at a constant phase current increases from the minimum value at the unaligned position to the maximum value at the aligned position. At a given rotor position, the flux-linkage increases with increasing phase current. Figure 1.4(a) shows the plot of the flux-linkage characteristics as function of the rotor position for a phase of the four-phase, 8/6 (8 stator and 6 rotor poles) SRM, considered in the previous illustrations. In these cases, the unaligned position is at  $-30^\circ$  and the aligned position is at  $0^\circ$  with respect to the excited phase. The plot shows that the rate of increase of the flux linkage with increasing phase current decreases as the rotor approaches the aligned position ( $0^\circ$ ). This is due to the saturation of the magnetic material used to build the SRM. This saturation is essential for maximizing the efficiency of the energy-conversion process in SRM [1]. However, it leads to a non-linear system that is difficult to control.

Let  $N_s$  denote the number of stator poles and  $N_r$  the number of rotor poles; then, the angular displacement of the rotor pole center with respect to the stator pole center at the unaligned position is  $\theta_u = \frac{180}{N_r}^\circ$ . The angular displacement at the aligned position is always  $\theta = 0^\circ$ . The flux-linkage characteristics such as the one in Figure 1.4(a) form the basis for all the simulation models and computations that are done for the SRM.



(a)



(b)

Figure 1.4 (a) Flux-linkage and (b) torque characteristics of a four phase 8/6 SRM.

An important characteristic that can be derived from the flux-linkage data is the torque characteristic that gives the variation of the developed electromagnetic torque with rotor angular position at different phase current levels. This torque characteristic is derived using the result that the torque in a rotary electromagnetic energy conversion system is given by:

$$T_e = \frac{\partial W_c}{\partial \theta},$$

where  $W_c$  is the co-energy of the electromagnetic system and is given by the area under the flux linkage characteristic at a considered rotor position till the considered phase current. By using this calculation for the flux-linkage characteristics of the SRM in Figure 1.4(a), we get the torque characteristics shown in Figure 1.4(b) for the case when only one phase of the SRM is carrying current. The torque characteristics show the trend that was described before; i.e., the developed torque is zero at the aligned ( $0^\circ$ ) and unaligned ( $-30^\circ$ ) positions for any value of the phase current. Thus, the torque at the shaft of the SRM would have a large difference between the maximum and minimum values when a single phase is only excited; this difference is known as *torque ripple*. This would lead to shaft oscillations at low speeds and increased acoustic noise [4]. In order to minimize this torque ripple and also fully utilize the SRM power output capability, overlap in the phase conduction periods of a SRM (and hence the phase current waveforms) is essential when it is applied in a practical motor drive application.

### 1.3 EV Propulsion Application

An electric motor drive for EV propulsion has to satisfy several operating conditions determined by the performance requirements listed as part of a specification for the EV. In this application, the motor drive has an almost continuously varying duty in terms of the load torque and speed requirements. The EV America Technical Specifications [5], the ANSI-IEEE Standard for Rotating Electrical Machinery for Rail and Road Vehicles [6], and the NEMA Standard for Motors and Generators [7] address the rating of electric motors used in EVs.

These standards require that the peak and continuous power ratings be identified separately for a complete specification of a motor used for electric propulsion of an EV. For a particular electric propulsion application, the EV main specifications are vehicle maximum mass ( $m_{ev}$ ), maximum and rated speeds ( $v_{ev,max}$  and  $v_{ev,r}$ ), acceleration and deceleration times ( $t_a$  and  $t_d$ ), maximum slope or gradient ( $\alpha$ ), rolling coefficient ( $k_r$ ), EV frontal area ( $A_f$ ), dragging coefficient ( $k_d$ ), headwind speed ( $v_{hw}$ ), wheel radius ( $r_w$ ) and gear box ratio(s). In addition, the considered performance specifications must also include the driving schedules (city and highway) and other particular operating conditions. The specifications determine the *road-load* characteristics (see  $F_{ev}$  Figure 1.5) that the EV has to overcome, calculated using the following equation [8] ( $a_d$  - density of air):

$$F_{ev}(v_{ev}) = k_r m_{ev} g + 0.5 a_d k_d A_f (v_{ev} + v_{hw})^2 + m_{ev} g \sin(\alpha) \quad (1.1)$$

Figure 1.5 also shows the *envelope*  $F_{em}$  of the EV motor drive characteristic that depends on the motor drive *peak power rating*, *rated speed* and *maximum speed*.

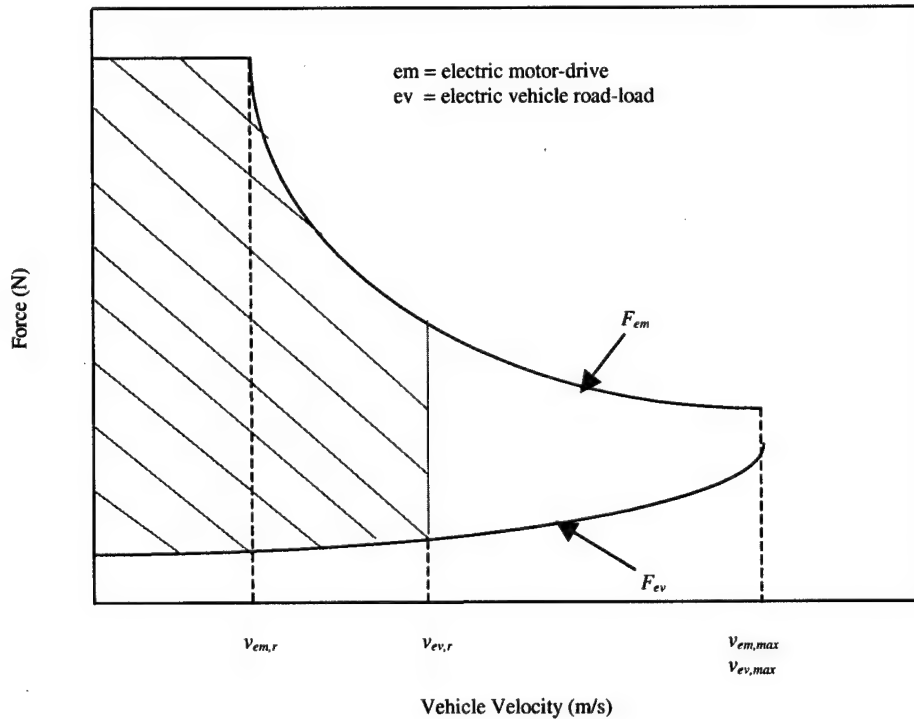


Figure 1.5 The road-load and motor-drive forces as function of vehicle velocity.

The motor drive has to traverse its entire operating characteristic (that is, constant-torque and constant-power regions). The envelope determines the performance obtained from the EV. The shaded area in Figure 1.5 represents the integral that determines the acceleration performance to rated speed that can be obtained from the EV. The road-load characteristic for a given EV is not constant, but changes with the considered condition. When designing the motor drive characteristics for EV propulsion, one has to meet the considered performance specifications, while achieving a high *average drive efficiency* and *low drive weight and cost* [9]. The vehicle speed is related to the electric motor speed through the gear ratio and wheel radius. In the case of EV, there is usually a single gear ratio, and the desired characteristic at the drive shaft is obtained through electronic control (i.e., electronic gearing). Hence, we can carry out all the studies in terms of the vehicle speed, thereby eliminating the need to consider the values of the gear ratio and wheel radius.

#### **1.4 SRM Application Issues and Contributions of this Report**

For EV applications, it is essential to identify and state both the peak and continuous power ratings of the SRM [6]. Towards this end, there is a need at the design stage to formulate a methodology to calculate the continuous power rating of the SRM by predicting the efficiency contours of the SRM based on the assumed efficiency at one operating point. Thus, it is useful to have scaling equations relating losses at one (known) operating point of the motor to those (unknown) losses at any other operating point. It is required to assume the losses at one operating point because the SRM is yet to be designed and built at this stage. This would allow the designer to estimate the motor losses under each operating condition in order to check the adequacy of the motor thermal design for each operating condition. An estimation of the thermal duty would also allow proper choice of the safety margins used in the design which would then determine the life of the SRM drive depending on the temperature attained by the winding under different operating conditions [6-7].

Chapter Two first presents a detailed SRM sizing procedure [12] for the propulsion of EV along with the development of the equations that allow relating losses at one operating point to another one. Using this approach, a code was developed in C++ for sizing the SRM.

In recent literature, the potential for multi-phase operation (more than one phase conducting current simultaneously) has been identified to obtain higher torque densities and higher efficiencies [2-3, 10-11]. These literatures only provide the means for understanding the operation under these conditions. There is however a need for a methodology to design the SRM under multi-phase operating conditions, while taking into account the loading constraints of the magnetic material used to build the SRM and the desired output torque. Chapter Three includes an approach for incorporating the multi-phase operation into the SRM design equations [13]. The theory for this approach was developed jointly by Mr. Edilberto Hall Mitre and myself. I suggested the idea of introducing coefficients to account for the multi-phase operation into the already existing design equations [1] for SRM under single-phase operation. Mr. Hall Mitre and I determined the values of these coefficients based on the results of the FEA studies. I performed all the FEA studies. Mr. Hall Mitre then developed the MATLAB™ code for designing the SRM using this approach. Using this sizing and design approach as an aid, a 1 hp four-phase 8/6 SRM prototype was designed by me and built by Baldor Motors and Drives (Fort Fort Smith, AR). Mr. Roberto Marcelo Schupbach and I then carried out static measurements on the SRM to quantify the performance. A description of this design and the obtained performance are included in Chapter Three.

Since the SRM is designed to be non-linear and has a coupled magnetic circuit, it is expected that superposition principles cannot be applied to predict its behavior under multi-phase operation. However, it is essential to identify and predict the non-linear torque characteristics of the SRM under multi-phase operating conditions for tasks such as torque feedback or torque ripple minimization.

In addition, it is essential to identify and adapt to the characteristics of each individual SRM due to variations in their characteristics due to manufacturing tolerances and variance in the magnetic material characteristics. For these tasks, it is necessary to develop feasible solutions that provide adequate accuracy. To this end, Chapter Four proposes Feed-Forward (FF) Artificial Neural Network (ANN) based solutions to achieve this non-linear mapping between the SRM terminal variables and its performance [14]. The idea of using ANN for this task was initially proposed by me. Mr. Schupbach and I then tried out several cases of using ANN for the torque-mapping task. The simulation studies by incorporating ANN into the SRM model were done by Mr. Schupbach. A new FF ANN based torque estimator is proposed in Chapter Five that can learn and adapt to the characteristics of the individual SRM based on on-line measurements [15].

Finally, Chapter Six considers an implementation of the considered FF ANN based solutions on the TI TMS320C6701 DSP and reports on the performance obtained. A scheme is also suggested for communicating the torque feedback from the TMS320C6701 to the TMS320F240 EVM (the SRM PWM generator) [16].

Throughout this report, references are given at the end of each chapter.

## References

- [1] T.J.E. Miller, Switched Reluctance Motor and Their Control, Magna Physics Publishing and Clarendon Press - Oxford, 1993.
- [2] B.C. Mecrow, "New Winding Configurations for Doubly Salient Reluctance Machines", *IEEE Transactions on Industry Applications*, Vol. 32, No. 6, November-December 1996, pp. 1348-1356.
- [3] Y. Tang, "Switched Reluctance Motor with Fractionally Pitched Windings and Bipolar Currents", *Conference Proceedings of the 1998 Annual Meeting of the IEEE Industry Applications Society*, pp. 351-358.
- [4] R. Krishnan, P. Vijayraghavan, "State of the art: Acoustic noise in switched reluctance motor drives", *Proceedings of the Annual Conference of the IEEE Industrial Electronics Society*, pp. 929- 934, August 1998.
- [5] "1997 EV America Technical Specifications", Department of Energy EV web-site - <http://www.ott.doe.gov/oaat/evs.html>
- [6] "IEEE Standards Collection – Electric Machinery", 1993 Edition.
- [7] "NEMA Standard for Motors and Generators", NEMA MG 1-1993.

- [8] M. Ehsani, K. M. Rahman, H. A. Toliyat, "Propulsion System Design of Electric and Hybrid Vehicles", *IEEE Transactions on Industrial Electronics*, Vol. 44, No. 1, pp. 19-27, February 1997.
- [9] E. M. Hall, S. S. Ramamuthy, J. C. Balda, "Optimum Speed Ratio of Induction Motor Drives for Electric Vehicle Propulsion", *Proceedings of the IEEE Applied Power Electronics Conference*, pp. 371- 377, March 4- 8 2001, Anaheim, California.
- [10] Michaelides and C.Pollock, " Short Flux Paths Optimize the Efficiency of a 5-Phase Switched Reluctance Drive", *Conference Proceedings of the 1995 Annual Meeting of the IEEE Industry Applications Society*, pp.286-293, Orlando (FL), October 8- 12.
- [11] J. Moon, S. Oh, J. Ahn and Y. Hwang, " Switched Reluctance Motor with 2-Phase Excitation", *Conference Proceedings of the 1998 Annual Meeting of the IEEE Industry Applications Society*, pp. 547-552, St. Louis (MO), October 12- 15.
- [12] Shyam S. Ramamurthy, J. C. Balda, T. Ericson, "Sizing a switched reluctance motor for electric vehicles", *Conference Proceedings of the IEEE Industrial Applications Society Annual Meeting*, pp. 71- 78, October 7-12 2000, Rome, Italy.
- [13] E. M. Hall, S. S. Ramamuthy, J. C. Balda, "An Enhanced Simple Method for the Design of Switched Reluctance Motors under Multi-phase Excitation", *Proceedings of the IEEE International Electric Machines and Drives Conference at MIT*, June 2001.
- [14] S. S. Ramamurthy, R. M. Schupbach, J. C. Balda, "Artificial Neural Network based Models for the Multiply Excited Switched Reluctance Motor", *Conference Proceedings of the IEEE Applied Power Electronics Conference*, pp. 1109- 1115, March 4- 8 2001, Anaheim, California.
- [15] S. S. Ramamuthy, J. C. Balda, T.Ericson, "Intelligent and Adaptive On-line Direct Electromagnetic Torque Estimator for Switched Reluctance Motors based on Artificial Neural Networks", *Conference Proceedings of the IEEE International Electric Machines and Drives Conference at MIT*, June 2001.
- [16] Shyam S. Ramamurthy, Juan Carlos Balda, "Implementation of Neural Networks to aid Switched Reluctance Motor Control on the TMS320C6701", *TI DSPS Fest 2000*, Houston, August 2000.

## Chapter Two

### SIZING A SWITCHED RELUCTANCE MOTOR FOR ELECTRIC VEHICLES

#### 2.1 Introduction

The EV America Technical Specifications [1], the ANSI-IEEE Standard for Rotating Electrical Machinery for Rail and Road Vehicles [2], and the NEMA Standard for Motors and Generators [3] address the rating of electric motors used in EVs. Hence, these are used when appropriate throughout this chapter.

These standards require that the peak and continuous power ratings be identified separately for a complete specification of a SRM used for electric propulsion of an EV. A detailed procedure is presented in this chapter to determine these power ratings given the vehicle specifications. To determine the continuous power rating of the SRM, it is necessary to know the variations of the SRM losses with vehicle speed and power requirement. To this end, the report work has led to the development of new equations that are used in the sizing calculations to estimate the variations of the SRM losses with speed and power output. The equation derivations are included in Appendix A.

For a particular electric propulsion application, the EV main specifications are vehicle maximum mass ( $m_{ev}$ ), maximum and rated speeds ( $v_{ev,max}$  and  $v_{ev,r}$ ), acceleration and deceleration times ( $t_a$  and  $t_d$ ), maximum slope or gradient ( $\alpha$ ), rolling coefficient ( $k_r$ ), EV frontal area ( $A_f$ ), dragging coefficient ( $k_d$ ), headwind speed ( $v_{hw}$ ), wheel radius ( $r_w$ ) and gear box ratio(s). The EV specifications considered in this study, listed in Table 2.1, are the minimum specifications for an EV qualifying as an EV America “production-level” vehicle [1].

**Table 2.1 The EV Specifications.**

|  |                     |   |  |
|--|---------------------|---|--|
| Vehicle mass                           | 1000 kg (GM Impact) | Mass considered in calculations ( $m_w$ ) | 1172 kg (vehicle with 2 166-lb occupants)                                  |
| Rolling Coefficient ( $k_r$ )          | 0.013               | Acceleration duty ( $t_a$ )               | 0 to 50 mph in 13.5 s  |
| Aerodynamic Drag Coefficient ( $k_d$ ) | 0.29                | Maximum speed ( $v_{ev,max}$ )            | 70 mph (drive should be able to operate continuously under this condition) |
| Frontal Area ( $A_f$ )                 | 2.13 m <sup>2</sup> | Gradient ( $\alpha$ )                     | 0%, 3% at 55 mph, 6% at 45 mph and capable of ascending a 25% gradient     |
| Wind Velocity ( $v_{hw}$ )             | 5 mph               |   |  |

The force vs. speed characteristic (or the so-called "road-load" characteristic) is determined from the EV main specifications (see Figure 1.5). The considered performance specifications also include the driving schedules (city and highway) to be satisfied and other operating conditions. The driving schedule data are given in the form of vehicle velocity at time instants equally spaced (see Figure 2.1). The sizing calculations presented here consider the *Federal Test Procedure* (FTP) and the *Highway Fuel Economy Driving Schedule* (HWFET) representing city and highway driving conditions, respectively [4]. The other considered operating conditions are based on the minimum performance specifications for a commercial EV given in [1].

The vehicle speed is related to the electric motor speed through the gear ratio and the wheel radius. All the results are reported in terms of the vehicle speed, thereby eliminating the need to consider the values of the gear ratio and the wheel radius in this study.

In the analysis, the SRM total losses are equal to the sum of copper and total-iron losses (i.e.,

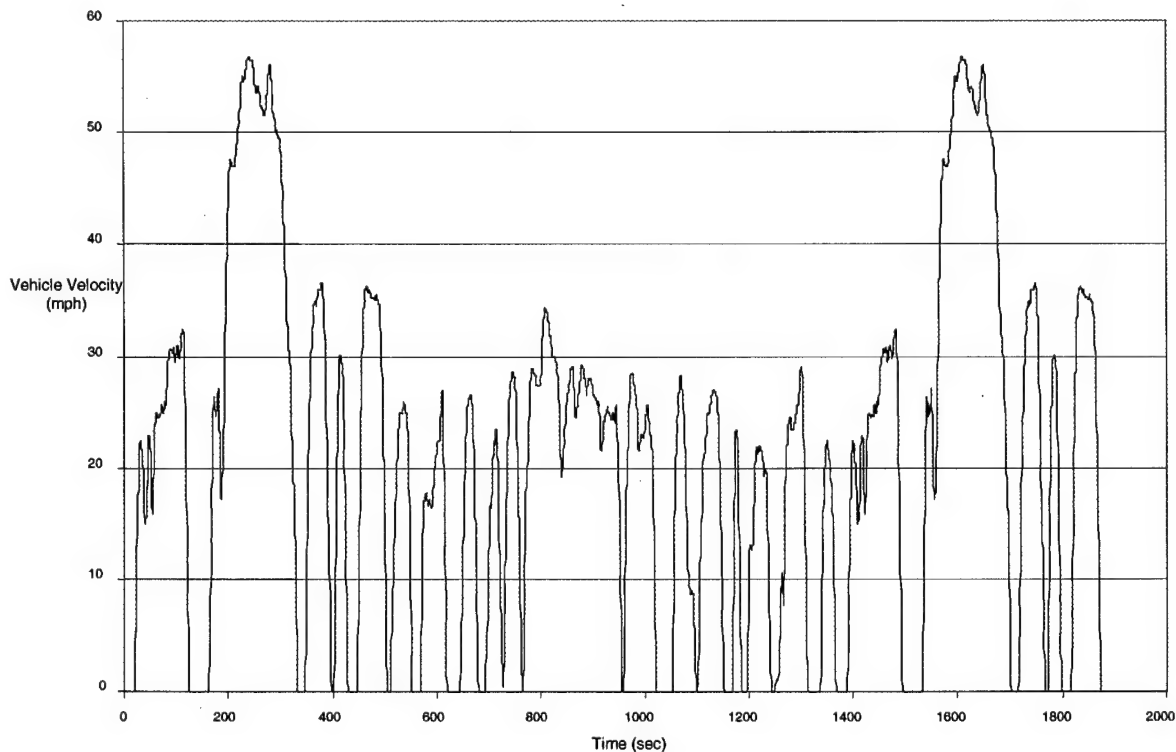


Figure 2.1 The FTP is composed of the UDDS (Urban Dynamometer Driving Schedule) followed by the first 505 seconds of the UDDS.

$W_{SRM} = W_{cu} + W_{Fe}$ ). Rotational losses are not considered although they could be included as suggested in [2]. In the following sections, we explain the proposed procedure for determining (sizing) the ratings of a SRM for EV propulsion. This explanation is followed by the results of applying this procedure to sizing a SRM for the EV specified in Table 2.1. The Chapter also includes a discussion on the continuous power ratings and the thermal duty of other electric motors as compared to the SRM for the same EV propulsion application.

## 2.2 Procedure for Sizing the SRM

For a complete specification of the electric motor, (i) the peak and continuous power ratings should be identified separately, and (ii) the peak power (or short-time capability) should be corrected according to the requirements imposed by all considered driving schedules and operating conditions [1-3]. In [5], the peak power rating is also called the rated or continuous power of the electric motor; this might lead to overdimensioning the electric motor. We can determine the peak power rating  $P_{emp}$  and the continuous power rating  $P_{emcont}$  by taking into account the vehicle specifications, considering the principles of operation of SRMs, and assuming (or knowing) the motor loss values at only one operating point.

Initially, the peak power rating  $P_{emp}$  of the SRM (i.e., the electric motor) is calculated from the specified acceleration duty as shown in [5]. This value is then compared with (a)  $P_{emmax}$ , the power for cruising at the vehicle maximum velocity [5], as well as the powers  $P_{emg}$  required when the EV is moving at (b) 55 mph on a 3% gradient, (c) 45 mph on a 6% gradient, and (d) ascending a 25% gradient at low speed. The value of  $P_{emp}$  is changed to  $P_{emmax}$  or the highest  $P_{emg}$  if any of these values is greater than the initial value of  $P_{emp}$ . To determine the continuous power rating  $P_{emcont}$  of the SRM, we need to identify that particular operating condition imposing the most severe thermal performance requirement on the SRM (i.e., the condition with the highest losses).

This is done by determining an *equivalent* continuous power rating  $P_{cont,i}$  at a chosen speed (we chose the rated speed  $v_{em,r}$ ) for each operating condition  $i$  (for example, like the driving schedule in Figure 2.1).

Figure 2.2 illustrates that the power losses change as function of the vehicle (motor) velocity. These losses increase the temperature of the electric motor. By definition, the losses dissipated at  $P_{cont,i}$  and the chosen speed are identical to those dissipated throughout the operating condition (where the speed changes). Hence, the temperature rise is the same. This *equivalent* continuous power rating is calculated at the same chosen speed for all conditions to identify that condition resulting in the highest  $P_{cont,i}$ , which then determines the SRM continuous power rating  $P_{emcont}$  valid only at the chosen speed. In other words, the SRM is capable of delivering this  $P_{emcont}$  at the chosen speed. The SRM temperature rise under this continuous power rating should be within the limits specified in [2] for each class of insulation. In other words, the SRM will have the same losses at the continuous power rating  $P_{emcont}$  and the rotor speed corresponding to  $v_{em,r}$  as the average losses corresponding to the most severe operating condition.

Due to the variation of SRM losses with vehicle speed (see Figures 2.2 to 2.4), a certain condition (e.g., cruising at maximum vehicle speed) may produce more losses than when the electric motor is delivering peak power at the chosen speed. To simulate this most-severe condition and test thermally the electric motor, the motor output would have to be increased above  $P_{emp}$  resulting in  $P_{emcont}$  being greater than  $P_{emp}$ , at the chosen speed. However, when  $P_{emcont}$  is specified at another speed at which the SRM efficiency is lower, it should be less than  $P_{emp}$ .

By using the sizing procedure described in this report, the SRM does not need to be capable of delivering  $P_{emp}$  continuously at all the speeds in the operation range of the drive as in [5], but it has to be designed to dissipate the losses occurring during all the specified conditions of EV operation.

In order to calculate  $P_{cont,i}$  it is necessary to know the SRM losses at each power requirement imposed by the operating condition; unfortunately, this is not possible since the SRM (or the electric motor) has yet to be designed. To relate assumed (or known) motor losses at one particular operating point (for example, we select  $P_{emp}$  and rated speed  $v_{em,r}$ ) to the equivalent continuous power rating  $P_{cont,i}$  (also at rated speed  $v_{em,r}$ ), we define the ratio  $s_i$  at the SRM rated speed between  $P_{cont,i}$  and  $P_{emp}$ :

$$s_i = P_{cont,i} / P_{emp} \quad (2.1)$$

For each specified operating condition  $i$  (or driving schedule),  $P_{cont,i}$  is calculated by solving for  $s_i$  in an iterative manner using the following motor-loss equation (refer to the Appendix A for its derivation):

$$s_i \{ (1-c) + c \times f \} + s_i^{0.8} \times c \times (1-f) = (1-c) \times K_1 + c \times f \times K_{2e} + c \times (1-f) \times K_{2h}. \quad (2.2)$$

The Newton's algorithm is used. A first estimate of  $s_i$  is obtained ignoring the exponent 0.8. The coefficient  $c$  represents the ratio between the total-iron loss and total losses of the electric motor, and the coefficient  $f$  represents the ratio between the eddy current and total-iron losses. These coefficients correspond to the peak output power  $P_{emp}$  at any arbitrary speed (we selected the SRM rated speed); that is,  $c = W_{Fep} / W_{SRMp}$  and  $f = W_{ep} / W_{Fep}$ . We used typical values for these two coefficients based on SRM designs presented in the literature [6-8]. The accuracy of the calculated or estimated  $P_{cont}$  depends on the "closeness" between the assumed (or known) loss values and those of the designed and built SRM. In (2.2), the copper-loss coefficient  $K_1$ , the eddy-current-loss coefficient  $K_{2e}$  and the hysteresis-loss coefficient  $K_{2h}$  corresponding to the equivalent continuous power rating  $P_{cont,i}$  are given by (see Appendix A for their derivations):

$$K_1 = \frac{1}{N} \frac{v_{em,r}}{P_{emp}} \sum_{i=1}^N \frac{P_{di}}{v_{ev,i}} \quad (2.3)$$

$$K_{2e} = \frac{1}{N} \frac{1}{P_{emp} v_{em,r}} \sum_{i=1}^N P_{di} v_{ev,i} \quad (2.4)$$

$$K_{2h} = \frac{1}{N} \frac{1}{P_{emp}^{0.8} v_{em,r}^{0.2}} \sum_{i=1}^N C_i \quad (2.5)$$

With

$$C_i = P_{di}^{0.8} v_{ev,i}^{0.2} \quad \text{for } v_{ev,i} \leq v_{em,r}$$

or

$$C_i = P_{di}^{0.8} v_{ev,i}^{0.2} \times \sqrt{\frac{v_{em,r}}{v_{ev,i}}} \quad \text{for } v_{ev,i} > v_{em,r}$$

$N$  represents the number of time instants in the considered driving schedule (or operating condition). For example, the FTP driving schedule has 1874 points.

The power  $P_a$  in the above equations is the power required from the SRM (electric motor) at the center of each time interval in a driving schedule assuming a linear velocity profile between any two consecutive time instants. This power is given by:

$$P_{di} = (F_a + F_{ev}) \times \frac{v_{ev,i-1} + v_{ev,i}}{2} \quad (2.6)$$

The required force components are determined as follows:

- 1)  $F_a$  is the acceleration component to accelerate the vehicle from velocity  $v_{ev,i-1}$  at time instant  $t_{i-1}$  to velocity  $v_{ev,i}$  at time instant  $t_i$ . This force is given by:

$$F_a = k_m m_{ev} \frac{v_{ev,i} - v_{ev,i-1}}{t_i - t_{i-1}}$$

- 2)  $F_{ev}$  is the force required to overcome the road load [5] at the velocity in the center of the considered time interval.

A negative value of  $P_a$  means that the vehicle requires braking power; that is, the electric motor participates in regenerative braking. In this case, the calculated  $P_a$  is inverted in sign for the purpose of only estimating the motor losses. Any additional force required during braking over the capability of the electric motor at a given vehicle speed is assumed to be provided by a mechanical braking system.

The constant  $k_m$  takes into account the rotating masses within the EV. The total force ( $F_a + F_{ev}$ ) during acceleration must be checked if it is less than or equal to the SRM peak capability based on the value of  $P_{emp}$  calculated earlier. If not, the peak SRM power  $P_{emp}$  must be made equal to the value corresponding to this total force. The C++ program for sizing the SRM is included in Appendix B.

### 2.3 Results of the Sizing Calculations

Assuming a ratio of 5:1 between the maximum and rated rotor speeds [5], the sizing procedure produces the following results for the EV specifications in Table 2.1:

#### A. SRM peak (output) power rating

- (1) Accelerating from 0 to 50 mph in 13.5 sec = 28 kW.
- (2) Ascending a 25% gradient (at 20 mph) = 28 kW.
- (3) Maintaining 55 mph in a 3% gradient = 20 kW.
- (4) Maintaining 45 mph in a 6% gradient = 21 kW.

(5) Cruising at the maximum vehicle velocity = 19 kW at the maximum motor speed.

Thus, the peak output power rating  $P_{\text{mp}}$  of the SRM is specified as 28 kW.

#### B. Continuous (output) power rating

The values of  $K_p$ ,  $K_{2e}$ ,  $K_{2h}$  and  $s_i$  were determined using the driving schedules FTP and HWFET as well as the power requirements at the maximum vehicle velocity of 70 mph and for sustained speeds on gradients. Values of  $f = 0.333$  and  $c = 0.4$  (considered typical for a SRM) were assumed [6-8]. The calculated results are listed in Table 2.2.

Using (2.3), (2.4), (2.5) and finally (2.2) with  $N = 1$ ,  $P_d = P_{\text{emmax}}$ ,  $v_{e,i} = v_{\text{emr}}$ ,  $P_{\text{emmax}}$  of 19 kW at the maximum speed corresponds to  $P_{\text{con},i}$  of 18 kW at the SRM rated speed with the  $K_p$ ,  $K_{2e}$ ,  $K_{2h}$  and  $s_i$  values listed in Table 2.2. This duty of cruising at the maximum vehicle speed results in the highest value of  $P_{\text{con},i}$ .

**Table 2.2 The Continuous Power Ratings at Rated Speed for the SRM**

| Condition                            | $K_i(3)$ | $K_{2e}(4)$ | $K_{2h}(5)$ | $s_i(2.2)$ | $P_{\text{con},i}(2.1)$ |
|--------------------------------------|----------|-------------|-------------|------------|-------------------------|
| FTP                                  | 0.121    | 0.381       | 0.252       | 0.172      | 5                       |
| HWFET                                | 0.103    | 1.222       | 0.455       | 0.324      | 9                       |
| Maintaining 55 mph in a 3 % gradient | 0.182    | 2.806       | 0.507       | 0.601      | 17                      |
| Maintaining 45 mph in a 6 % gradient | 0.233    | 2.411       | 0.558       | 0.592      | 17                      |
| Cruising at maximum vehicle speed    | 0.133    | 3.333       | 0.446       | 0.626      | 18                      |

The continuous power rating  $P_{\text{con}}$  of the SRM is specified as 18 kW at the SRM rated speed (see Table 2.2).

Assuming a safety factor of 1.2, the output power ratings of the SRM to be designed and built are:

Peak power = 34 kW at and above the rated speed of the SRM.

Continuous power = 23 kW at the maximum speed of the SRM.

Figure 2.2 shows the ideal (torque or force) envelope of the SRM drive (referred to the EV wheels), the road-load characteristic (as per (1.1) for the EV specifications in Table 2.1) and the SRM loss variation (when the SRM is developing the power required to satisfy the road-load characteristic). Here, Area I is the specified operating region (when the vehicle speed is less than the maximum specified value of 70 mph)

and Area II is the region where the EV is still capable of operating due to the SRM peak power output capability  $P_{emp}$ . However, the SRM drive is not capable of operating continuously in this region due to thermal considerations. It is clear from the figure that this EV is not capable of travelling at velocities greater than about 90 mph.

## 2.4 SRM Loss Trends

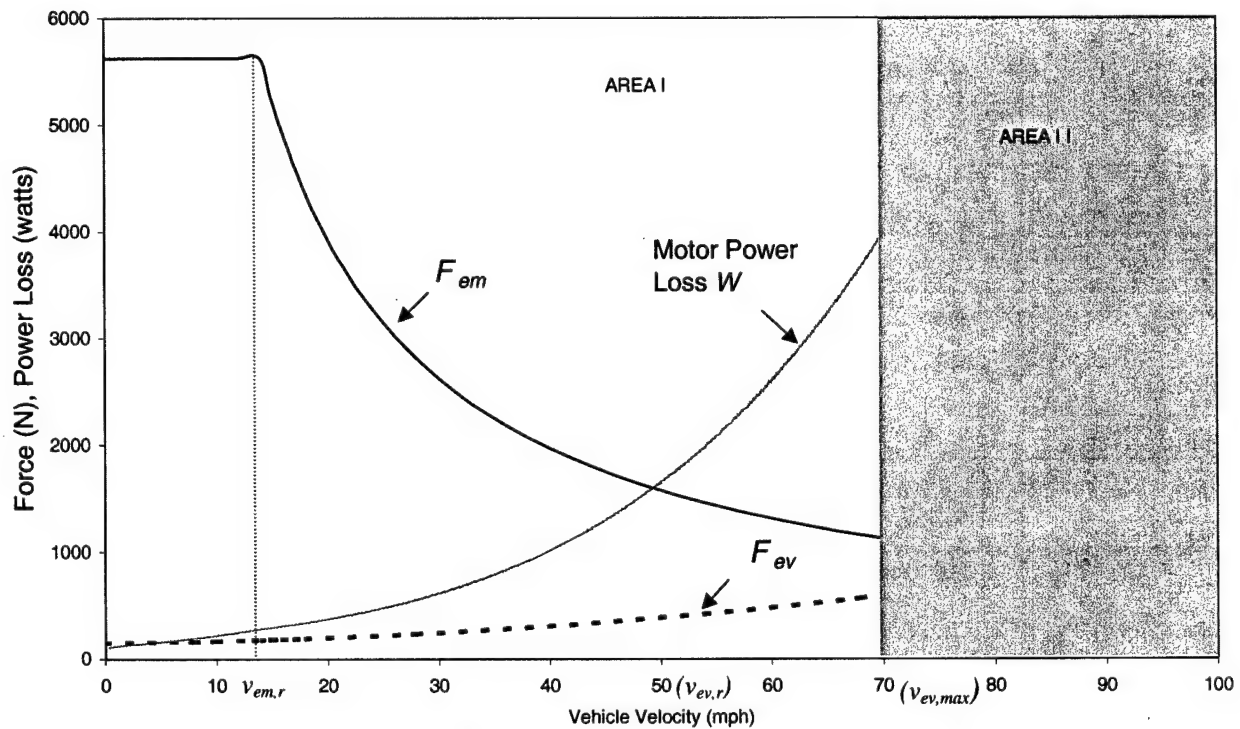


Figure 2.2 The electric propulsion drive envelope, EV road-load characteristics, SRM loss variations and the operating areas.

In order to achieve a low loss dissipation or low thermal duty for the electric motor and also have the optimum efficiency for the EV drive, it is essential to understand the behavior of each motor loss component as a function of the EV speed and power requirement. To this end, Figure 2.3 shows the

variations of the SRM losses with vehicle velocity when the SRM is developing a constant torque equal to that value required at the vehicle maximum velocity. Figure 2.4 shows the variations of SRM losses with vehicle velocity when the SRM is developing the power required to overcome the specified road load. In these figures, each loss component is normalized (in per-unit) with respect to the total loss at the peak power output and rated speed. The total losses are plotted using the assumed values of  $f$  and  $c$ . For a constant torque demand, the SRM losses increase with increasing vehicle velocity (and drive speed). This is mainly due to the increase in the iron losses with vehicle speed; in particular, the eddy-current loss component exhibits the most rapid increase. Finally, it is clear from Figure 2.4 that the losses are the highest when the vehicle is cruising at the maximum vehicle speed.

Next, we analyzed the effects of the contributions of the loss components on the continuous power rating of the SRM. For  $c (= W_{Feq} / W_{SRMq})$  varying between 0.3 to 0.7 with  $f = 0.333$ , the continuous power rating at rated speed varies between 0.5 to 1.03 times the peak power rating  $P_{emp}$ . On the other hand, varying  $f (= W_{ep} / W_{Feq})$  between 0.3 to 0.7 with  $c = 0.4$  results into the continuous power rating at rated speed varying between 0.6 to 1.07 times of  $P_{emp}$ . Since the iron loss shows an increase with the drive speed, it is desirable to keep the iron losses at a lower fraction of the total losses by choosing  $c$  low and to design the SRM with low eddy-current losses by choosing  $f$  low. This reduces the losses at the maximum cruising velocity, and hence, it reduces the loss-dissipation requirements for the SRM. Thus, the continuous power rating and the loss-dissipation duty imposed on the SRM are also functions of the contributions of the individual loss components to the total motor losses; these are determined to a certain degree during the design stage. The development of a design methodology using these ideas is not within the scope of this report.

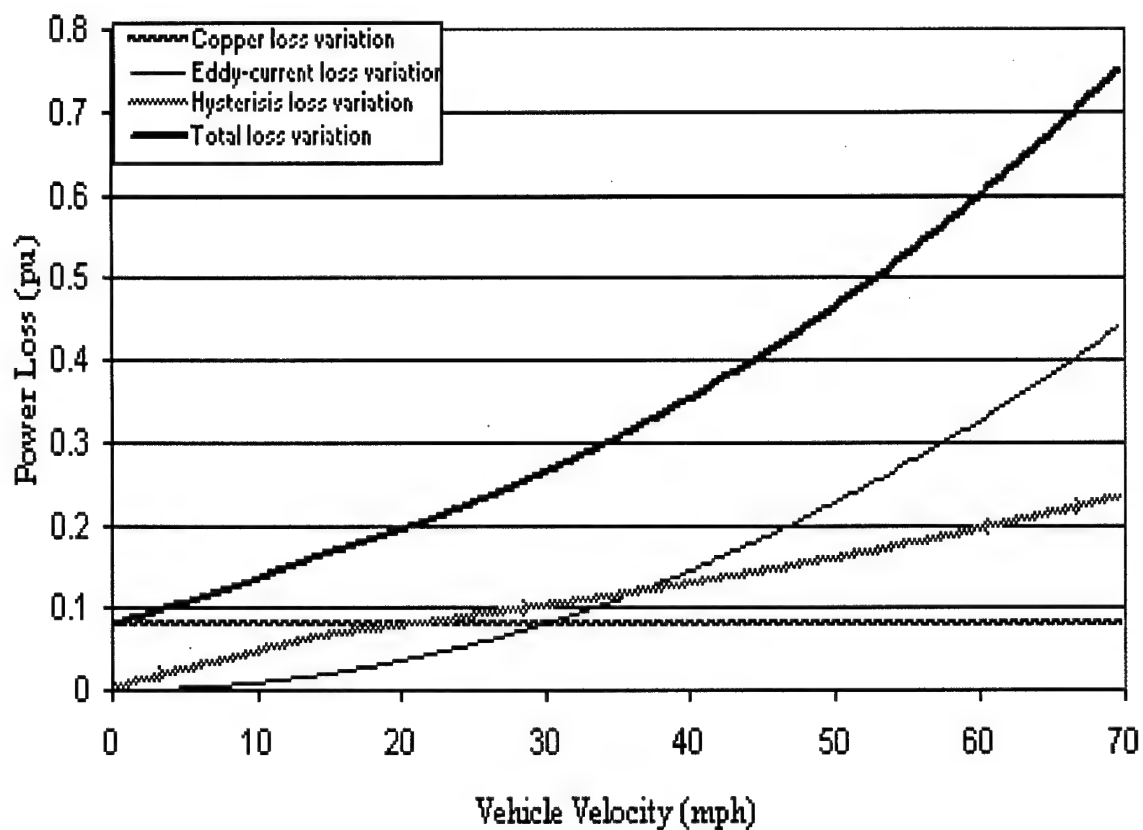


Figure 2.3 Variation of loss components and total loss with vehicle velocity at constant torque.

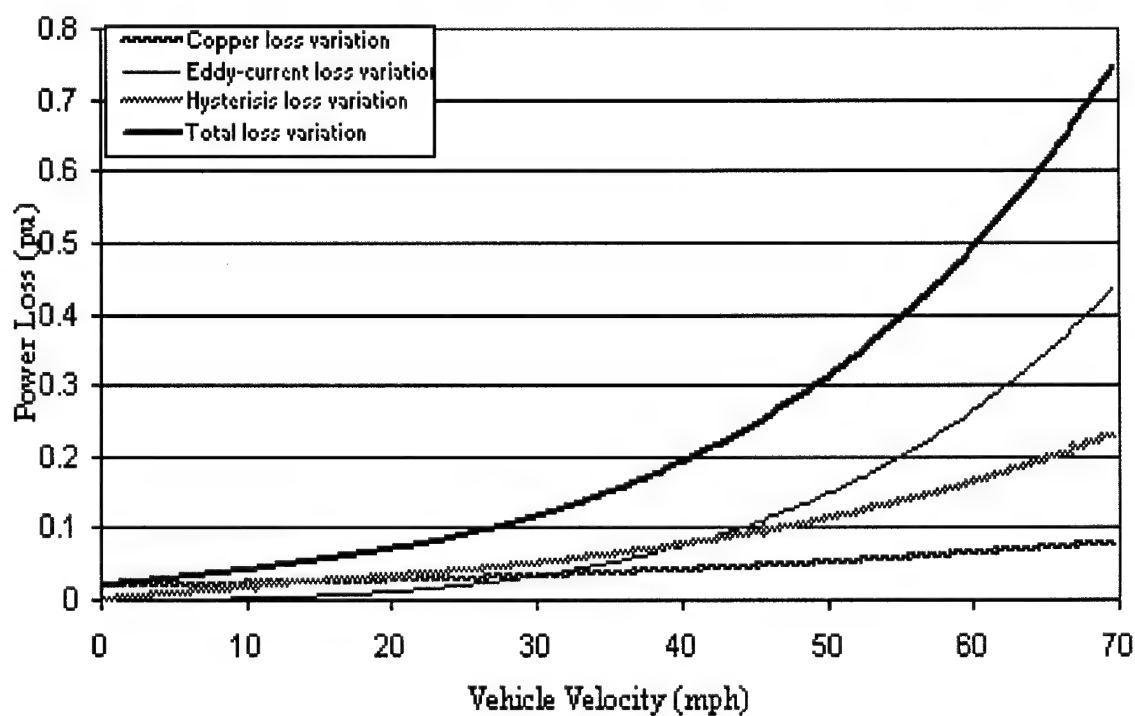


Figure 2.4 Variation of loss components and total loss with vehicle velocity.

## 2.5 Comparison with Other EV Electric Motors

To get a better insight into the thermal duty of the SRM as compared to other electric motors used for this EV application, a similar sizing study for other popular drives was carried out. The considered electric motors are the Permanent Magnet Synchronous Motor (PMSM), the Induction Motor (IM) and the DC Motor. The performance of each motor is described below and the sizing results are presented in Table 2.3. The results are presented for a drive with  $v_{em,max}/v_{em,r} = 2$  and for a drive with  $v_{em,max}/v_{em,r} = 5$  (long constant-power region). See Appendix B for the MATLAB™ code for sizing these motors.

**Table 2.3 Results of Sizing Calculations for Different Motor Types.**

| Ratio<br>$v_{em,max}/v_{em,r}$ | 2<br>$P_{emp} = 59 \text{ kW}$ |      |            | 5<br>$P_{emp} = 34 \text{ kW}$ |      |            |
|--------------------------------|--------------------------------|------|------------|--------------------------------|------|------------|
| Motor Type                     | $W/W_p$                        | s    | $P_{cont}$ | $W/W_p$                        | s    | $P_{cont}$ |
| SRM                            | 0.36                           | 0.34 | 20         | 0.64                           | 0.63 | 22         |
| PMSM                           | 0.84                           | 0.85 | 50         | 1.15                           | 1.12 | 38         |
| IM                             | 0.47                           | 0.35 | 21         | 0.60                           | 0.58 | 20         |
| DC                             | 0.18                           | 0.43 | 26         | 0.56                           | 0.75 | 26         |

$W$  – losses to be dissipated by the motor under the most severe operating condition.

$W_p$  – losses at peak drive power output and rated speed.

The PMSM is considered widely considered as the ideal candidate for EV propulsion due to its high efficiency in the constant torque region [9]. It is clear from our analysis that the PMSM has more losses as compared to other motors when applied for this EV propulsion application, since it has to traverse a large constant-power region during operation. The losses increase due to the high currents required for flux weakening in the constant power region. The studies summarized in Table 2.3 indicate that the average efficiency of the PMSM (as indicated by the losses  $W$ ) in operation is much lower than the other motors. When the SRM loss contributions are chosen appropriately, it becomes comparable to the conventional motors (IM and DC Motor). The behavior of each motor is discussed in detail below.

### A. PMSM Discussion

The PMSM has a fixed excitation determined by the permanent magnets. During operation, the PMSM needs to satisfy the following equations at a given power output  $P_a$  and speed [10]:

$$P_{di} = i_q \times (E_q + (X_d - X_q) \times i_d) \quad (2.7)$$

$$\left( \frac{V}{X_q} \right)^2 = i_q^2 + \left\{ \frac{X_d}{X_q} \left( i_d + \frac{E_q}{X_d} \right) \right\}^2 \quad (2.8)$$

where  $E_q$  is the back-emf induced due to the fixed excitation of the permanent magnets,  $X_d$  and  $X_q$  denote respectively the direct and quadrature axis reactance values of a phase,  $i_d$  and  $i_q$  denote respectively the direct and quadrature axis components of the phase current, and  $V$  is the terminal voltage. To achieve a long constant-power region, it is necessary to weaken the excitation using the d-axis component  $i_d$  of the armature current. This leads to the armature current increasing above the rated speed with an increase in speed. The winding current at the maximum motor speed rises close to or greater than the current at the peak power output and rated speed irrespective of the motor power output. In turn, the copper losses increase at high speeds at all power output levels. The required q-axis current slightly decreases due to the contribution by the reluctance torque. The core losses increase with speed because flux weakening in proportion to the motor speed is not exactly achieved.

The result is that the copper and core losses at the maximum drive speed are high for very high ratios of maximum to rated speed (long constant-power region). In the PMSM, it is difficult to reduce the loss dissipation duty substantially by the choice of the individual components of the total loss. This is because the iron and copper losses have similar increasing contributions as a function of the vehicle speed. In addition, efforts to reduce the d-axis component of current through control result in increased fluxing in the core leading to an increase in core losses.

We have considered a PMSM with interior permanent magnet rotor having  $E_q = 0.80$  pu,  $X_d = 0.50$  pu and  $X_q = 0.66$  pu, with  $c = 0.4$  and  $f = 0.333$ .

The controller is implemented following the concepts of [10], in order to determine the winding currents as function of the vehicle speed and motor power output. Till rated speed, the controller sets the terminal voltage proportional to the frequency. Above this speed, the terminal speed is held constant. The

continuous power rating is determined by the duty of cruising at the maximum vehicle velocity. For this duty, the winding current is close to the winding current corresponding to peak power output at rated speed for  $v_{em,max}/v_{em,r} = 2$  and is higher than this current at  $v_{em,max}/v_{em,r} = 5$  even though the motor power output is only 19 kW. The iron losses are also higher than those at rated speed (at which the continuous power rating is specified).

### B. *IM Discussion*

The IM is assumed to operate under simple  $V/f$  control. Hence, it operates at substantially constant flux upto rated speed. The flux is then inversely proportional to speed in the constant power region. At a given power level and above the rated speed of the motor, the rms armature current remains almost constant with changes in speed. Also, the core losses reduce after the rated speed of the motor because the flux reduction plays a greater role than the frequency increase. The loss-dissipation duty is reduced if the core loss component is minimized in the design.

We have considered an IM with  $c = 0.4$  and  $f = 0.333$ . The continuous power rating is determined by the duty of maintaining a speed of 45 mph in a 6 % gradient.

Since this speed is greater than the rated speed of the motor at both speed ratios, the core losses are lower than those at rated speed. The winding current is approximately equal to the ratio of the power required at the above duty over the peak power output for both speed ratios. The choice of the individual components has a weak influence on the continuous power rating of the motor.

### C. *DC Motor Discussion*

The armature current in the dc machine is constant with speed at a given power level after the rated speed of the motor. The continuous power rating is again determined by the duty of maintaining a speed of 45 mph on a 6 % gradient. The winding current is approximately equal to the ratio of the power required at this duty to the peak motor power output for both speed ratios.

## References

- [1] "1999 EV America Technical Specifications", Department of Energy EV web-site - <http://ev.inel.gov/fop/eva/99EVATECHSPEC.PDF>
- [2] "IEEE Standards Collection – Electric Machinery", 1993 Edition.
- [3] "NEMA Standard for Motors and Generators", NEMA MG 1-1993.
- [4] "EPA Dynamometer Driving Schedules", Environmental Protection Agency web-site - <http://www.epa.gov/OMSWWW/labmthod.htm>.
- [5] M. Ehsani, K. M. Rahman, H. A. Toliyat, "Propulsion System Design of Electric and Hybrid Vehicles", *IEEE Transactions on Industrial Electronics*, Vol. 44, No. 1, pp. 19–27, February 1997.
- [6] T. J. E. Miller, Switched Reluctance Motors and their Control, Oxford Science Publications, 1993.
- [7] T. J. E. Miller, Y. Hayashi, "A New Approach to Calculating Core Losses in the SRM", *IEEE Transactions on Industry Applications*, Vol. 31, No. 5, pp. 1039-1046, September/October 1995.
- [8] P. N. Materu, R. Krishnan, "Estimation of Switched Reluctance Motor Losses", *IEEE Transactions on Industry Applications*, Vol. 28, No. 3, pp. 668-679, May/June 1992.
- [9] D. J. Patterson, "High efficiency permanent magnet drive systems for electric vehicles", *Proceedings of the 1997 23rd Annual International Conference on Industrial Electronics, Control, and Instrumentation*, pp 391-396, Nov 9-14 1997 New Orleans, LA.
- [10] P. Pillay (editor), Performance and design of permanent magnet ac motor drives, IEEE tutorial course presented at the IEEE Industrial Applications Society Annual Meeting, October 1989 - Chapters 6, 8.

## Chapter Three

### DESIGN APPROACH UNDER MULTI-PHASE EXCITATION

#### 3.1 Introduction

Recent literature has identified the potential for operating the SRM advantageously under multi-phase excitation [1- 4]. The operation of SRM configurations working under multi-phase excitation is described in these literatures in terms of the phase inductances. This description, though useful for understanding the operations of these configurations, cannot be used when designing the SRM, given a specification set to be satisfied. When designing electric machines, one has to take into account the constraints imposed by the electric and magnetic loadings of the machine (i.e., current and flux densities, respectively). To this end, the Chapter describes the work carried out as part of this Report that attempts to obtain a better understanding of these SRM configurations when operated in the multi-phase excitation mode. FEA studies based on ANSYS™ [5] were the means to obtain and understand the flux distribution in each configuration. Based on these studies, the design procedure of [6] was modified by incorporating coefficients that account for each configuration and mode of excitation. The following sections introduce these coefficients and briefly describe the design procedure, which uses these coefficients. A 1-hp prototype of a SRM for EV propulsion was then designed and built based on this procedure. The details of this prototype are included together with a discussion of the obtained measurement results.

#### 3.2 Nomenclature

|                 |   |                       |                                     |
|-----------------|---|-----------------------|-------------------------------------|
| $B_s$           | Saturation flux density                     | $D_R, D_S, D_{shaft}$ | Rotor, stator and shaft diameters   |
| $L_{stk}$       | Stack length                                | $t_R, t_S$            | Rotor and stator-pole widths        |
| $y_r$           | Rotor yoke thickness                        | $k_d$                 | Ratio of rotor to stator diameter   |
| $K_s$           | Slot-fill factor                            | $T_{peak}$            | Peak torque produced by a pole pair |
| $T_{avg, peak}$ | Average peak torque<br>developed by the SRM | $P_{peak}$            | Peak power                          |

|                    |                                  |                                   |  |
|--------------------|----------------------------------|-----------------------------------|--|
| $N$                | Number of turns/pole             | $N_R, N_S$                        | Number of rotor and stator poles         |
| $m$                | Number of phases                 | $P$                               | Number of pole pairs/phase = $N_s / m$   |
| $rpm, \omega_r$    | Rated speed in $rpm$ and rad/sec | $I, J$                            | Current and current density              |
| $V, E$             | Voltage and electromotive force  | $\theta_e, \theta_m, \theta_{ST}$ | Electrical, mechanical and stroke angles |
| $\beta_R, \beta_S$ | Rotor- and stator-pole arcs      | TRV                               | Torque per unit rotor volume             |

Subscripts avg, mech, cont, rms, I, DC, T, ST, min, STK denote average, mechanical, continuous, effective value, current, direct current, torque, stroke, minimum, and stack, respectively.

### 3.3 SRM Magnetic Circuit and Excitation Modes

When exciting a phase of the SRM, the flux flows through the stator poles, the rotor poles, the rotor body and traverses the air gap. This flux closes its path by returning through the depth of the stator and rotor bodies behind the poles known as the *back iron* (see Figure 3.1). When multiple phases are excited, it is the level of saturation of the back iron that primarily determines the extent to which the multi-phase excitation can be supported by the SRM while still getting advantage due to such an operation. Based on the current polarity with which adjacent phases are excited, the pattern of flux flow in the SRM magnetic circuit changes and determines the saturation level of the back-iron. FEA-based flux plots obtained under the two main excitation modes are displayed in Figures 3.2 and 3.3 to illustrate this better. These are the *long-flux-path* mode, in which the two adjacent excited phases produce the same direction of flux into the back iron resulting into the same fluxing pattern as the single-phase excitation case (see Figure 3.2). The flux flowing through the back iron is hence increased. The rotor and stator back-iron width should be increased adequately to carry this additional flux without reaching deep saturation in order to get advantage in terms of torque density when using multi-phase excitation in this mode.

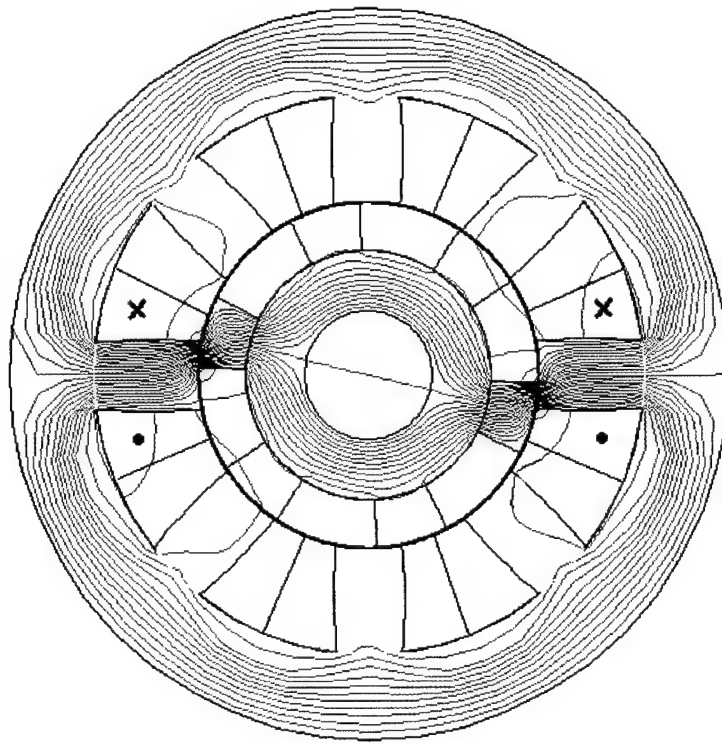


Figure 3.1 Flux distribution for a 8/6 four-phase SRM in the single-phase excitation case for a rotor position of  $\theta = -15^\circ$ .

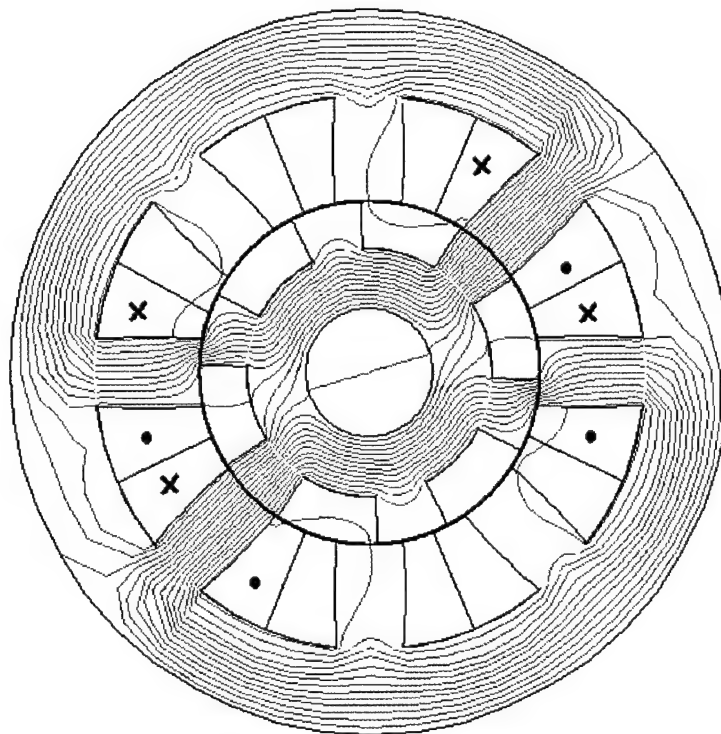


Figure 3.2 Flux distribution for a 8/6 four-phase SRM in the multi-phase excitation case and long-flux-path mode for a rotor position of  $\theta = -15^\circ$ .

By deep saturation, we mean that the back iron is carrying so much flux that any increment in phase current causes a negligible further increment in flux. The other excitation mode is the *short-flux-path* mode in which the two excited phases have opposite direction of flux flow into the back iron. The flux flowing in the back iron is not increased substantially. Thus, this mode requires no increase in the depth of the back iron and at the same time it supports the advantages that can be obtained due to multi-phase operation (see Figure 3.3). These two excitation modes increase the torque density of the SRM by increasing the number of pole-pairs participating simultaneously in torque production. However, the long-flux-path mode requires a corresponding increase in the back-iron depth. When the number of phases is even, the short-flux-path mode requires that the converter have the capability of supplying bipolar currents to maintain short-flux-path mode continuously. When the number of phases is odd, only unipolar currents are required and the short-flux-path mode operation can be obtained through appropriate winding connections. These points will be explained in more detail later in this chapter.

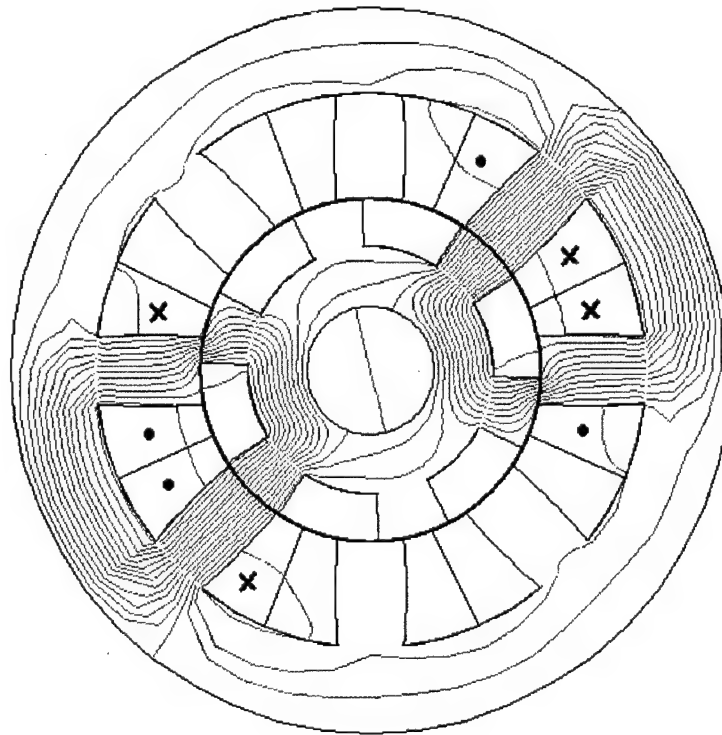


Figure 3.3 The flux pattern in a 8/6 four-phase SRM in the multi-phase excitation case and short-flux-path mode for a rotor position of  $\theta = -15^\circ$ .

There are other excitation modes (like the *full* and *fractional pitch* (FRSRM) winding configurations) that attempt to increase the torque density of the SRM by increasing the number of phases acting simultaneously on a pole pair. As a result, the peak *mmf* to be produced by a phase reduces. However, the time interval for which each phase is carrying a current is increased. So, the rms phase current remains almost the same. This diminishes the advantages that can be obtained by these modes of operation; namely, the *full* and *fractional pitch* (FRSRM) winding configurations. Figures 3.4 and 3.5 (a) and (b) show the *mmf* and flux distribution in a FRSRM carrying square wave currents [3]. In this case, the *mmf* acting on a pair of poles is a function of currents flowing in two phases. In an equivalent short-pitch winding wound over pole 1, a current having a magnitude of  $(i_c - i_b)$  flows and determines the torque produced by the equivalent short-pitch winding.

In case of pole 2, the current flowing is  $(i_a - i_b)$ . For pole 3, the current flowing is  $(i_a - i_c)$ . Figures 3.5 (a) and 3.5(b) shows the magnetic flux distribution in the FRSRM for square-wave currents when  $\theta = 0^\circ$  and  $\theta = 15^\circ$  respectively. At  $\theta = 0^\circ$ , pole 1 produces positive torque and pole 3 produces a torque equal in magnitude to that of pole 1, but negative in sign. Pole 2 does not

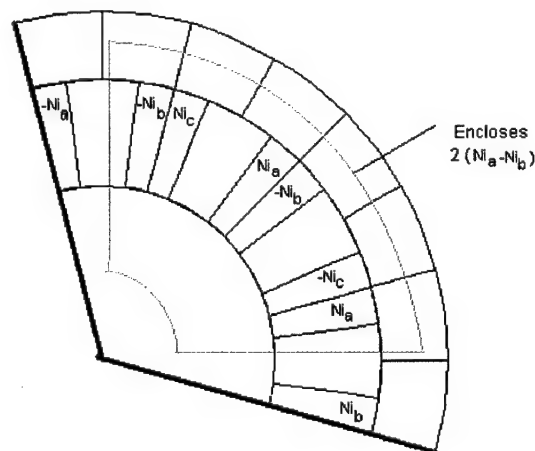


Figure 3.4. The *mmf* distribution in a section of the FRSRM.

produce any torque.

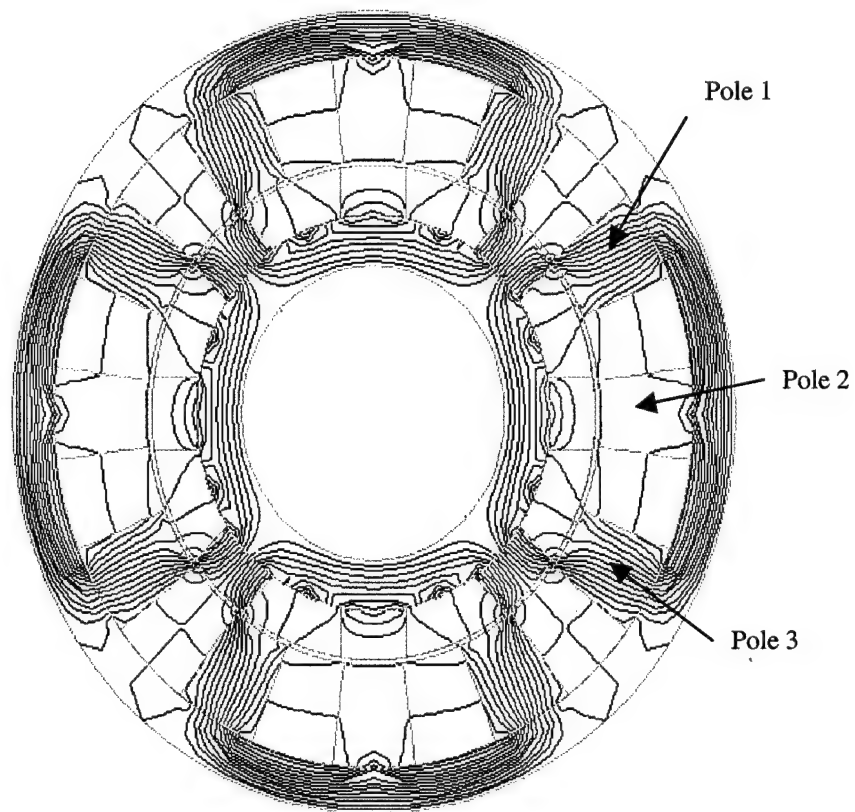


Figure 3.5(a). Flux distribution in the FRSRM for square-wave currents and  $\theta = 0^\circ$ .

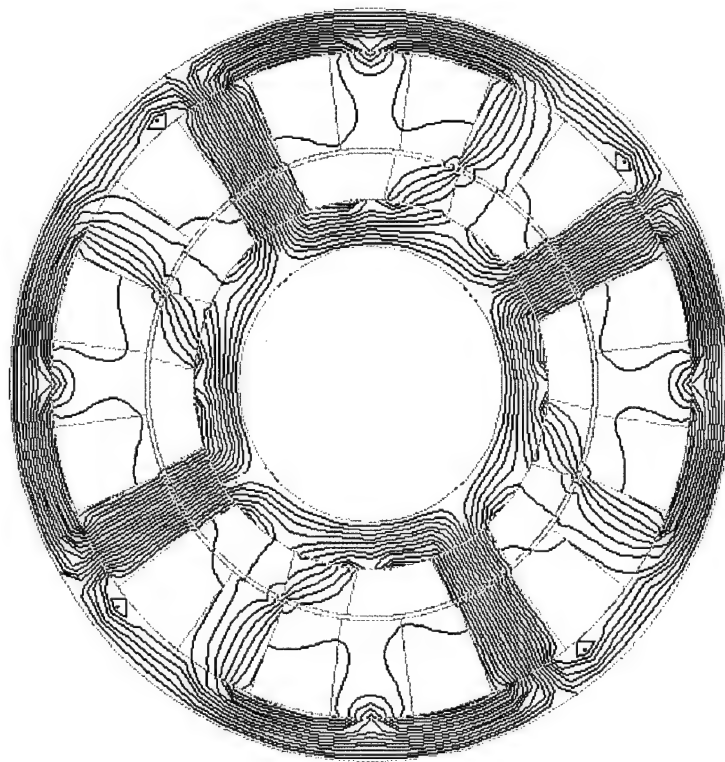


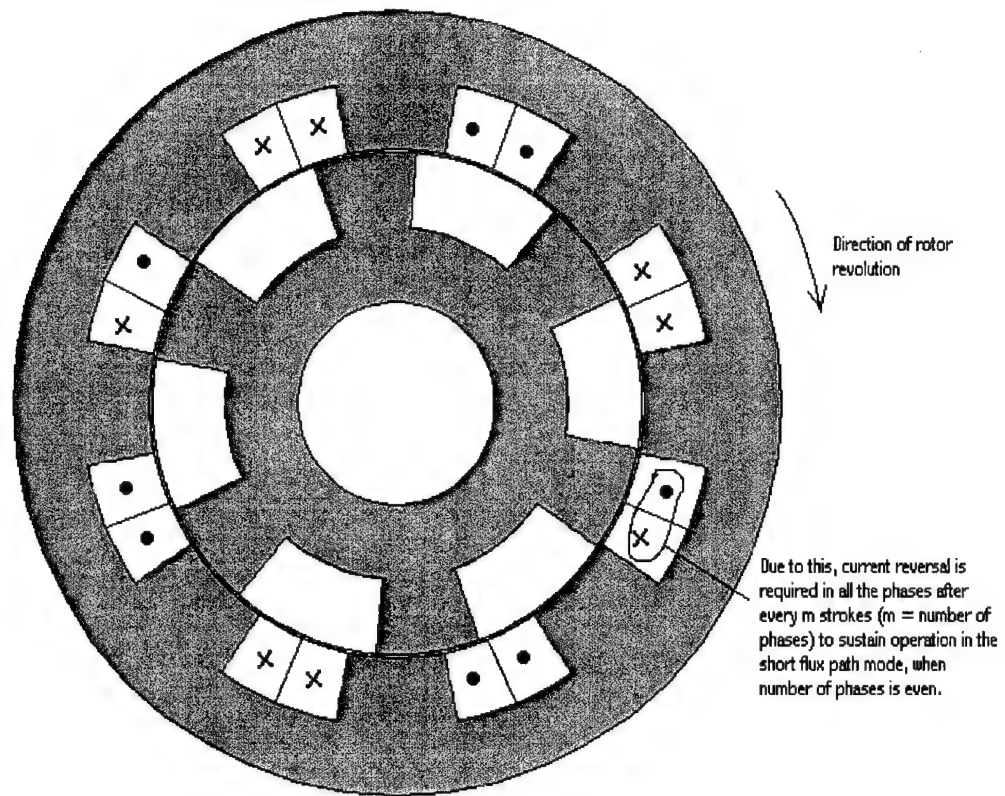
Figure 3.5(b). Flux distribution in the FRSRM for square-wave currents and  $\theta = 15^\circ$ .

At  $\theta = 15^\circ$ , the currents in the equivalent short-pitch windings remain the same. Pole 3 produces positive torque, pole 1 and 2 do not produce any torque. The factor relating the rms phase current to the peak phase current will be greater in this case since all the three phases are carrying current at all times. The work of this report has modified the design equations of [6] to account for the various configurations so that for a particular SRM configuration operated under multi-phase excitation, the design procedure would account for:

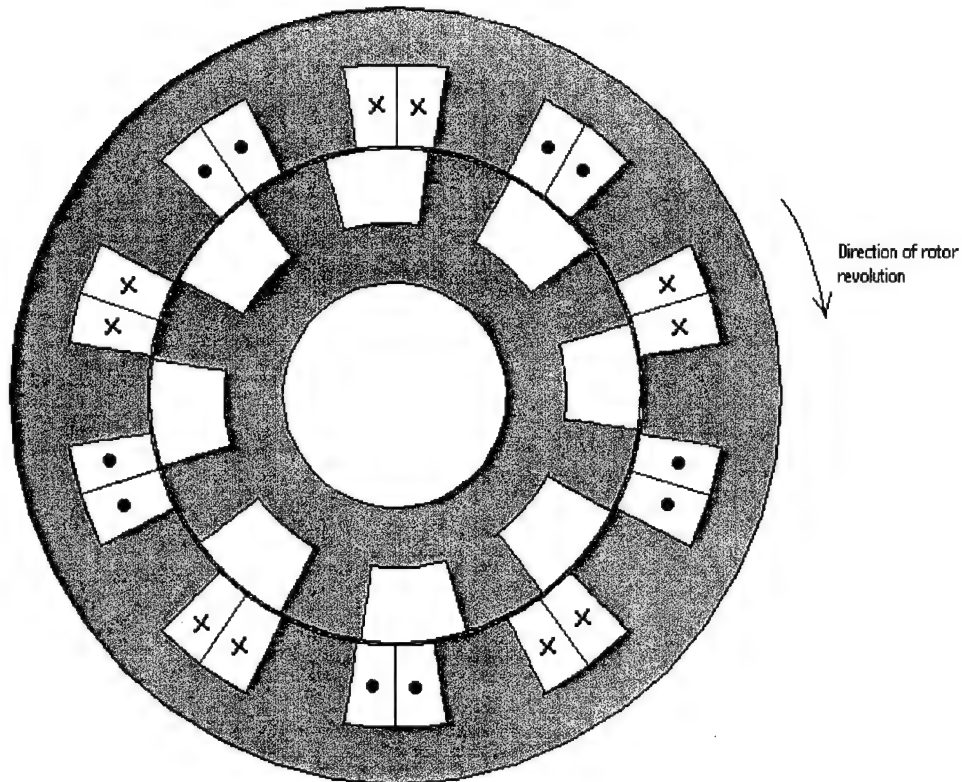
- 1) The increased number of pole-pair participation.
- 2) The increased mmf acting on a pole-pair.
- 3) The torque waveform obtained using a particular configuration.
- 4) The factor relating the average torque to the peak torque.

As mentioned earlier, the short-flux-path mode of operation would give the most benefit in terms of torque density. Thus, the design procedure has been developed to consider only this mode of operation. For instance, the design procedure does not consider the required increment in the depth of the back iron, which is essential in the long-flux-path mode of operation. FEA analyses were carried out for several important SRM configurations to identify the major flux paths in each case. Sample ANSYS<sup>TM</sup> FEA code is included in Appendix C.

Figure 3.6 (a) shows that in the case of the four-phase 8/6 SRM (even number of phases), at the end of 4 strokes, phase current reversal is required to continue operation in the short-flux path mode. However, Figure 3.6(b) illustrates that in the case of the five-phase 10/8 SRM (odd number of phases), the original current direction in the first phase can still sustain operation in the short-flux-path mode at the end of 5 strokes. In this case, appropriate connection of the phases is only required to sustain short-flux-path operation. If operation is not sustained in the short-flux-path mode, the flux would take the long path every  $m$  strokes resulting into a reduction in the instantaneous torque, increased losses, noise and vibrations. Thus, the converter should have the capability of supplying bipolar currents when the number of phases is even with the short-flux-path mode of operation (see Figure 3.6). The flux in any SRM operating under the long-flux-path mode will take the short path mode every  $m$  strokes.



(a)

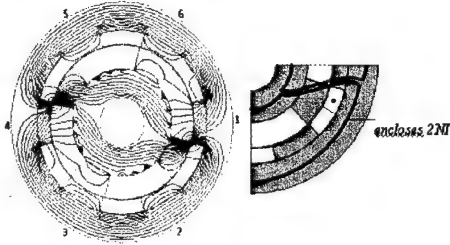
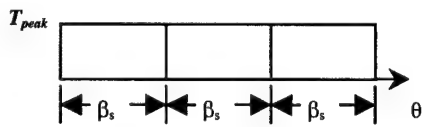
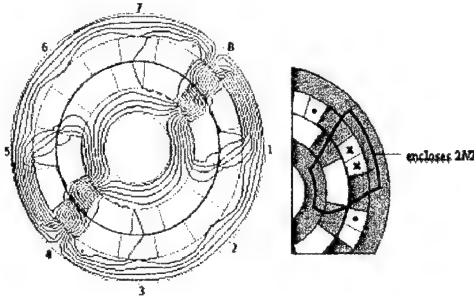
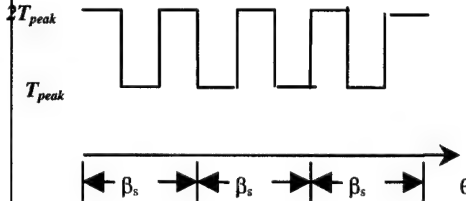
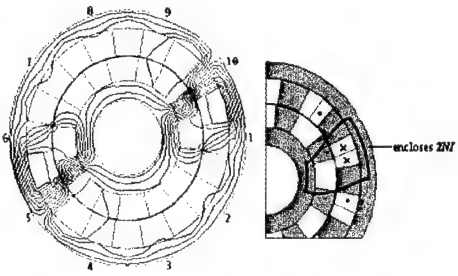
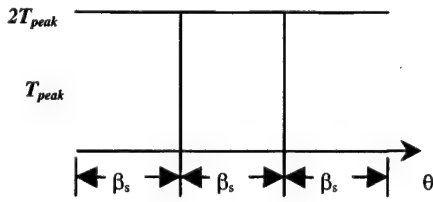


(b)

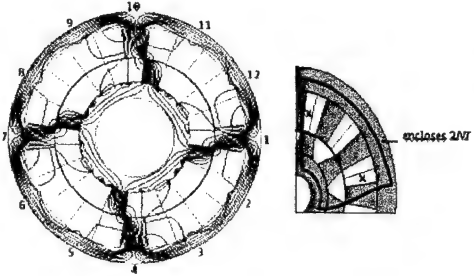
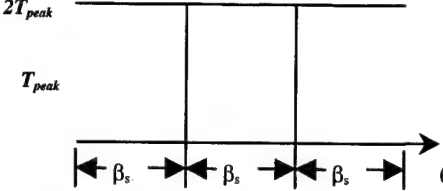
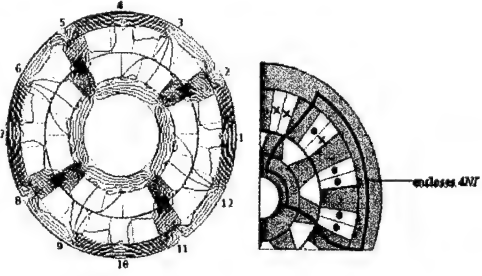
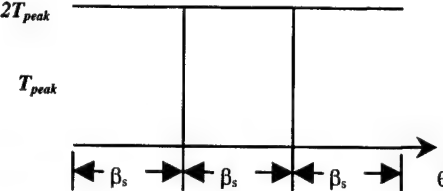
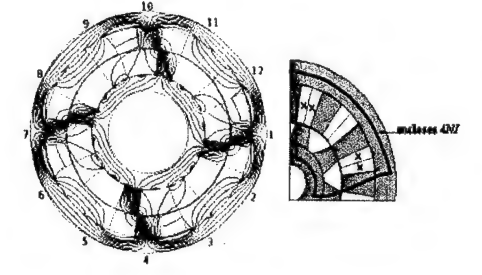
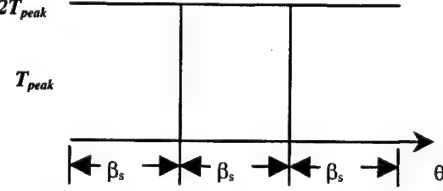
Figure 3.6 Winding connections for the short-flux-path mode over one revolution: (a) Four-phase 8/6 SRM (change in the flux pattern), and (b) Five-phase 10/8 SRM (no change in the flux pattern).

The results are summarized in Tables 3.1. It is clear that some configurations increase the number of pole pairs participating in the torque production while others increase the number of phases acting on a pole pair.

**Table 3.1 FEA of SRM Configurations – Part 1.**

| SRM Configuration and Operation Mode    | FEA Analysis and Major Flux Path  | Ideal Torque Waveform   |
|---|---|---|
| Three-phase 6/4                         |    |    |
| Four-phase 8/6 in short-flux-path mode  |  |  |
| Five-phase 10/8 in short-flux-path mode |  |  |

**Table 3.1 FEA of SRM Configurations – Part 2.**

|                                |   |   |
|--------------------------------|---|---|
| Three-phase 12/8               |    |    |
| Three-phase 12/8<br>FRSRM      |   |   |
| Three-phase 12/8<br>full-pitch |  |  |

### 3.4 Design Coefficients for Multi-phase Operation

This Section introduces the coefficients enabling the design of the SRM under multi-phase excitation. These coefficients are useful for extending established design procedures on SRMs operating under single-phase excitation (such as the one described in [6]). It must be noted that some of the equations listed in [6] are only valid for the specific case of the three-phase 6/4 SRM under single-phase excitation.

It is well known that the SRM operates in a sequence of strokes. Under single-phase excitation, each phase may conduct for a stroke angle given by:  $\theta_{ST} = \frac{360}{mN_R}^\circ$ . (3.1)

In some SRM configurations (e.g., the 8/6 and 10/8 considered in this Report), the stator-pole arc  $\beta_s$  is greater than the stroke angle. As a result, only the fraction  $\theta_{ST}/\beta_s$  of the stator-pole width is actually utilized in torque-production under single-phase operation. To account for this, we introduce the stroke angle coefficient that is given by:

$$K_{ST} = \frac{\beta_s}{\theta_{ST}} \quad (3.2)$$

This can be easily understood by considering the flux-linkage variation in Figure 1.4(a) along the 12 A line. In this case, one can realize that limiting  $\Delta\theta$  to values smaller than  $30^\circ$  will yield smaller flux-linkages and energy conversion. With this background, we present the equations for calculating the number of turns per pole,  $N$ , the peak torque per pole pair,  $T_{peak}$  (which is used for sizing the rotor dimensions [6]), the peak winding current,  $I_{peak}$  and the rms winding current,  $I_{rms}$ . While doing this, we will introduce other design coefficients.

#### A. Number of turns/pole $N$

The magnetic flux per pole is given by

$$\Phi = \frac{B_s t_s L_{STK}}{K_{ST}} \quad (3.3)$$

The coefficient  $K_{ST}$  in the denominator of (3.3) accounts for the fact that only the fraction  $(1/K_{ST})$  of the total stator pole area ( $t_s \times L_{STK}$ ) is actually used in some configurations because the stroke angle is smaller than the stator-pole arc. From (3.3) the flux linkage for two coils in series is given by

$$\lambda = 2 N \Phi . \quad (3.4)$$

The DC voltage  $V_{DC}$  required to produce the magnetic flux in the core is calculated as follows [6]:

$$V_{DC} = (d\lambda / d\theta) \omega = \left( \frac{\lambda}{\theta_{ST}} \right) \omega . \quad (3.5)$$

Substituting (3.3) and (3.4) into (3.5) and solving for the number of turns/pole  $N$  yields:

$$N = K_{ST} \times \frac{\Pi \times V_{DC}}{\omega \times m \times t_s \times L_{STK} \times N_R \times B_s} \quad (3.6)$$

where all linear dimensions are in m,  $V_{DC}$  is in volts,  $B_s$  is in weber/m<sup>2</sup> and  $\omega$  is in rad/sec.

$$N = K_{ST} \times \frac{46500 \times V_{DC}}{rpm \times m \times t_s \times L_{STK} \times N_R \times B_s} . \quad (3.7)$$

When the coils on more than one pole pair are connected in series to form a phase, (3.4) must be divided by  $(P/2)$ . The constant 46500 is a conversion factor that arises when all linear dimensions are expressed in inches and the speed value in rpm as used in [6].

#### B. Peak torque per pole pair $T_{peak}$

The average peak torque is related to the peak power and the rated speed  $\omega$  at which the torque has to be developed as follows:

$$T_{avg, peak} = \frac{P_{peak}}{\omega_r} . \quad (3.8)$$

In the previous Section (see Tables 3.1), we noted that:

- Only one pair of poles develops torque in the three-phase 6/4 SRM at any given time, and
- The average torque developed in the five-phase 10/8 SRM is twice of that developed by that one pole pair.

Thus, the peak torque to be developed by a pole pair in the 10/8 SRM for a given average peak torque is half of that to be developed by one pole pair in the 6/4 SRM.

To account for this in the design equations, we introduce the torque coefficient  $K_T$  that accounts for the reduction in the developed torque by only one pole pair in a particular configuration. As per our definition,  $K_T = 1$  for the 6/4 SRM and  $K_T = 2$  for the 10/8 SRM.

Up to this point, we only considered the unsaturated operation of the SRM. However, the actual SRM operates under saturation. Thus, we introduce the coefficient  $K_{Tpeak}$  accounting for the effects of saturation and given as the ratio of the peak torque to the average value obtained from FEA analysis; that is  $K_{Tpeak} = T_{peak}/T_{avg}$ .

In general, the average peak torque developed by the SRM is given by

$$T_{avg, peak} = \frac{K_T \times \frac{P}{2}}{K_{Tpeak} \times K_{ST}} \times T_{peak} \quad (3.9)$$

From (3.8) and (3.9), the peak torque to be developed by only one pole pair is given by:

$$T_{peak} = \frac{K_{Tpeak} \times K_{ST}}{K_T \times \frac{P}{2}} \times \frac{P_{peak}}{\omega} \quad (3.10)$$

### C. Peak winding current $I_{peak}$

In a three-phase 6/4 SRM with short-pitch windings under single-phase excitation (that is, with only one pole pair producing torque), the peak winding current for developing the torque  $T_{peak}$  is given by [6]:

$$I_{peak} = \frac{T_{peak}}{N \times B_S \times D_R \times L_{STK}} \quad (3.11)$$

In SRM with full- and fractional-pitch windings, the winding arrangement results in increased mmf acting on the flux paths. As a result, the winding current can be reduced for a desired flux density to be developed in the air-gap. To account for this, we introduce the coefficient  $K_I$  which is the amount by which the winding current can be reduced as compared to the short-pitch winding case. By this definition,  $K_I = 1$  in the 6/4 and 8/6 SRM, and  $K_I = 2$  in the 12/8 SRM with full- or fractional-pitch windings. Thus, the peak winding current can be calculated as:

$$I_{peak} = \frac{1}{K_I} \times \frac{T_{peak}}{N \times B_s \times D_R \times L_{STK}} \quad (3.12)$$

This equation applies when the coils on the pole pairs of a phase are connected in series. For the coil parallel connection, (3.12) should be multiplied by  $(P/2)$ .

In summary, we can calculate the turns/pole,  $N$ , the peak torque developed by only one pole pair,  $T_{peak}$  and the peak winding current,  $I_{peak}$  using the new coefficients to modify the equations of the design procedure in [6]. For sizing the winding conductors, we need to calculate the rms value of the winding current  $I_{rms}$  as shown below.

#### D. RMS winding current $I_{rms}$

The coefficient  $K_A$  is defined as the ratio between the rms and peak winding currents. This coefficient takes different values depending on the number of phase currents applied at any one time and the SRM configuration. For continuous single-phase operation, this ratio is given by [6]:

$$K_A = \sqrt{\frac{1}{m}} \quad (3.13)$$

since there is a current in only one phase for the duration of the stroke angle  $\theta_{ST}$ . In the 8/6 and 10/8 SRMs under multi-phase excitation, the current pulse exists for the duration of the stator-pole arc  $\beta_s$ . This increase in conduction (and hence, rms winding current value) can be accounted for by introducing the coefficient  $K_{ST}$  in (3.12). For example,  $\beta_s = 18^\circ$  and  $\theta_{ST} = 9^\circ$  in a 10/8 SRM so the period of the current pulse is increased by a factor of  $18/9 = 2$ . Likewise,  $\beta_s = 22.5^\circ$  and  $\theta_{ST} = 15^\circ$  in the case of the 8/6 SRM with short-pitch windings under multi-phase excitation; the period of the current pulse increases by a factor of  $22.5/15 = 1.5$ .

In general, this coefficient for SRM with short-pitch windings becomes:

$$K_A = \sqrt{\frac{K_{ST}}{m}} \quad (3.14)$$

In the full- and fractional-pitch winding SRM,  $K_A$  is given by the square root of the ratio between the number of phases conducting at a time and the total number of phases. For the three-phase full-pitch winding SRM having two phases conducting at any time,  $K_A = \sqrt{\frac{2}{3}}$ . For the three-phase fractional-pitch winding SRM, all three phases conduct at any given time and  $K_A = \sqrt{\frac{3}{3}} = 1$ .

The multi-phase design coefficients introduced in this section are listed in Table 3.2 for the considered SRM configurations.

### 3.5 SRM Design Steps and Prototype Design

Using the above design coefficients, a simple method for designing SRM under multi-phase excitation was developed in [7]. The method ideas were incorporated into a computer program that calculates the SRM main dimensions, peak current, total weight and winding losses given the input specifications. Figure 3.7 shows the program flowchart which is described in more detail in Dr. E. Hall Mitre's doctoral report [7].

From Chapter 2, the SRM satisfying the assumed performance specifications must have the following ratings:

Peak Power Rating = 34 kW

Continuous Power Rating = 23 kW

The other specifications of the SRM were assumed as:

DC Supply Voltage = 300 V

Rated Speed = 1200 rpm

Maximum Speed = 6000 rpm.

**Table 3.2. Design coefficients.**

| $N_S / N_R$ | Winding Scheme               | $K_T$ | $K_{ST}$ | $K_I$ | $K_A$  |
|-------------|------------------------------|-------|----------|-------|--------|
| 6/4 or 12/8 | Short pitch                  | 1.0   | 1.0      | 1.0   | 0.5778 |
| 6/4 or 12/8 | Full pitch                   | 1.0   | 1.0      | 2.0   | 0.8165 |
| 6/4 or 12/8 | Fractional pitch             | 1.0   | 1.0      | 2.0   | 1.0000 |
| 8/6         | Short pitch, short flux path | 1.5   | 1.5      | 1.0   | 0.6124 |
| 10/8        | Short pitch, short flux path | 2.0   | 2.0      | 1.0   | 0.6324 |

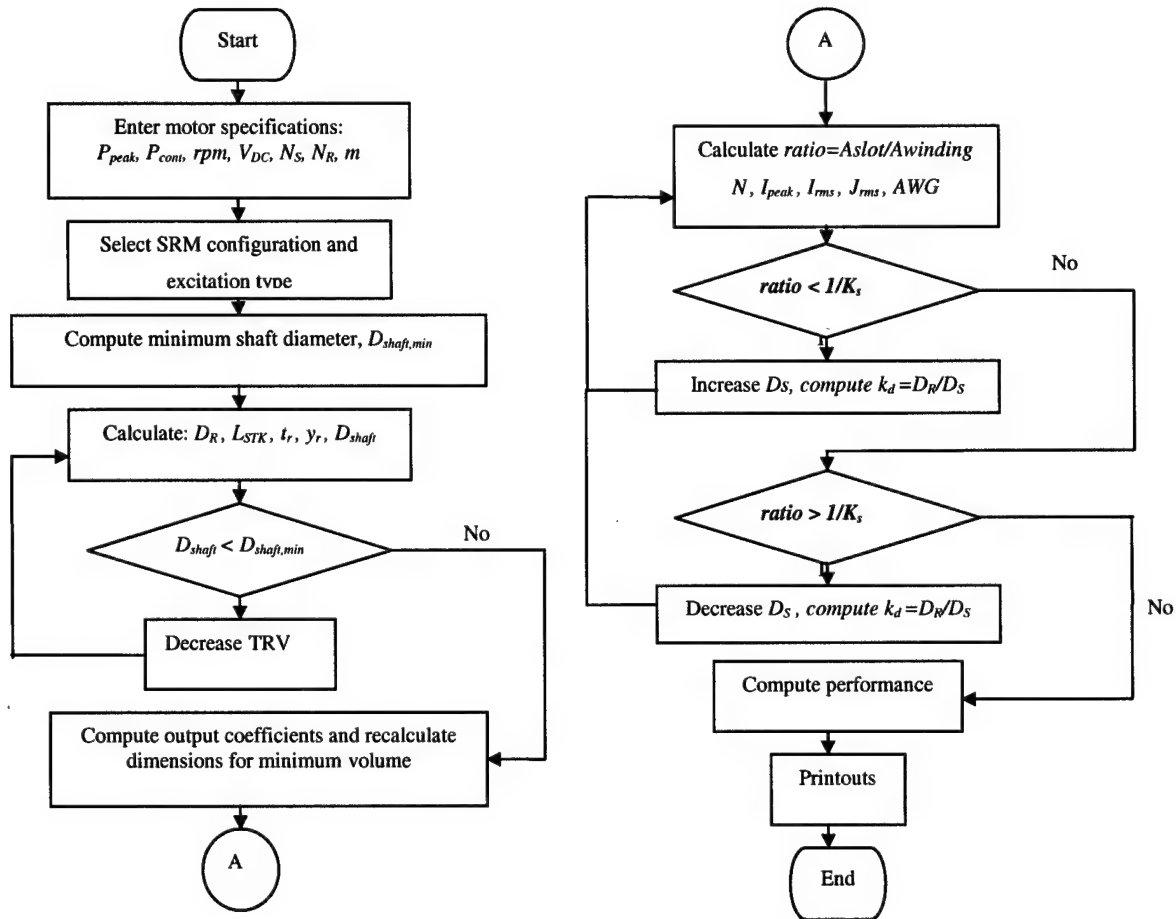


Figure 3.7 Flowchart of the computer program that calculates the SRM main dimensions, peak current, total weight and winding losses.

The maximum speed was chosen as 6000 rpm considering the limitations of the TMS320C240 EVM. The rated speed was chosen as 1200 rpm based on a choice of the speed ratio of 5 for the drive. The different SRM candidates are those ones listed in Table 3.2. For each SRM, Table 3.3 lists the stator outer radius and stack length, weight, peak winding current and copper losses.

These results were obtained using the same constraints on maximum flux and current densities for all configurations. It is clear that the 8/6 SRM and the 10/8 SRM have almost identical weights. However, the 8/6 SRM has a greater angle range available for turn-on angle advancement to build up the phase current even at high speeds. As a result, its torque characteristic is better at high speeds. It is noted that electric motors for EV must operate over a wide speed range. The FRSRM and the full-pitch winding SRM have highly coupled windings, and hence, the phase currents are difficult to set up and control. Due to these reasons, the 8/6 SRM configuration was chosen for this application since it has the feasibility for continuous operation in the short-flux-path mode and adequate angle control for phase advancement. The 8/6 SRM design was then scaled using the following scaling principle proposed in [8]:

$$T_{avg, peak} = \left( \frac{D_R}{2} \right)^3 L_{STK} B_s J N_R \quad (3.15)$$

FEA studies were carried out to refine the design. Some changes to the geometry were made such as the manufacturing requirement of straight poles for easy insertion of coils wound outside the stator on a former. The drawings for this SRM were prepared so that it could be manufactured by Baldor Motor and Drives, Fort Smith, AR. Table 3.4 shows the specifications of the manufactured SRM. The geometry of the stator and rotor laminations is shown in Figure 3.8.

**Table 3.3. Design Results [7]**

| $N_S / N_R$ | Winding Scheme   | Excitation Type               | Stator Outer Radius (m) | Stack Length (m) | Weight (kg) | Peak Current (A) | Copper Losses @ $P_{cont}$ (Watts) |
|-------------|------------------|-------------------------------|-------------------------|------------------|-------------|------------------|------------------------------------|
| 6/4         | Short pitch      | Single phase                  | 0.232                   | 0.298            | 306         | 258              | 665                                |
| 12/8        |                  |                               | 0.188                   | 0.237            | 133         | 264              | 646                                |
| 12/8        | Full pitch       | Multi phase                   | 0.172                   | 0.237            | 111         | 274              | 773                                |
| 12/8        | Fractional pitch | Multi phase                   | 0.179                   | 0.237            | 120         | 274              | 802                                |
| 8/6         | Short pitch      | Multi phase (short flux path) | 0.185                   | 0.237            | 145         | 132              | 563                                |
| 10/8        |                  |                               | 0.186                   | 0.237            | 139         | 132              | 688                                |

**Table 3.4 1-HP Prototype SRM Specifications**

|                                  |   |
|----------------------------------|---|
| Rated Speed                      | 1200 rpm  |
| Maximum Speed                    | 6000 rpm  |
| Continuous Power Rating          | 490 W @ Rated Speed                                   |
| DC Bus Voltage                   | 75 V  |
| Winding Resistance/Phase @ 75 °C | 0.43 Ohms   |
| Stator Outer Radius              | 81.8 mm   |
| Stack Length                     | 72 mm   |
| Winding Conductors               | 68 turns of 2 conductors of AWG 20 wire on each pole. |
| Peak Winding Current             | 15 A  |
| Multiple Excitation Mode         | Two-Phase, Short-Flux-Path Mode                       |

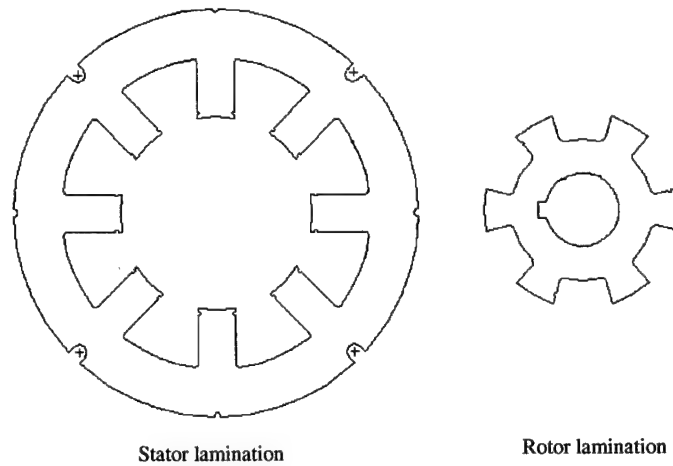


Figure 3.8. Stator and rotor lamination cross-section.

### 3.6 Description Of the Experimental Results

#### A. Comparison of Measurements vs. FEA Simulations

The prototype SRM was characterized using 2D FEA studies. A deviation was expected between the flux-linkage characteristics from FEA and those from actual measurements at the unaligned position. From this point of view, a 20 % margin was incorporated between the desired peak power rating and the actual design value. The single-phase measurements are based on the procedure described in [6], while the multi-phase measurements are based on the new approach presented in Chapter 4 for the multiply-excited 6/4 and 8/6 SRM. The flux data were obtained by integrating the back emf equation using the measured terminal voltages and phase currents.

The phase resistance was measured using a digital multi-meter as well as by the V/I method. The latter was also used for resistance measurements in order to determine the average winding temperature rise. The torque was measured using a Lebow torque meter/transducer.

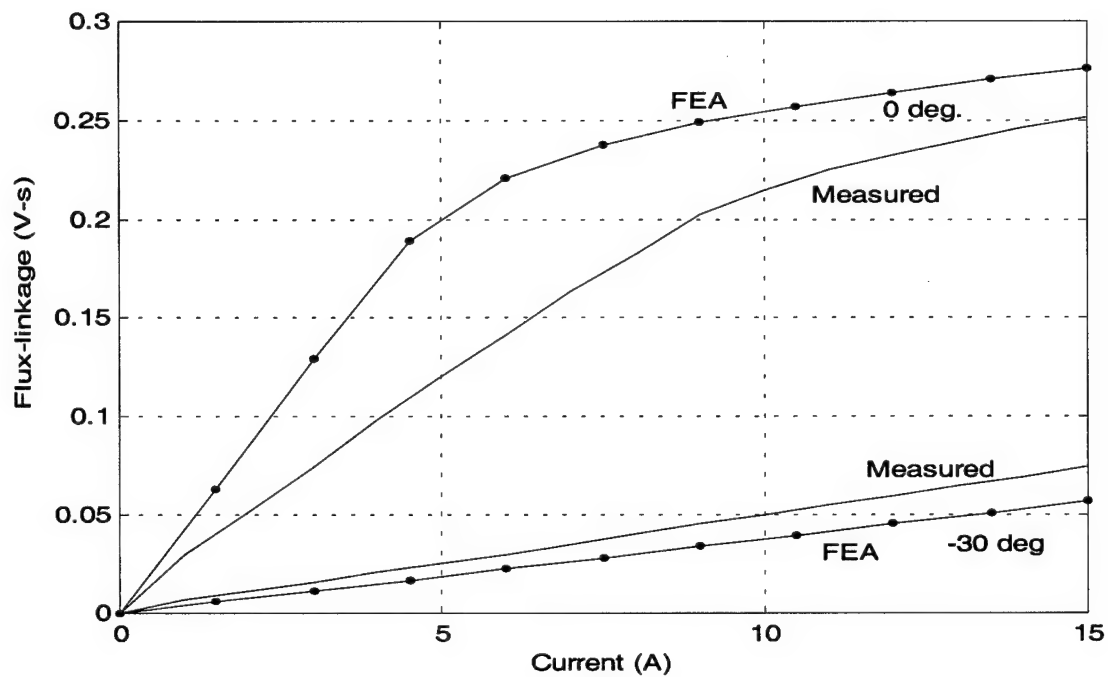
Measurements were also carried out for the torque characteristics under single-phase excitation as well as multi-phase excitation (short and long flux path modes). The torque characteristics under the various modes are included and discussed in detail in Chapter Four. Figures 3.9 (a) and (b) show the comparative torque and flux-linkage characteristics under single-phase excitation obtained using FEA and measurements. The observed difference between the FEA and measured characteristics deviates from the usually expected one of difference occurring in 2D FEA results from the actual flux-linkage characteristics at the unaligned position. In this case, a comparatively greater deviation is observed at the aligned position. This pattern of deviation could be attributed only to a difference between the specified and actual coil turns of about 20%. Also, a phase resistance measurement shows that it is less than the calculated value of 0.43 ohms for a winding conductor of gage 20 by about 20 %. The actual resistance value is about 0.34 ohms. However, this possible reduced number of turns in the prototype could not be verified with the manufacturer.

Figure 3.10 shows a plot of the measured flux-linkage characteristics for the 8/6 SRM under single-phase excitation. Figure 3.11 shows the measured average winding temperature rise when a phase is carrying the peak phase current of 15 A. This verifies the short-time overload capability of the designed SRM, since the temperature rise during this overload is well within the allowable temperature rise for the Class F insulation used in the machine.

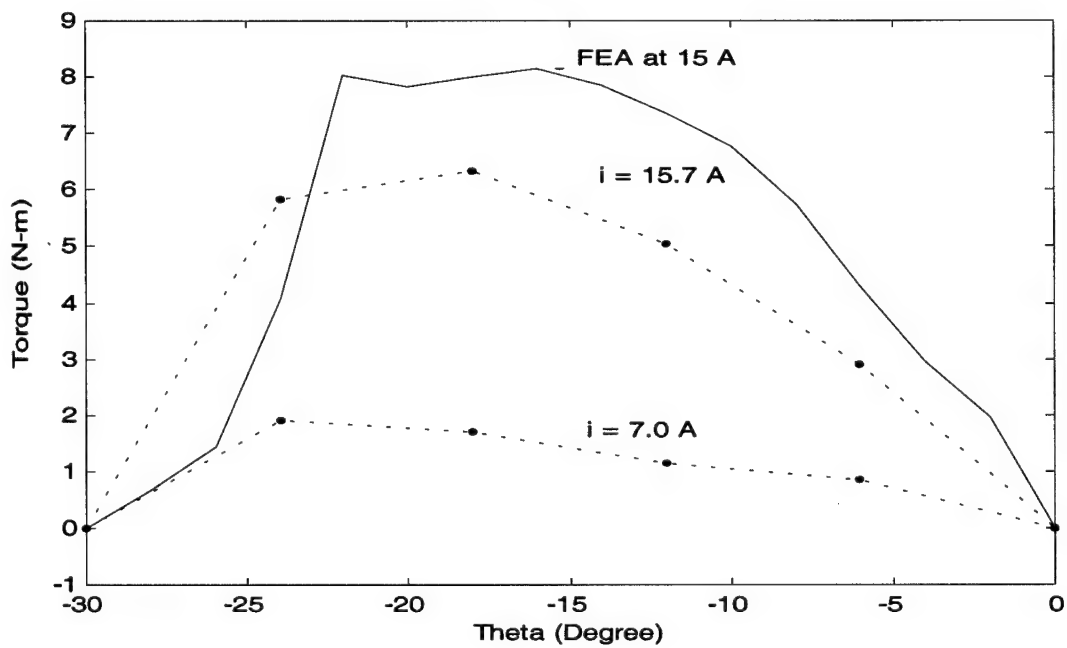
## References

- [1] A. Michaelides and C. Pollock, "Short Flux Paths Optimize the Efficiency of a 5-Phase Switched Reluctance Drive", *Conference Proceedings of the 1995 Annual Meeting of the IEEE Industry Applications Society*, pp.286-293, Orlando (FL), October 8- 12.
- [2] B.C. Mecrow, "New Winding Configurations for Doubly Salient Reluctance Machines", *IEEE Transactions on Industry Applications*, Vol. 32, No. 6, November-December 1996, pp. 1348-1356.

- [3] Y. Tang, "Switched Reluctance Motor with Fractionally Pitched Windings and Bipolar Currents", *Conference Proceedings of the 1998 Annual Meeting of the IEEE Industry Applications Society*, pp. 351-358, St. Louis (MO), October 12- 15.
- [4] J. Moon, S. Oh, J. Ahn and Y. Hwang, " Switched Reluctance Motor with 2-Phase Excitation", *Conference Proceedings of the 1998 Annual Meeting of the IEEE Industry Applications Society*, pp. 547-552, St. Louis (MO), October 12- 15.
- [5] Swanson Analysis Systems, ANSYS Revision 5.0 Tutorials, 1992.
- [6] T.J.E. Miller, Switched Reluctance Motor and Their Control, Magna Physics Publishing and Clarendon Press – Oxford, 1993.
- [7] E. Mitre Hall, Comprehensive Technical Analysis of Switched Reluctance Motor in Electric Vehicle Propulsion Applications, University of Arkansas, May 2001.
- [8] R. Rabinovici, "Scaling of Switched Reluctance Motors", *IEE Proceedings on Electric Power Applications*, Part B, Vol. 142, N 1, January 1995, Stevenage England, pp. 1-4, 1350-2352 IEPAER.



(a)



(b)

Figure 3.9 (a) Flux linkage-Current, and (b) Torque-Angle characteristics for single-phase excitation.

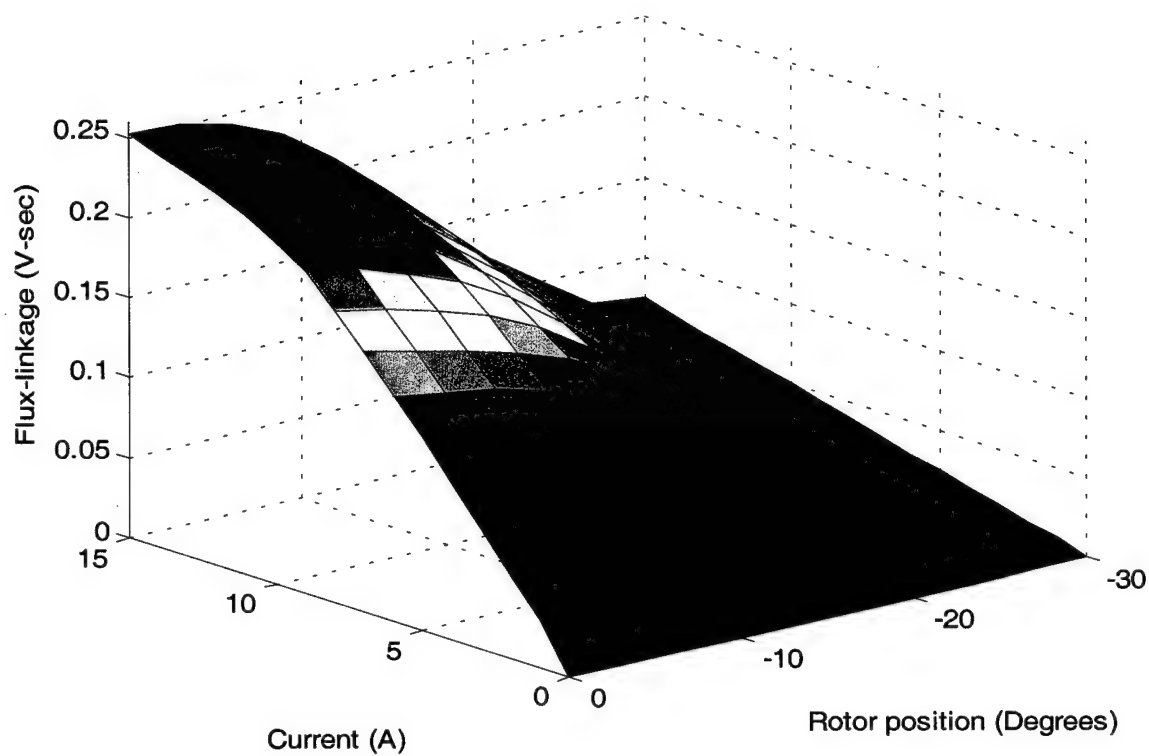


Figure 3.10. Flux-linkage surface for the 8/6 SRM prototype under single-phase excitation.

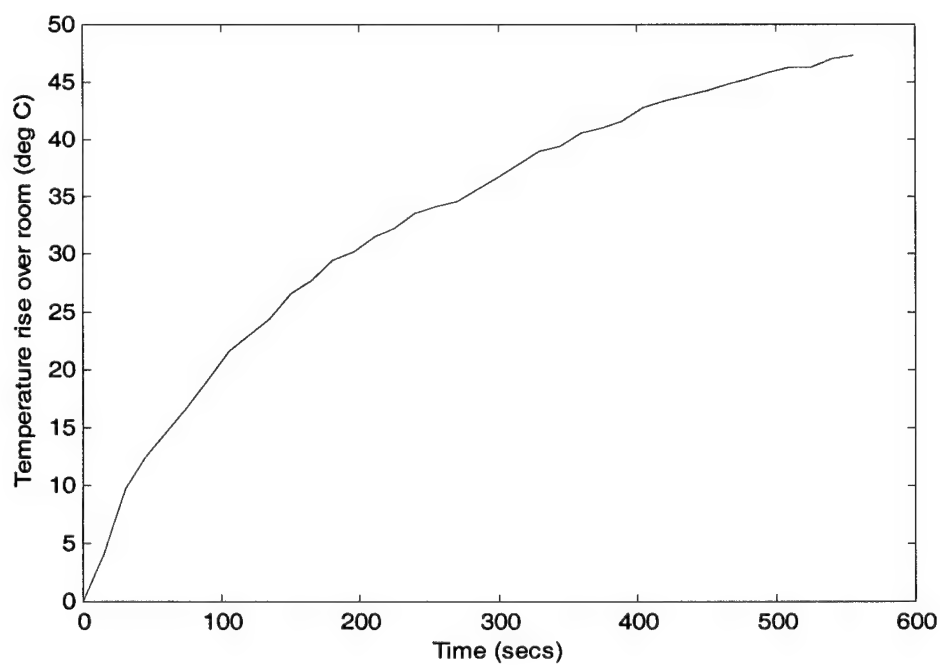


Fig. 3.11 Temperature rise in the windings at the peak phase current of 15 A.

## Chapter Four

# ARTIFICIAL NEURAL NETWORKS FOR MODELING THE MULTIPLY EXCITED SRM

### 4.1 Introduction

This chapter presents a new modeling technique for multi-phase excited SRM that uses FF ANN to account for the mutual flux interaction among excited phases and to compute the torque, while requiring a smaller measured data set as compared to earlier modeling approaches.

In recent years, the need for multi-phase excitation modeling techniques has increased greatly [1] since it has been proposed that multi-phase excitation can substantially improve the performance of SRM in terms of torque ripple, torque density, acoustic noise and efficiency. Moreover, studies on sensorless operation (torque and position) and advanced control strategies increase further the need for a *simple* multi-phase model based on a *small number* of measurements and capable of achieving *high accuracy*.

SRM have been traditionally driven using single-phase excitation; i.e., exciting only one phase at a time. However, even a SRM designed to operate under single-phase excitation, such as the three-phase 6/4 SRM, operates under multi-phase conditions during the commutation from one phase to the next one. An accurate model of the SRM should consider the influence of the currents in the other excited phases. In the past, single-phase excitation modeling techniques have been extended using superposition to model the SRM multi-phase operation due to several reasons; namely, they are simpler to implement, faster to compute, and require a smaller number of data points than multi-phase excitation modeling techniques. This type of approximation is frequently adequate as a first approach to model the SRM dynamic behavior and to study simple control strategies. However, superposition principles will not yield high accuracy due to the non-linearities of the system as well as the existence of mutual interactions between the phases. Hence, proper multi-phase excitation modeling techniques should be implemented when requiring higher accuracy.

In the past, many techniques have been reported for on-line calculation of the SRM performance variables and parameters as function of the terminal variables (i.e., current, position) under the single-phase operating mode for example [2]. However, it is difficult to develop equations to calculate easily and accurately these performance variables and parameters in the multi-phase excitation case.

The chapter first presents the proposed multi-phase model for the SRM together with a discussion on the behavior of the phase flux and net electromagnetic torque under multi-phase excitation. The measurement techniques used to obtain the data to train the ANN are then described. Finally, the chapter presents the simulation results obtained using the new model and compares them with the results obtained using the single-phase model.

## 4.2 The Multi-Phase Modeling of the SRM

The phase voltage equation of the multiply excited SRM is given as follows:

$$V_j = R_j i_j + \frac{d\lambda_j}{dt} \quad (4.1)$$

where  $V_j$ ,  $R_j$ ,  $i_j$ , and  $\lambda_j$  are the applied voltage, resistance, current and flux linkage of the  $j$ -th phase, respectively.

The flux linkage of the  $j$ -th phase,  $\lambda_j$ , can be expressed as follows:

$$\lambda_j = \lambda_{jj}(i_j, \theta_j) + \sum_{k=1, k \neq j}^{N_{ph}} \lambda_{jk} = \lambda_{jj}(i_j, \theta_j) + \lambda_{jm} \quad (4.2)$$

where  $N_{ph}$  is the number of phases simultaneously excited,  $\lambda_{jj}$  is the self-flux linkage of the  $j$ -th phase,  $\lambda_{jk}$  is the mutual-flux linkage between the  $j$ - and  $k$ -th phases,  $\theta_j$  is the rotor position of the  $j$ -th phase and  $\lambda_{jm}$  represents the total mutual-flux linkage interacting with the  $j$ -th phase. The mutual-flux linkages  $\lambda_{jk}$  are in general non-linear function of the current in all the excited phases and the rotor position with respect to the phase  $j$ .

Since all the other phases and rotor poles have fixed geometric relationships with respect to the phase  $j$ , we only need to consider the rotor positions with respect to the  $j^{\text{th}}$  phase. Thus, the mutual-flux linkage  $\lambda_{jm}$  is a nonlinear function of the relative rotor position and the currents in all the excited phases. By using a model for mapping this function, the mutual-flux linkage portion can be subtracted from the total flux linkage in order to obtain the self-flux linkage portion. From the self-flux linkage, the phase current can be calculated using the flux-linkage characteristic under single-phase excitation. Finally, from the phase currents, the total torque can be then calculated using another non-linear function representing the full mapping of the multi-phase torque with respect to currents in all the excited phases and the rotor position. Fig. 4.1 shows a generic phase of the multi-phase model.

The sub-sections below discuss in more detail the behavior of the torque and mutual flux interactions between the phases when exciting multiple phases as well as the multi-phase modeling steps and concepts.

#### *A. Mutual-Flux Linkage and Torque Behavior*

The mutual flux interactions between the phases of a SRM are determined by several factors such as the current level in the excited phases, the rotor position and the saturation level of the core, in particular that of the back iron. Also, the SRM may operate in either short or long flux path mode depending on the polarity of the currents in the excited phases. Suppose that we consider only two adjacent phases excited simultaneously. In the case of the short-flux-path mode, the fluxes in the two adjacent phases have opposite directions of flow into the back iron (see Fig. 4.2). Thus, the majority of the flux tends to concentrate in the region of the back iron between the two phases (see Fig. 4.2). In the long flux path mode, the fluxes have the same direction of flow (see Fig. 4.2). Thus, the fluxing pattern remains the same as the single-phase excited case. The excitation of the two phases simultaneously drives the back iron further into saturation than in the single-phase excitation case.

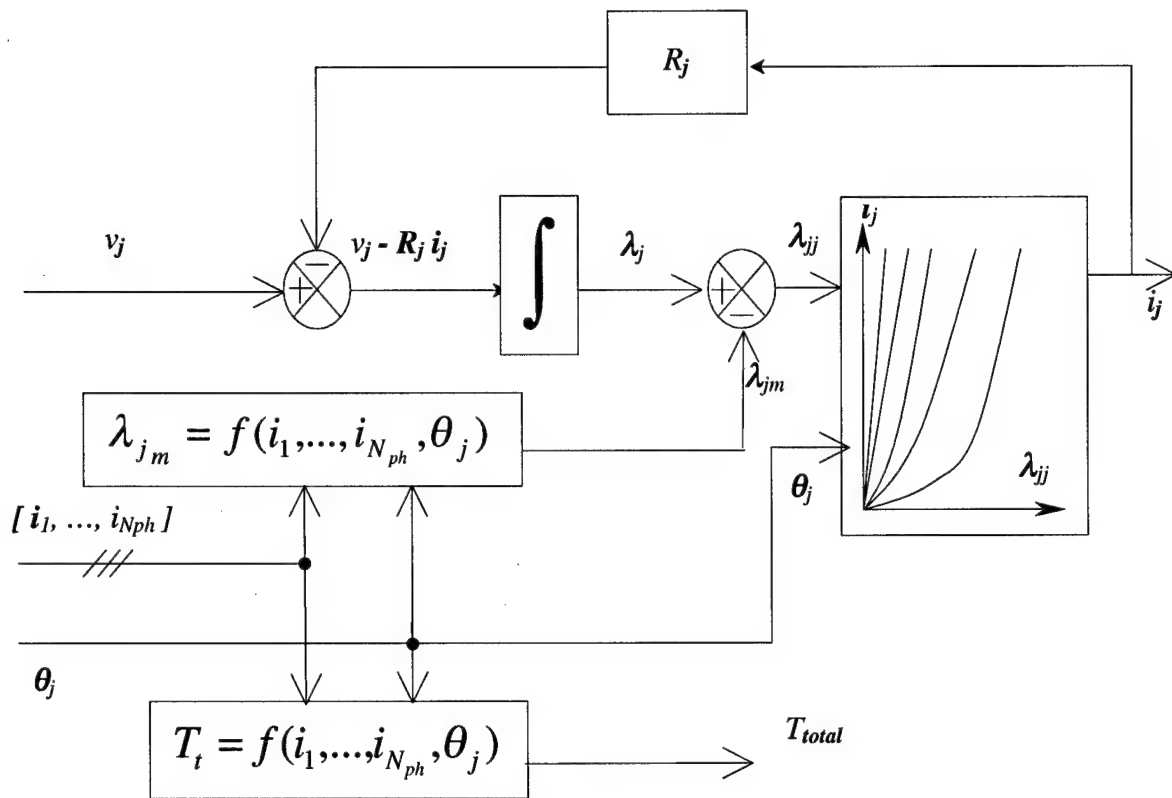


Figure 4.1. A generic phase model of the multi-phase excited SRM.

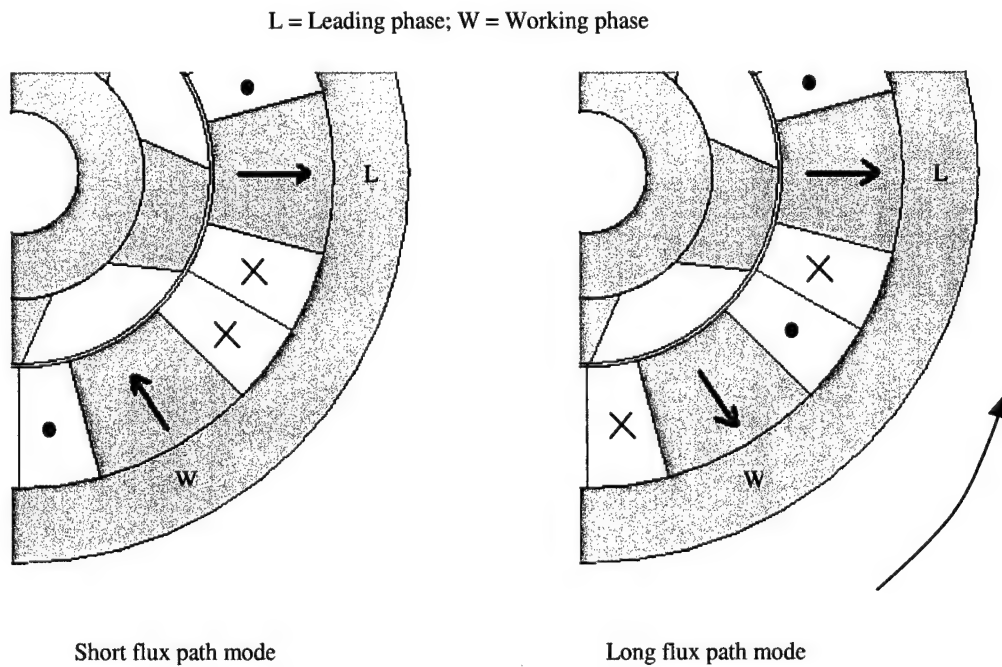


Figure 4.2. The short- and long-flux-path modes of operation when exciting two phases.

This chapter will later introduce the concept of the mutual flux interaction function  $M(i_1, i_2, \dots, i_{Nph}, \theta)$ , which is the non-linear function determining the mutual interaction between the excited phases. The function  $M$  may produce either an increase or decrease in the net phase flux depending on the current levels in the excited phases  $i_1, i_2, \dots, i_{Nph}$  and the rotor position  $\theta$ . In the case of the short-flux-path mode at low current levels, the change in the fluxing pattern under multi-phase excitation results in increasing the net flux in each phase due to the decrease in the reluctance of the flux path (due to a shorter length). At high current levels, however, the net flux decreases due to the saturation of the back iron between the two phases.

For the long-flux-path mode of the operation, the net flux reduces at all current levels. The peak level of mutual interaction is lower in the short-flux-path case as compared to the long-flux-path case. This difference in interaction level between the two modes will be more pronounced when increasing the number of participating phases. As a result, the changes in the mutual flux and torque are smaller in the short-flux-path case than in the long-flux-path case. Fig. 4.3 illustrates these points through a plot of the function  $M$  at a rotor position of  $-7.5^\circ$ , which was derived using ANSYS<sup>TM</sup>-FEA simulations of a 6/4 SRM. It can be observed that  $M$  is positive for certain current levels in the short-flux-path mode. For all other conditions, it is negative.

The torque produced by each phase is a function of the flux level in the air-gap portion associated with that phase. The torque produced by each of the conducting phases also changes since the flux level of a phase changes with the presence of currents in the other phases. This torque change follows the pattern of the change in the flux. Since the mutual flux interactions are in general higher in the long-flux-path mode, the deviation in net torque from that obtained by superposition of single-phase values is greater in the long-flux-path excitation mode. Hence, the principle of superposition should not be used to model the SRM under multi-phase excitation. Similar behavior of SRM under multi-phase excitation has been recently reported in [3].

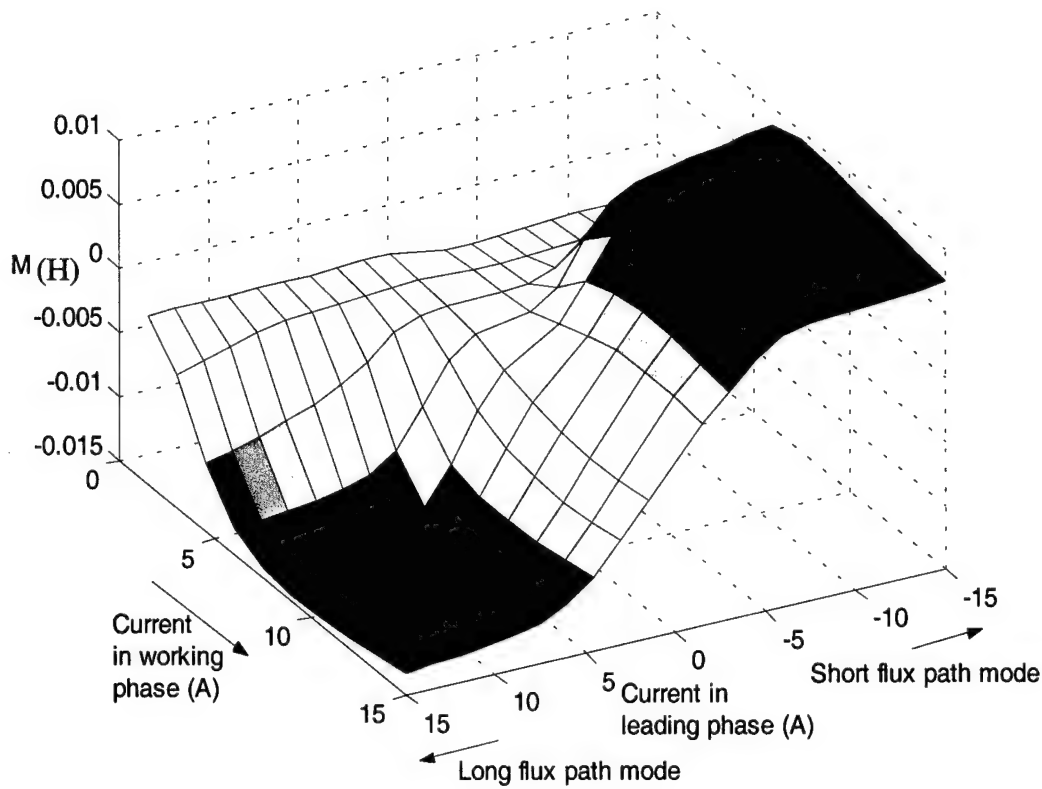


Figure 4.3. The variation of the mutual flux interaction function  $M$  with phase winding currents at  $\theta = -7.5^\circ$ .

In this report, the case of  $N_{ph} = 2$  has been considered. Different non-linear function approximation techniques can be implemented in order to represent the mutual interaction  $M(i_1, i_2, \theta)$  and total torque  $T(i_1, i_2, \theta)$  functions. Most approximation techniques when applied to these functions would require *a large number of data points* to get the required fit to the non-linear behavior of the SRM. Also, these techniques would involve tedious calculations (several computations of trigonometric functions and surface integrals at each time-step) [4] for torque calculation that are difficult to implement efficiently for simulations and on-line estimation. For example, one can use a Fourier series like formulation to express the variation of the  $M$  function with rotor position. Knowing the single-phase characteristics of the phases, we need the  $M$  values as a function of current in the 2 excited phases (surfaces like that in Fig. 4.3) at a minimum of 4 rotor positions to compute the coefficients of this Fourier series.

At each rotor position, we need 10 steps of one phase current  $\times$  10 steps of the other current or 100 measurements; hence, we require a total of 400 measurements. These numbers are based on ANSYS<sup>TM</sup>-FEA studies aimed at representing these interaction functions for several SRM configurations. In some cases, data at more positions are required to be able to use a Fourier series representation. For estimating the torque, it is essential to compute the total co-energy of the system by consideration of the self and mutual fluxes. Other modeling methods must be sought to reduce the large number of measurements required to obtain the model data and simplify the computations. In particular, two FF ANN have been applied that are expected to require a substantially reduced data set and can be trained to generalize and estimate the behavior of the mutual interactions and torque.

The role of the flux ANN is to provide static mapping between the currents in the two excited phases, the rotor position and the mutual flux interaction function. Likewise, the torque ANN is used to provide static mapping between the two currents, the rotor position and the electromagnetic torque developed in the SRM.

#### B. The Mutual Flux Interaction Function $M(i_1, i_2, \theta)$

A multiply excited magnetic system (in this case, the SRM under multi-phase excitation) is governed by the following relationship among the flux linkage  $\lambda_i$ , the phase current  $i_i$ , the total system coenergy  $W_c$ , and the total system field energy  $W_f$ .

$$\sum_{j=1}^{N_{ph}} \lambda_j i_j = W_c + W_f \quad (4.3)$$

In the case of a SRM with two phases simultaneously excited ( $N_{ph} = 2$ ), (4.3) can be expressed as:

$$\lambda_1 i_1 + \lambda_2 i_2 = W_c + W_f \quad (4.4)$$

The total phase fluxes  $\lambda_1$  and  $\lambda_2$  are divided into *self-flux linkages* ( $\lambda_{11}$  and  $\lambda_{22}$ ) and *mutual-flux linkages* ( $\lambda_{12}$  and  $\lambda_{21}$ ) as follows:

$$\lambda_l = \lambda_{l1} + \lambda_{l2} \quad \text{and} \quad \lambda_2 = \lambda_{22} + \lambda_{21} \quad (4.5)$$

Based on these equations, a *mutual flux interaction function*  $M$  can be defined as follows:

$$\lambda_{l2} = M(i_l, i_2, \theta) i_2 \quad \text{and} \quad \lambda_{2l} = M(i_l, i_2, \theta) i_l \quad (4.6)$$

Then, (4.4) can be rewritten as

$$\lambda_{l1} i_l + \lambda_{22} i_2 + 2M(i_l, i_2, \theta) i_l i_2 = W_c + W_f \quad (4.7)$$

The mutual flux interaction function  $M(i_l, i_2, \theta)$  can be calculated as follows:

$$M(i_l, i_2, \theta) = \frac{W_c + W_f - \lambda_{l1} i_l - \lambda_{22} i_2}{2 i_l i_2} \quad (4.8)$$

To obtain the plot of Figure 4.3,  $W_c$ ,  $W_f$ ,  $\lambda_{l1}$  and  $\lambda_{22}$  were obtained at each current level and rotor position using ANSYS<sup>TM</sup>-simulations.

### C. ANN-based Representation of $M$ and Torque

The SRM operates in strokes over the conduction angle  $\theta_{ST}$  given by:

$$\theta_{ST} = \frac{360^\circ}{m N_R} \quad (4.9)$$

where  $m$  is the number of phases and  $N_R$  is the number of rotor poles. The positive torque capability of each phase is from  $\theta = \frac{-180}{N_R}^\circ$  to  $0^\circ$  where  $\theta$  is the rotor position with respect to a phase measured

between the centers of the rotor and stator poles, respectively. To use a FF ANN to represent the mutual flux interactions between the SRM phases, we consider the influence of the leading phase on the working phase (in the direction of rotation) and vice-versa for rotor positions  $\theta$  at the working phase varying between  $\frac{-180}{N_R}^\circ$  to  $0^\circ$ . Correspondingly, the rotor position at the leading phase varies between

$$\left( \frac{-180}{N_R} + \theta_{ST} \right)^\circ \text{ to } \theta_{ST}^\circ.$$

For the three-phase 6/4 SRM considered here, the flux and torque ANN will account for mutual flux interactions between the leading and working phases as well as the electromagnetic torque output for  $\theta$  varying between  $-45^\circ$  to  $0^\circ$  at the working phase. The rotor position with respect to the leading phase will correspondingly vary between  $-15^\circ$  to  $30^\circ$ . This choice of angles will not only allow representing the mutual flux interactions and the electromagnetic torque from the minimum possible turn-on angle at the working phase but also allows for delayed turn-off at the leading phase. For a four-phase 8/6 SRM, the FF ANN will account for the mutual flux interactions within an angle span from  $\theta = -30^\circ$  to  $0^\circ$  when the rotor position with respect to the leading phase varies between  $-15^\circ$  to  $15^\circ$ .

#### 4.3 ANN Training using Measurements of $M$ and Torque

The FF ANN were first trained using data points computed from ANSYS<sup>TM</sup>-2D simulations. This is adequate for the initial stages of model development, for determining the ANN architecture and for carrying out initial studies. However, it is well known that 2D FEA cannot be expected to give an accurate magnetic characterization of the SRM because of neglecting the end-winding effects [5]. An accurate modeling of the SRM for verification and tuning of the drive performance should be based on measured data. Static measurements were carried out on a three-phase 6/4 SRM designed for single-phase operation as well as a 1-hp four-phase 8/6 SRM prototype, designed for multi-phase operation in the short-flux-path mode for EV propulsion applications.

The multi-phase data were recorded in the FEA simulations at 6 equally spaced intervals of angular position in the range  $-45^\circ$  to  $0^\circ$ , 5 equally spaced intervals of current from 3 A to 15 A in the two phases. The training data thus have  $(6 \times 5 \times 5 = 150)$  points. The single-phase excitation data are composed by 16 equally-spaced rotor positions and 15 equally-spaced current phase resulting in 240 more data points. Remember that the Fourier series based representation requires 400 measured points in addition to the single-phase excitation data.

Also, the multi-phase torque would have to be computed using complex formulations that are difficult to implement either in the off-line or on-line mode [4]. In the off-line case, the torque under multi-phase excitation would be pre-computed and stored as 3D lookup tables. At the phase current and rotor position values measured from the drive, the torque would then have to be computed by on-line interpolations. On the other hand, the on-line case would be more difficult to implement due to requiring estimation of flux-linkage characteristics as well as torque computation on-line.

The ANN were trained and their structure was optimized using MATLAB<sup>TM</sup>. For the FF ANN mapping of the  $M$  function to the terminal variables in the 6/4 SRM case, the desired performance accuracy was obtained using an ANN having an input layer of 3 neurons, two hidden layers having respectively 3 and 2 neurons (with log-sigmoid activation functions), and an output layer of 1 neuron (having a linear activation function). Figure 4.4 below shows the  $M$  function prediction using the FF ANN at different current levels in the working and leading phases as function of rotor position. It is noted that the  $M$  function is always negative meaning that the phase flux will always be reduced in the 6/4 SRM operating under multi-phase excitation and long-flux-path mode. Similarly, the torque ANN has an input layer of 3 neurons, a hidden layer of 7 neurons and an output layer of 1 neuron. Figure 4.5 shows the topology of the torque prediction FF ANN. Figure 4.6 shows the electromagnetic torque prediction using the FF ANN at different current levels in the working and leading phases as function of the rotor position. The torque values were obtained using FEA.

In order to take the static measurements, a test/measurement bench was set up as illustrated in Figure 4.7 that also illustrates conceptually the electrical circuit for the measurements. The torque measurements were made using a Lebow torque meter at 9 rotor positions and 5 levels of phase current at equally spaced intervals resulting in  $5 \times 5 \times 9 = 225$  measurements for the multi-phase excitation case. The single-phase excitation case was characterized using  $16 \times 5 = 80$  measurements; that is a total of 305 measurements.

Figure 4.8 shows the static torque measurements on the four-phase 8/6 SRM when operated in the short- and long-flux-path modes.

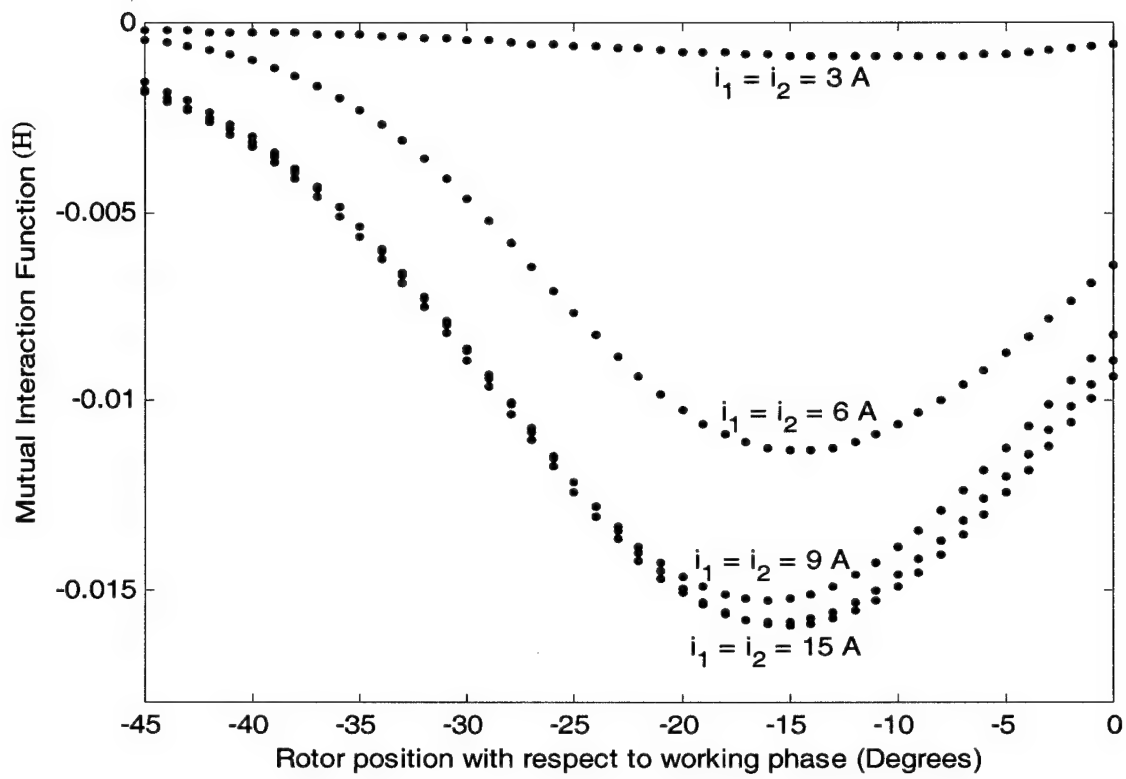


Figure 4.4 The output of the FF ANN for estimating the mutual flux interaction function at different current levels as function of the rotor position with respect to the working phase.

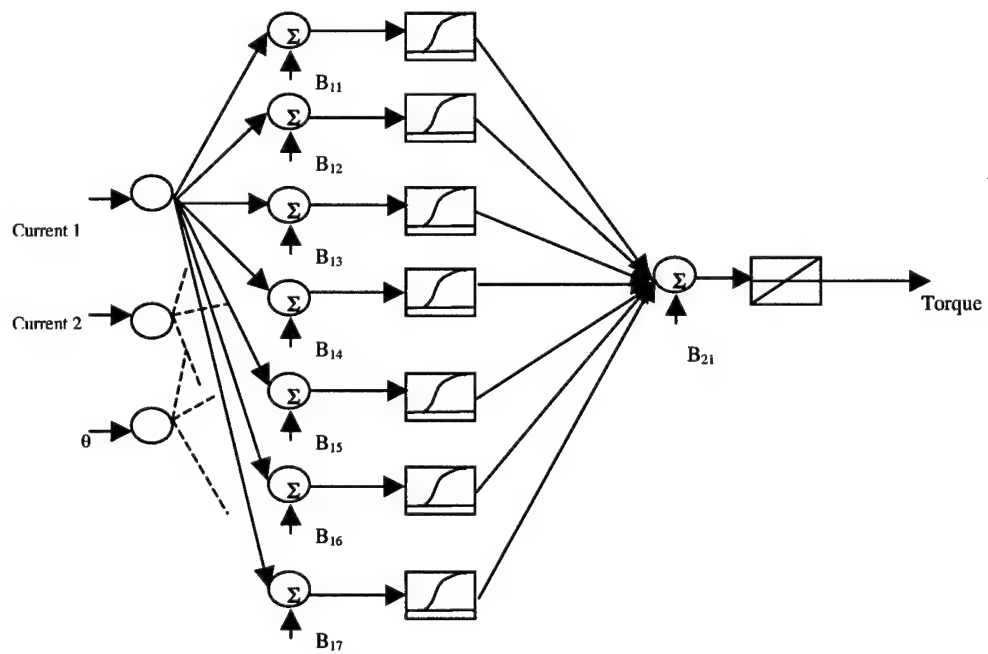


Figure 4.5 The FF ANN used for torque mapping.

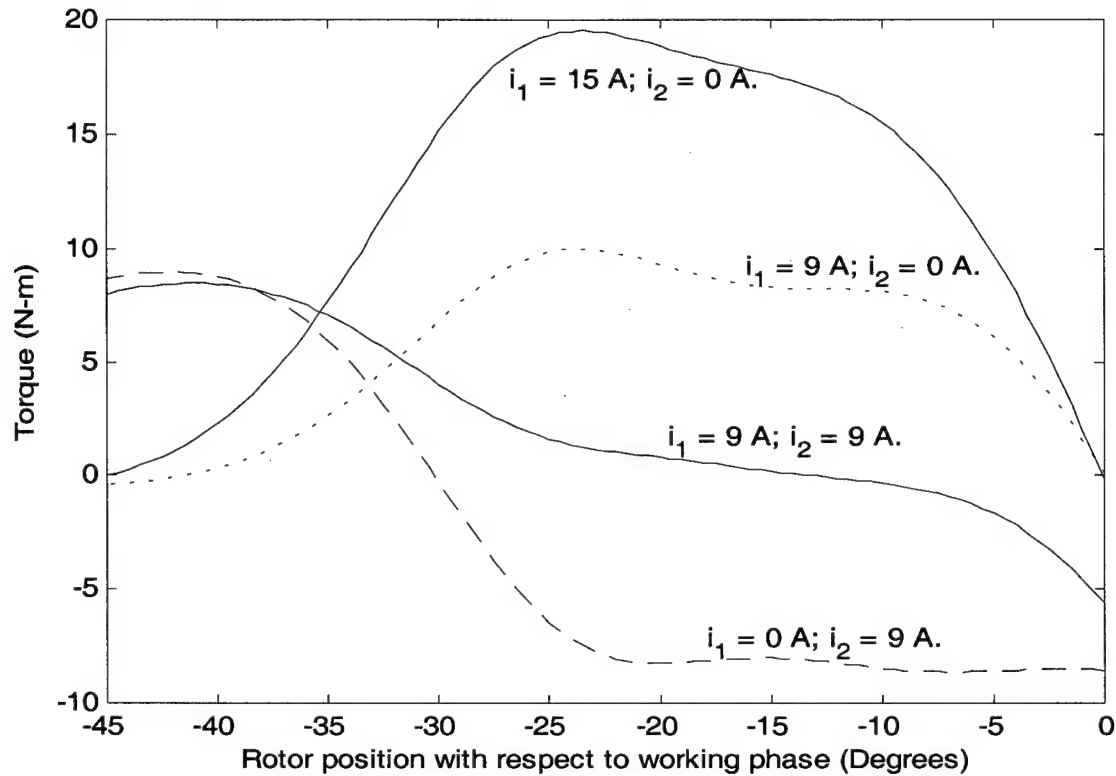


Figure 4.6 The output of the FF ANN for estimating the torque at different current levels as function of the rotor position with respect to the working phase.

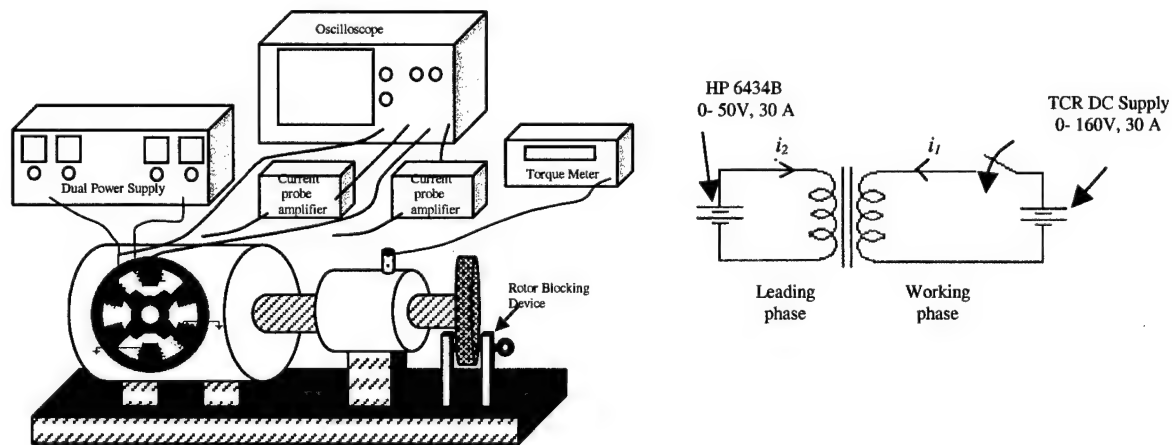


Figure 4.7. Test/measurement bench for torque and mutual-flux linkage measurements.

Since this SRM was designed to take advantage of the short-flux-path mode concept, the torque output is diminished in the long-flux-path mode due to deep saturation of the back iron. The torque value that would be obtained by using superposition of the torque of the working and leading phases operated independently is also shown to substantiate the fact that superposition cannot be used for modeling the

multiply excited SRM. In addition, the single-phase excitation characteristics for the leading and working phases are shown for completeness. The measured torque data were used to train the FF ANN to provide static mapping between the terminal variables and the developed electromagnetic torque. The desired performance accuracy of the mean squared error of  $[0.0005 \times (\text{the peak expected torque value})^2]$  was obtained using a FF ANN having the same topology as that one in the 6/4 SRM case. Fig. 4.9 shows the performance of the FF ANN for the 8/6 SRM prototype in the torque estimation task. The single-phase flux-linkage characteristics at different positions were obtained by single-shot applications of a dc voltage source to the phase.

The SRM phase terminal voltages and currents, recorded using a Tektronix™ TDS 460 four-channel digitizing oscilloscope, were used to compute the flux linkages as function of current. For computing the multi-phase characteristics, the dc voltage is simultaneously applied to two phases (see Figure 4.7). The voltage sources can be turned on simultaneously or they can be turned on one at a time. One of the voltage sources is set to get the desired current level in one of the phases. Then, the other voltage source is turned on so that the current in that phase increases from zero to the peak phase current. Even though the current in the first phase will vary slightly due to the mutual interactions, it is acceptable since the idea is to sample the space of the function  $M$  to use these values for training of the ANN. The terminal voltage and currents of the two phases are recorded and used to compute the phase fluxes (see Figure 4.10). Since the single-phase characteristics are already known, we can then compute the mutual flux and  $M$  value. For measuring  $M$ , we need only 5 current levels in one phase (say leading phase) at 6 rotor positions. The current is set up in the other phase (say the working phase) by switching on the dc voltage source whose voltage is selected so as to set up the peak phase current based on knowing the phase resistance value. In this case, each switching of the dc voltage source at the working phase will provide data to measure the  $M$  function values along trajectories parallel to the working phase current axis on surfaces such as that in Figure 4.3. Thus, we need  $5 \times 6 = 30$  measurements to characterize  $M$  completely.

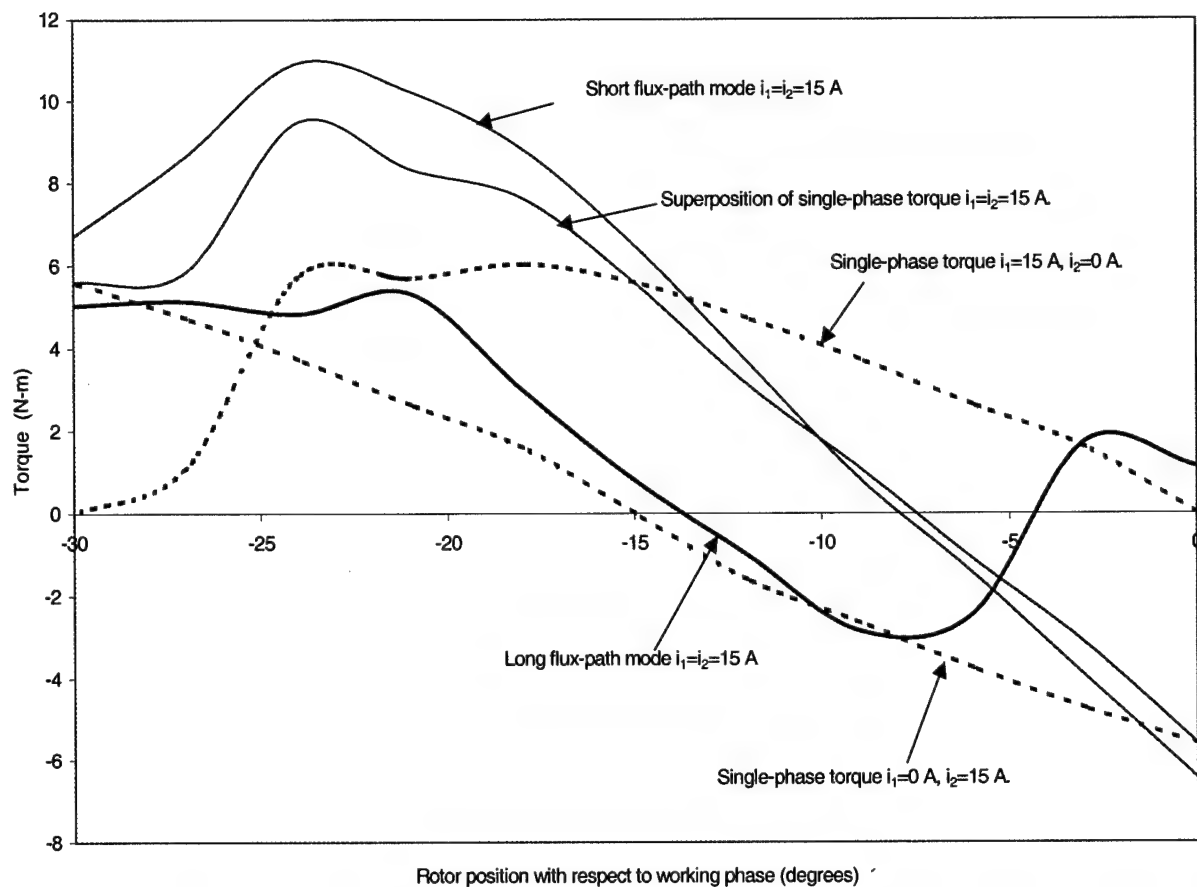


Figure 4.8. Static torque measurements of the four-phase 8/6 SRM prototype (1=working phase, 2=leading phase).

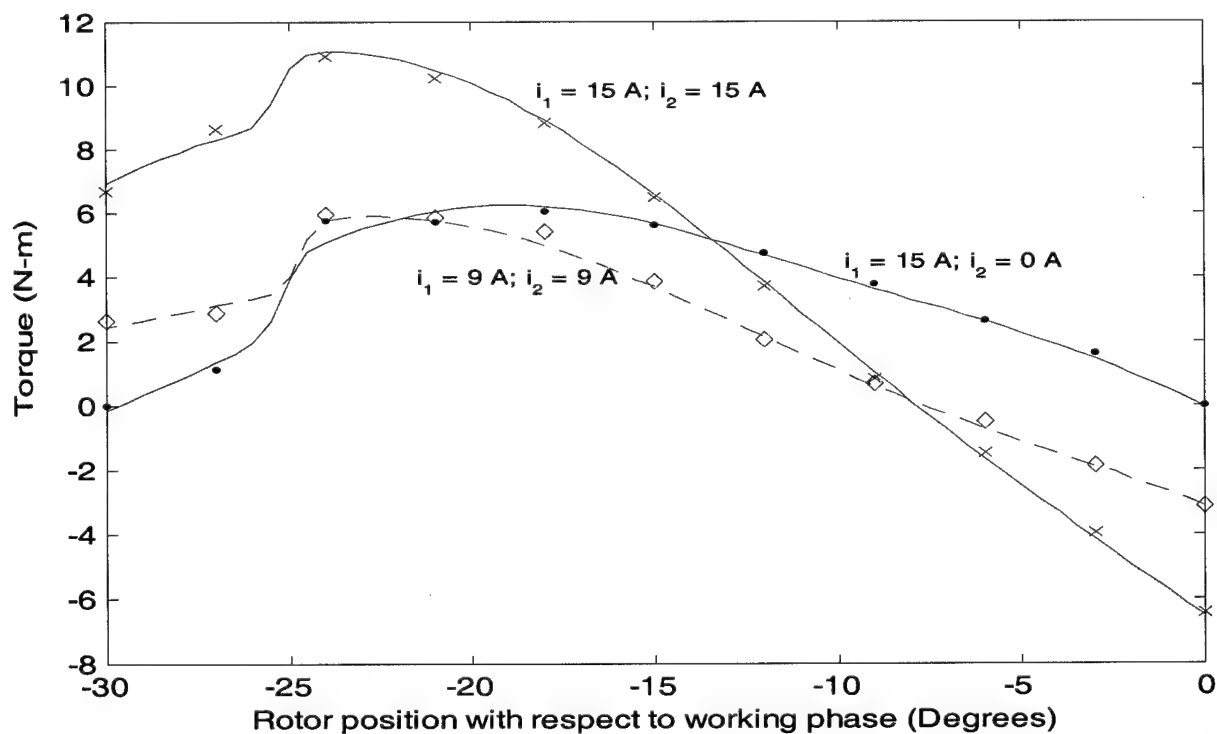


Figure 4.9. Performance of the FF ANN for static torque mapping in the four-phase 8/6 SRM case.

In Figure 4.10, the current in (leading) phase 2 was set at a fixed level. Then, a voltage was applied to the (working) phase 1. As a result, the current in phase 1 increases from zero and correspondingly, the current in phase 2 undergoes a change due to the mutual flux interactions. The voltage source applied to phase 2 changes to maintain the current at the set current limit. Such waveforms were recorded at each measurement point and used to calculate the phase flux linkages under these conditions. Since the self-flux linkages have been already recorded, we can use (4.8) to compute the  $M$  function.

These computed values at different current levels and rotor positions are then used to train the FF ANN for mapping the terminal variables to the  $M$  function values. The desired performance accuracy was obtained with a FF ANN having an input layer of 3 neurons, two hidden layers of respectively 5 and 4 neurons, and an output layer of 1 neuron. Figure 4.11 illustrates the performance of the FF ANN in mapping the SRM terminal variables to the measured mutual flux interaction functions. It is noted again that  $M$  has negative and positive values meaning that the effect may be to either decrease or increase the phase flux. As anticipated from Figure 4.3, the mutual interaction functions cannot be “fitted” by a single mathematical expression (e.g., Fourier series). Therefore, the ANN provides better performance than the other methods. Table 4.1 summarizes the number of measured points in the ANN-approach as compared to the conventional techniques for the two-phase excitation case. With higher number of excited phases, the number of measurement and storage points required with the conventional methods for torque mapping would scale up by one more order (e.g., 10000 points of measurement and storage would be required in the three-phase excitation case). In the case of the mutual interaction function, the number of points would scale to similar values since a Fourier series approximation to interpolate between the function values at 4 positions would no longer be applicable.

#### **4.4 Simulations And Results**

The described multi-phase model was applied in simulations to study the dynamic performance of the SRM drive since a fully operational SRM drive was not available in the laboratory. The full model including the torque and mutual flux interaction function ANN was implemented in SIMULINK<sup>TM</sup>.

**Table 4.1 Summary of Conventional and ANN-approach**

|                             | Conventional (interpolation)   | ANN  |
|-----------------------------|--|--|
| Mutual Interaction Function | 6 points for single phase plus 40 points with two phases. Can use spline function plus Fourier Series. 400 points storage. | 6 points for single phase plus 30 points for two phases.   |
| Torque                      | About 1000 points of measurements (or computation) and storage. Must use spline function.                                  | 80 points for single phase plus 225 points for two phases. |

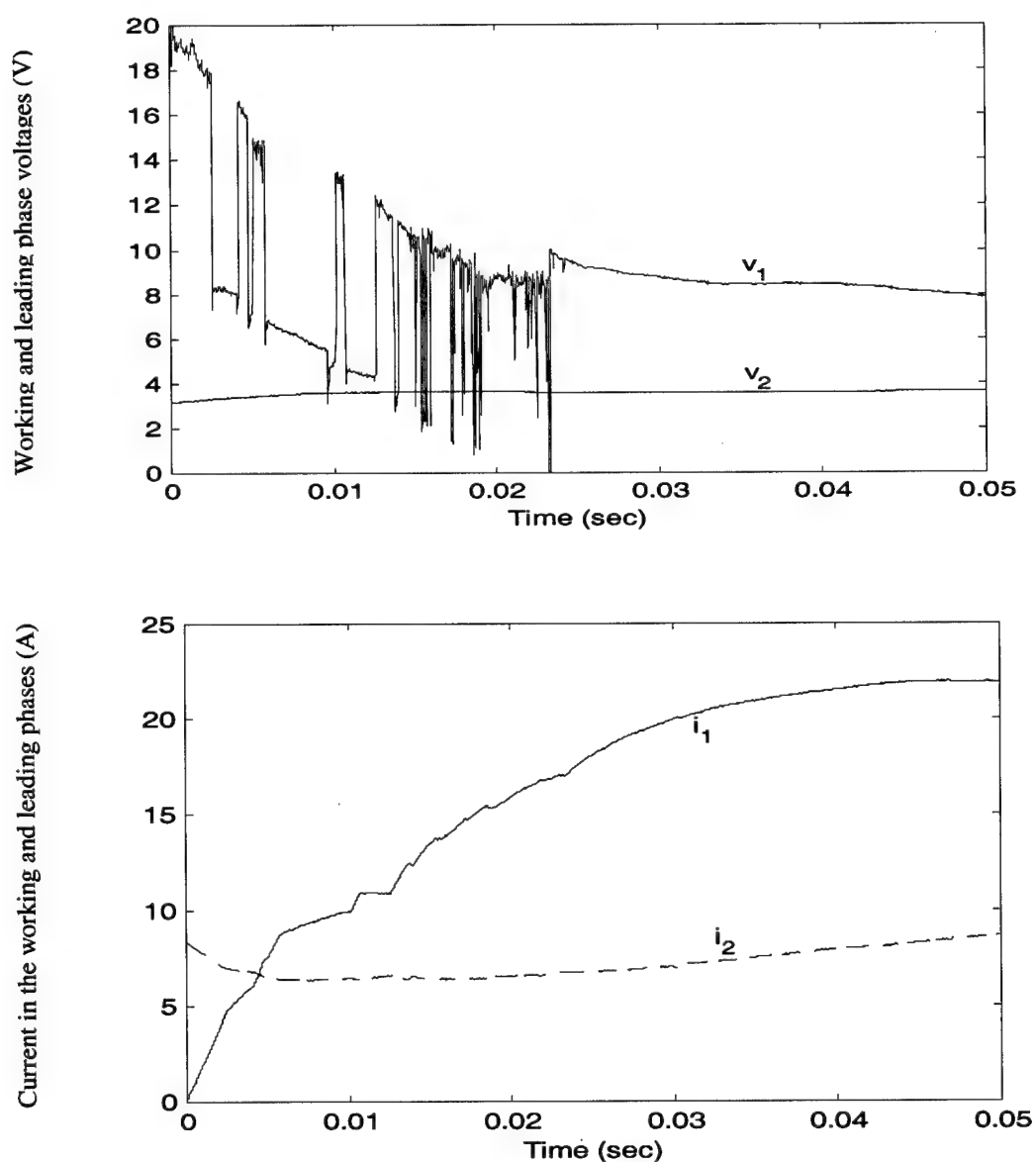


Figure 4.10. Applied voltages and currents during the  $M$  function measurement at  $\theta = -18^\circ$ .

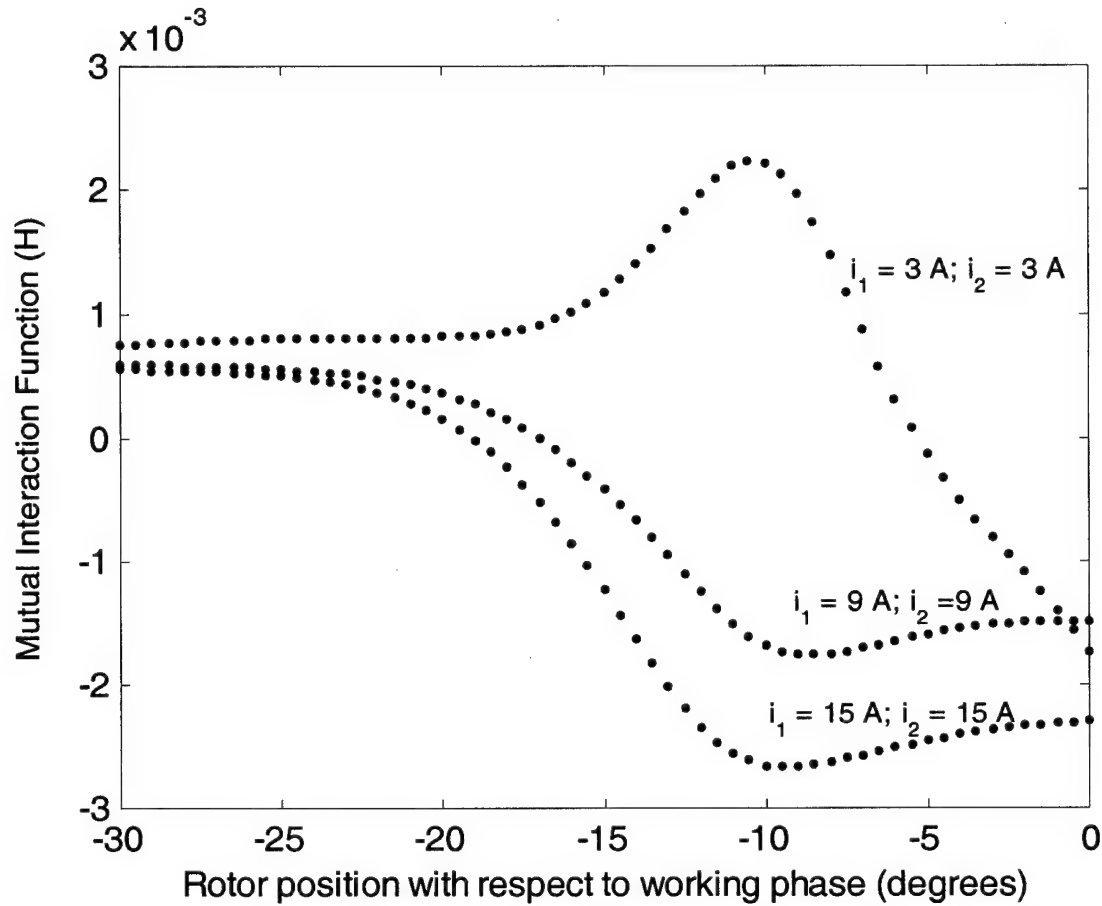


Figure 4.11. Performance of the FF ANN for the mutual flux interaction function mapping in the four-phase 8/6 SRM case.

See Appendix D for the full SIMULINK<sup>TM</sup> model. To explore one of the possible applications for this new model, a simulation study was also implemented for a position sensorless scheme correcting for the mutual flux linkages.

Figure 4.12 shows the simulation results for the torque waveform using the FF ANN based on the measured torque data from the three-phase 6/4 SRM at a speed of 300 rpm. The torque waveforms clearly illustrate the difference between the torque obtained using a multi-phase model and the principle of superposition. Measured torque are not shown in the figure since the torque FF ANN was trained using measured results for a mean squared error value of  $[0.0005 \times (\text{the peak torque value})^2]$ .

The actual average torque developed by the SRM is lower by about 14% when compared to the “superposition” results. Thus, the “ANN” torque provides a far better estimation of the actual SRM torque. The degree of multi-phase operation is also illustrated in Figure 4.12. It is observed that the 6/4 SRM operates with two phases excited simultaneously for certain periods and with only one phase excited for other periods.

Figure 4.12 also shows the simulation results for the position error in the position estimation system based on the multi-phase flux linkage model at 300 rpm. These simulations are based on data obtained from FEA simulations. If the phase flux is not corrected for the mutual flux linkage, the estimated position may deviate from the actual value by about 10° leading to improper SRM operation.

## References

- [1] A. M. Michaelides, C. Pollock, “Short Flux Paths Optimize the Efficiency of a 5-Phase Switched Reluctance Drive”, *Conference Proceedings of the 1995 Annual Meeting of the IEEE Industry Applications Society*, pp.286-293.
- [2] M. Ehsani, B. Fahimi, G. Suresh, J. Mahdavi, “A New Approach to Model Switched Reluctance Motor Drive; Application to Dynamic Performance Prediction, Control and Design”, *Conference Proceedings of the 1998 Power Electronics Specialist Conference*, pp. 2097-2102.
- [3] R. B. Inderka, R. S. Ottl, M. Krehenbrink, R. W. De Doncker, “Effects of Mutual Coupling in Switched Reluctance Machines”, *Electromotion Journal*, Volume 7, No.2, 2000, pp. 96-104.
- [4] A. M. Michaelides, C. Pollock, “Modelling and design of switched reluctance motors with two phases simultaneously excited”, *IEE Proceedings*, Vol. 143, No. 5, pp. 361–370, September 1996.
- [5] T. J. E. Miller, Switched Reluctance Motor and Their Control, Magna Physics Publishing and Clarendon Press - Oxford, 1993.

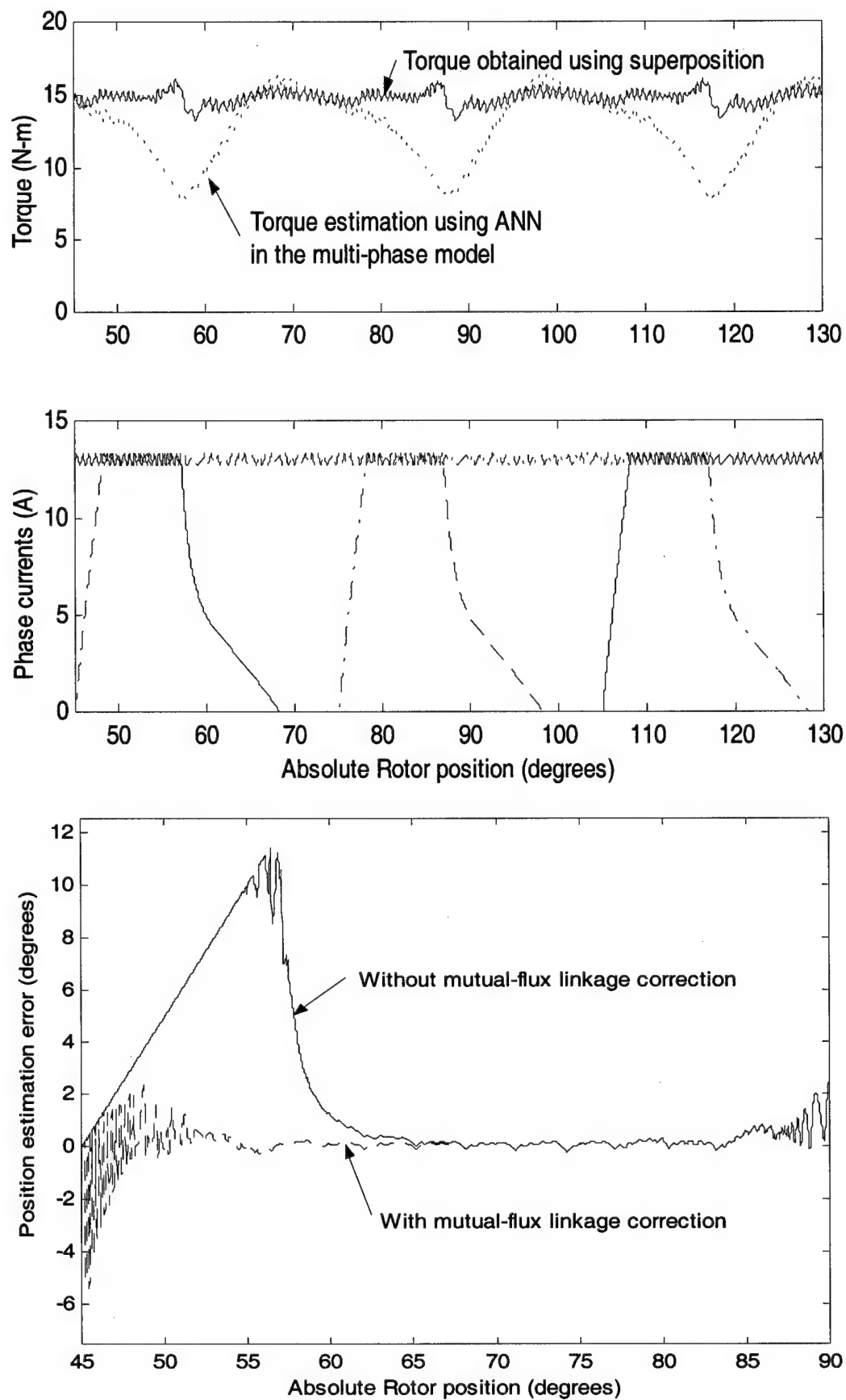


Figure 4.12 Simulation results in the multi-phase mode using superposition and the proposed ANN-based model.

## Chapter Five

### ADAPTIVE ON-LINE TORQUE ESTIMATION

#### 5.1 Introduction

For SRM, the electromagnetic torque has been normally calculated using the flux-linkage characteristics of the motor to compute the co-energy (as a function of rotor position at a constant current) and then applying the classical equation of torque as a function of co-energy. However, the actual flux-linkage characteristics for a particular SRM may be different from that of the designed motor or the initial prototype for which the electromagnetic torque computations have been made off-line. This is because of manufacturing tolerances and the variance in the behavior of magnetic materials among other factors.

Any approach that computes the torque based on standstill measurements of inductance performed on one prototype [1-2] is not adequate when accurate torque feedback is desired for robust dynamic control. The problem is further compounded by the dependence of torque not only on the current level but also on the rotor position. Extensive off-line measurements and calculations would be required to obtain the electromagnetic torque characteristics as function of current and rotor position. The torque data to be stored would be extremely large and the algorithm retrieving the torque from those values stored at discrete current, rotor position and speed values would have to carry out extensive on-line interpolation over non-linear surfaces. Moreover, these techniques would fail with slight changes in the "off-line" characteristics of the machine with aging (e.g., changes in the air-gap or in the magnetic material properties). An improved technique was presented in [3] to estimate the flux-linkage characteristic of the SRM using *on-line* measurements. In [1-3], the electromagnetic torque developed is *indirectly* computed through complex co-energy calculations by integrating the flux-linkage characteristics up to the current level at which the torque is desired between two different rotor positions.

This technique would also involve surface integrals to compute the flux linkage and co-energy to get the actual torque produced in the multi-phase case [4].

In the multi-phase case, results obtained by superposition of the single-phase torque for each conducting phases is unacceptable as shown in Chapter 4 [5]. Thus, techniques such as those in [1-3] would be computationally expensive, especially for the multiply excited SRM case.

ANN-based models providing static mapping between the SRM terminal variables and the electromagnetic torque have been proposed and applied in [5-6]. To overcome the limitations of other techniques, this chapter presents a new and simple technique for estimating the SRM torque in the multi-phase case using an ANN based on the SRM terminal voltage equation. This technique is simpler to apply and can adapt to changes in the SRM characteristics. The proposed technique is intended to allow the ANN SRM model suggested in [5] to adapt and correct its training based on the current characteristics of the individual SRM. In the proposed technique, an ANN estimator is applied to learn the characteristics of the machine using on-line measurements of the phase currents and voltages. The technique does not require any prior off-line simulations or computations; hence, it is simpler to implement than other methods. The system is used to estimate the speed component of the net applied terminal voltage. This component is then used to *directly* calculate the electromagnetic torque developed in the SRM.

An approach for applying ANN for on-line torque estimation has been proposed previously [7]. This approach requires knowledge of the torque in the previous time instants. When such estimation operates in the absence of a torque transducer (the main goal of the estimation is to eliminate the torque transducer), the results obtained are inaccurate. The technique presented here requires no prior knowledge of the torque or the system characteristics. Figure 5.1 shows the role of torque feedback in the control schematic of a SRM. The entire estimation and torque mapping is proposed to be implemented on a fast DSP such as the C6701 expressDSP<sup>TM</sup> from Texas Instruments. This implementation will be described in more detail in the Chapter Six.

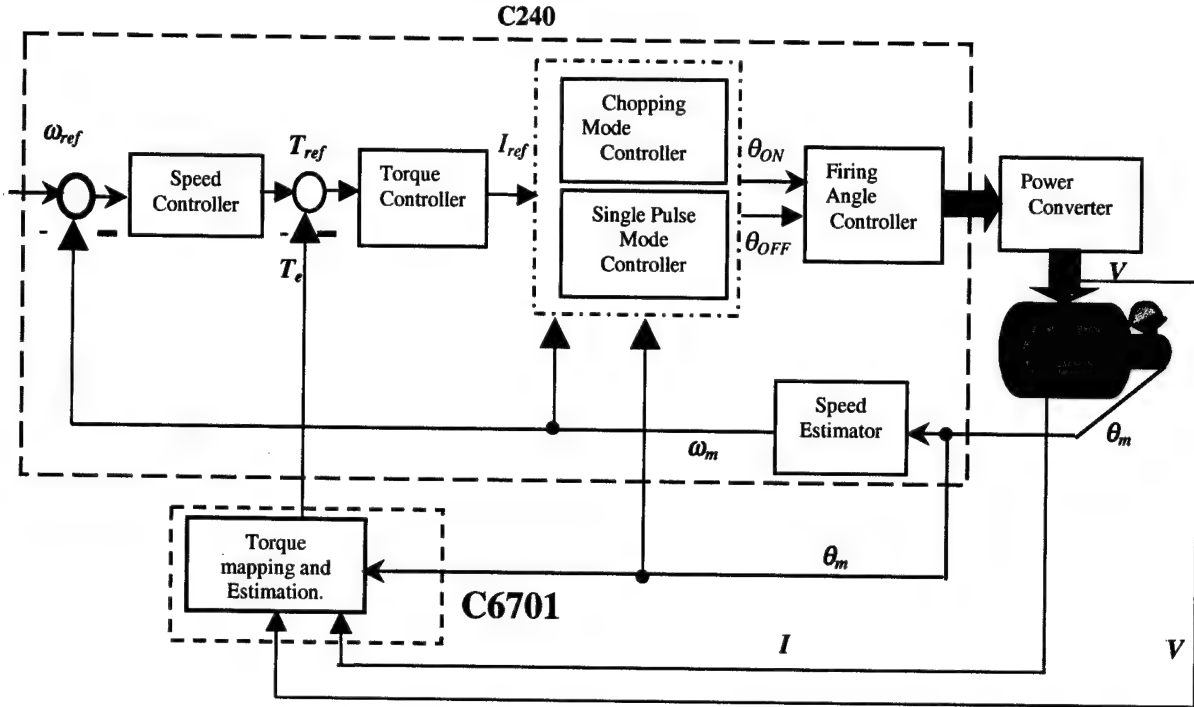


Figure 5.1. The proposed ANN based system on the C6701 to offer torque feedback to the SRM Controller.

## 5.2 Novel Torque Estimation Technique

The terminal voltage equation of the SRM is given by:

$$v = Ri + \frac{d\lambda}{dt}$$

The back emf  $e$  is then given by :

$$e_k = v_k - Ri_k = \left( \frac{d\lambda}{dt} \right)_k = \left( \frac{\partial \lambda}{\partial i} \right)_k \left( \frac{di}{dt} \right)_k + \left( \frac{\partial \lambda}{\partial \theta} \right)_k \left( \frac{d\theta}{dt} \right)_k = e_{ik} + e_{\omega k} \quad (5.1)$$

The ANN topology could be chosen to identify the net back emf  $e$  given by (5.1). The inputs and output of the ANN are chosen as samples at equally spaced time instants like corresponding to a practical digital implementation. To represent  $\left( \frac{d\theta}{dt} \right)_k$ , we use  $(\theta_k - \theta_{k-1})$  and for  $\left( \frac{di}{dt} \right)_k$ , we use  $(i_k - i_{k-1})$ . Since the sampling time  $T$  is constant, the ANN weights adjust to take care of this value, allowing the use of difference values. In the first topology, the speed component of the back emf would be determined by setting the current change  $(i_k - i_{k-1})$  to zero (see Figures 5.1 and 5.2).

However, this choice of ANN topology results in the disadvantage that the ANN output  $e_k$  is presented with binary values (either  $\approx V_{dc}$  or 0) depending on whether the power converter

switches are ON or OFF. Thus, the ANN does not have adequate output patterns to be able to generalize the output for other cases. As a result, this topology does not perform well. To overcome this limitation, we use the observation that the value of  $\left(\frac{di}{dt}\right)_k$  is rich in patterns that vary with the applied voltage, speed, rotor position and current level. Hence, we choose a second ANN topology that has the form of Figure 5.3. In this case the ANN is trained to identify the change in the phase current ( $i_k - i_{k-1}$ ). The ANN emulates the SRM terminal equation re-written as:

$$\left(\frac{di}{dt}\right)_k = \frac{v_k - Ri_k - \left(\frac{\partial \lambda}{\partial \theta}\right)_k \left(\frac{d\theta}{dt}\right)_k}{\left(\frac{\partial \lambda}{\partial i}\right)_k} = \frac{v_k - Ri_k - e_{\omega k}}{\left(\frac{\partial \lambda}{\partial i}\right)_k} \quad (5.2)$$

To determine the speed component of the back emf  $e_{\omega k}$ , we need to determine the back emf  $e_k$  that would set the  $\left(\frac{di}{dt}\right)_k$  to zero. To do this, we set the ANN output to 0 and then invert the ANN to determine the corresponding  $e_k$  (see Figure 5.4). This value is the speed-emf component, say  $e_{\omega k}$ . Having determined the speed-emf, the developed electromagnetic torque at the  $k^{\text{th}}$  time instant is then computed using the following equation:

$$T_{e,k} = \frac{e_{\omega k} \times i_k \times T}{(\theta_k - \theta_{k-1})} \quad (5.3)$$

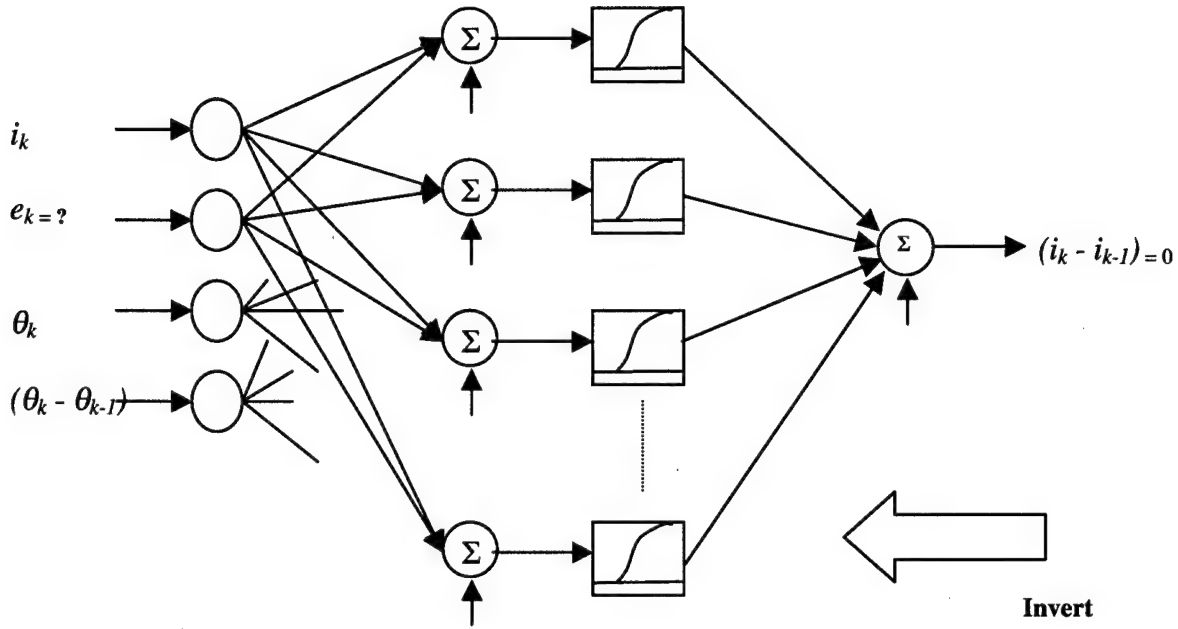


Figure 5.4. ANN inversion for determining the speed emf component.

### 5.3 The Inversion Algorithm

Several techniques have been proposed in the literature for inverting feed-forward ANN [8-9]. In our case, the task is simplified because three of the four input variables are already known at the  $k^{\text{th}}$  instant. Furthermore, we can use the property of electric motors that the speed emf has to be a continuous function of time.

Based on this, we can start with a speed emf value of zero and in each case search for the neighborhood values that minimize the output  $(i_k - i_{k-1})$  of the ANN in Fig. 5.4. Thus, we set values of  $e_{\omega k}$  in the neighborhood of the value in the previous time instant and carry out forward propagation to search for that value of  $e_{\omega k}$  minimizing the output of the ANN. The algorithm for the estimation system was implemented in MATLAB<sup>TM</sup> and estimates the electromagnetic torque developed in a four-phase 8/6 SRM drive system modeled in SIMULINK<sup>TM</sup> (see Appendix D) using on-line measurements of voltage, current and rotor position.

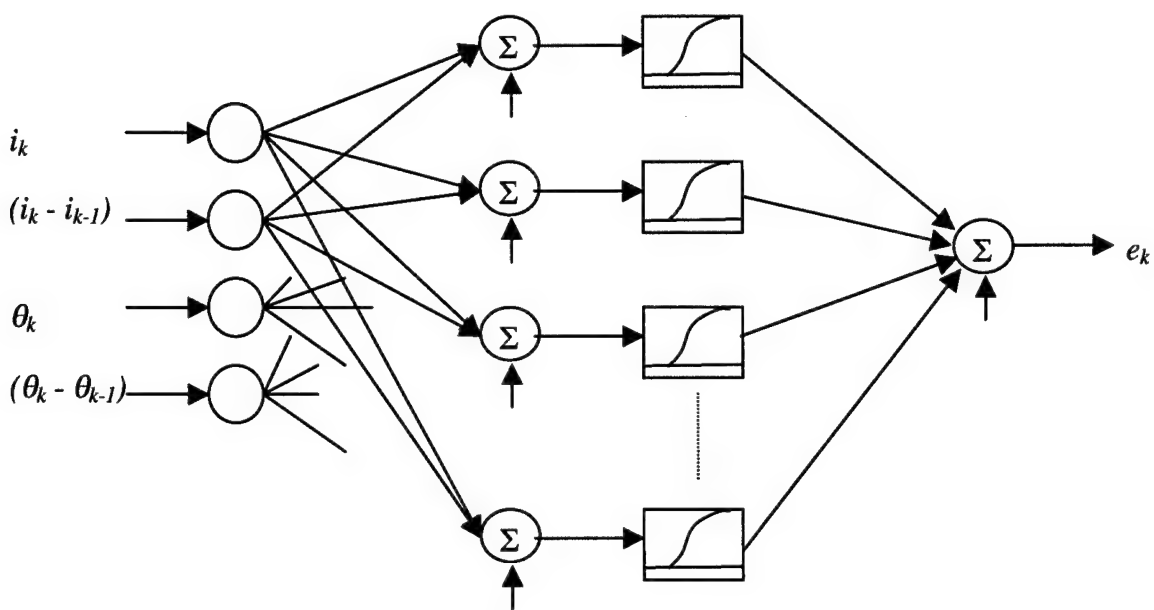


Figure 5.2. ANN topology for back emf identification (see (5.1)).

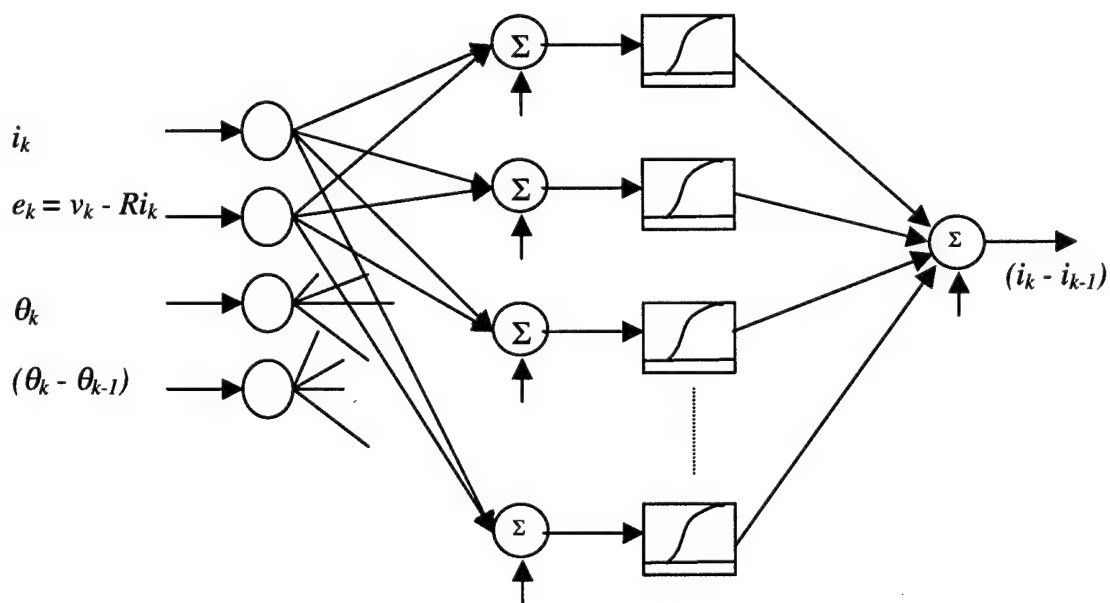


Figure 5.3 ANN topology for current change identification (see (5.2)).

The SIMULINK™ SRM model was used to produce the “on-line” measurements because a fully operational SRM drive is not available in the lab.

Fig. 5.5 shows the flow chart of the algorithm for the electromagnetic torque computation. At the start of the algorithm, the speed emf estimate  $e_{\omega k}$  is set to zero. At every time instant  $k$ , the position  $\theta_{k-1}$  and current  $i_{k-1}$  from the previous time instant are retrieved from the SIMULINK™ SRM model and used to compute the position and current changes. The position  $\theta_k$  and current  $i_k$  samples then overwrite the values stored in the previous time instant. Based on these “measured” and computed values, the ANN in Figure 5.3 is trained to identify the change in current ( $i_k - i_{k-1}$ ). The speed emf is then obtained by inverting the ANN using an iterative search technique assuming a range for  $e_{\omega k}$  as shown in the flow chart. Remember that  $e_{\omega k}$  cannot experience a large variation instantaneously, so we assume that this variation is within  $\pm 5\%$  of the DC supply  $V_{dc}$ .

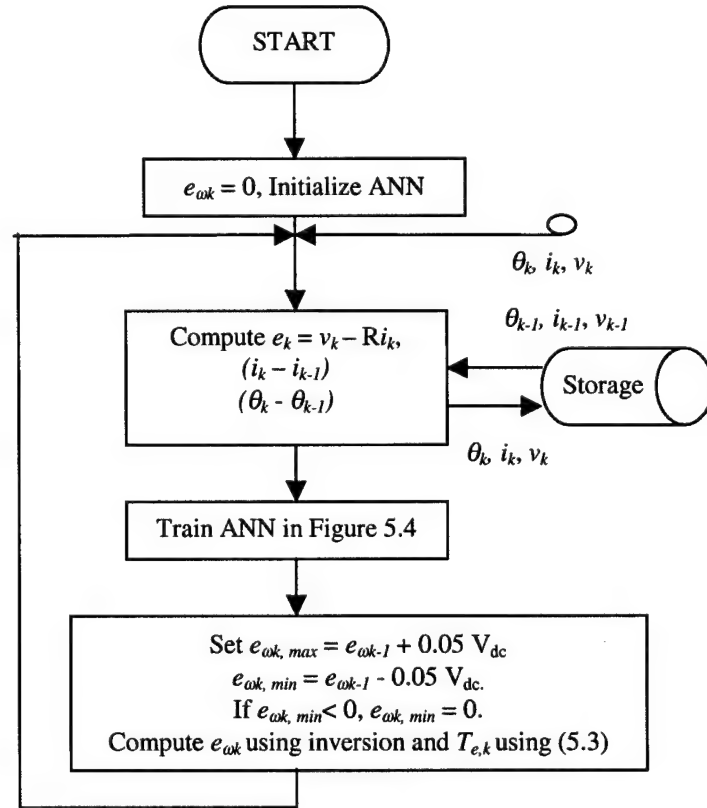


Figure 5.5. The flow chart for the electromagnetic torque computation

## 5.4 Simulation and Implementation Results

The ANN topology for the estimation task was optimized using MATLAB<sup>TM</sup>. The ANN has an input layer of 4 neurons, a hidden layer with 3 neurons using tan-sigmoid activation functions and an output layer with one neuron having a linear activation function.

The ANN estimator is initiated with random weights. The estimator trains to predict the change in current ( $i_k - i_{k-1}$ ), for given back emf  $e_k$ , current  $i_k$ , rotor position  $\theta_k$  and speed  $\omega_k$ . It was found that speed and current level changes in the SRM are essential for the ANN to be able to train correctly and assign the individual components of the back emf  $e_k$  to the appropriate causes (i.e., speed and current changes). The data corresponding to such changes can be easily obtained since speed and current changes are inherently present in a practical system during transients due to load changes and startup.

Fig. 5.6 shows the initial response of the estimation system after startup with random weights and biases. The transients during changes in speed and current levels are evident. During the simulations, the speed and currents were perturbed by step changes after fixed periods. This was done to allow the ANN to identify the characteristics of the system.

Fig. 5.7 shows the plot of the estimated electromagnetic torque along with that obtained from FEA data corresponding to the SRM current waveform at 1000 rpm and 13 A. The estimation system that has been running for 1 sec (i.e., the time offset) is able to estimate the torque to a very good accuracy. By time offset, we mean that the ANN started with no prior knowledge of the system and takes 1 sec to learn the system characteristics. Remember that an advantage of the technique proposed here is that no off-line measurements are required as in other techniques. Figure 5.8 shows the back emf and its speed component as estimated by the ANN estimator. Preliminary simulation studies for the multi-phase case indicate that the influence of the other phases maybe added by considering additional inputs to the ANN. In this study, we have not considered them.

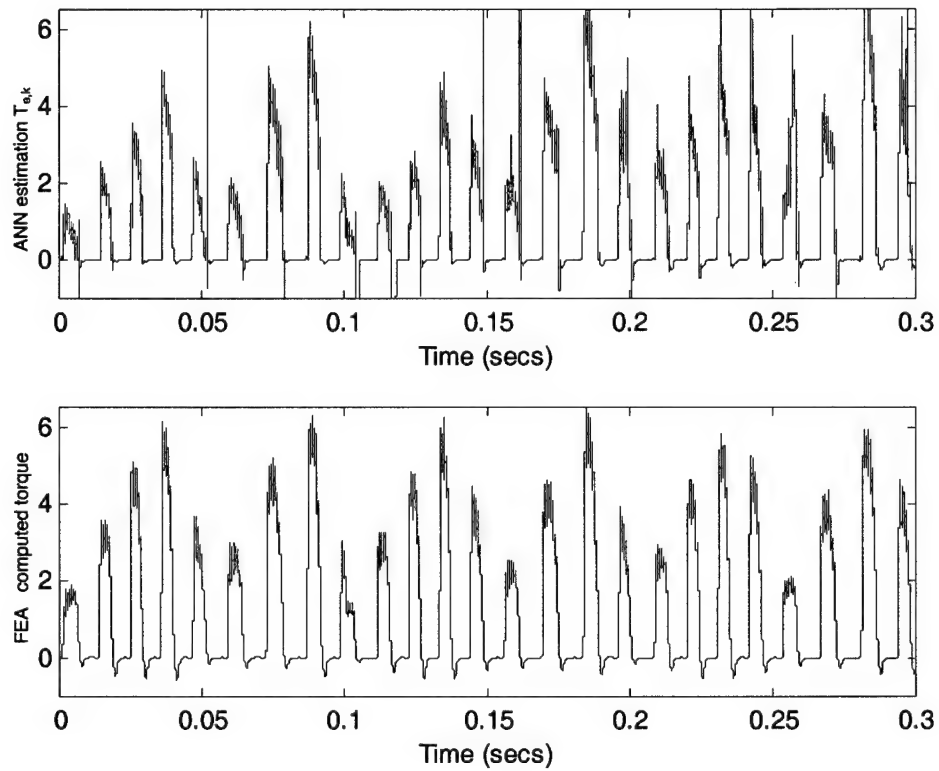


Figure 5.6. The ANN estimator response following startup with random weights and biases.

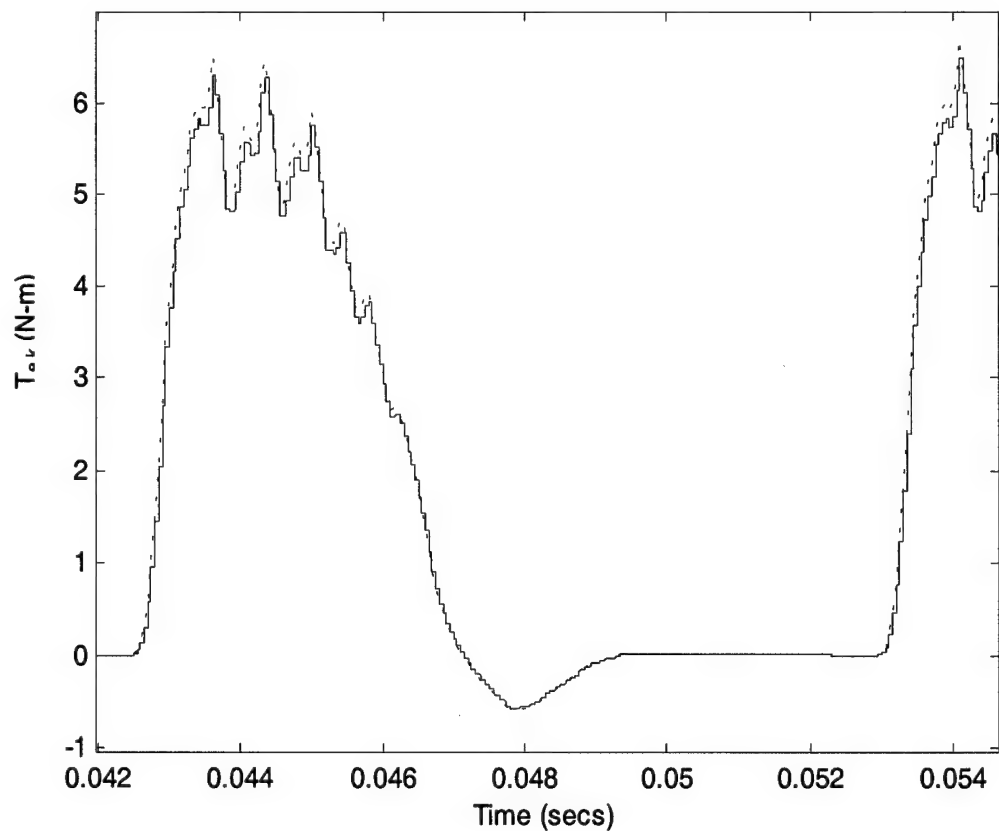


Figure 5.7. The comparison of the electromagnetic torque computed using the ANN estimator (solid) and using FEA (dashed) at 1000 rpm and 13 A. (Time offset = 1 sec).

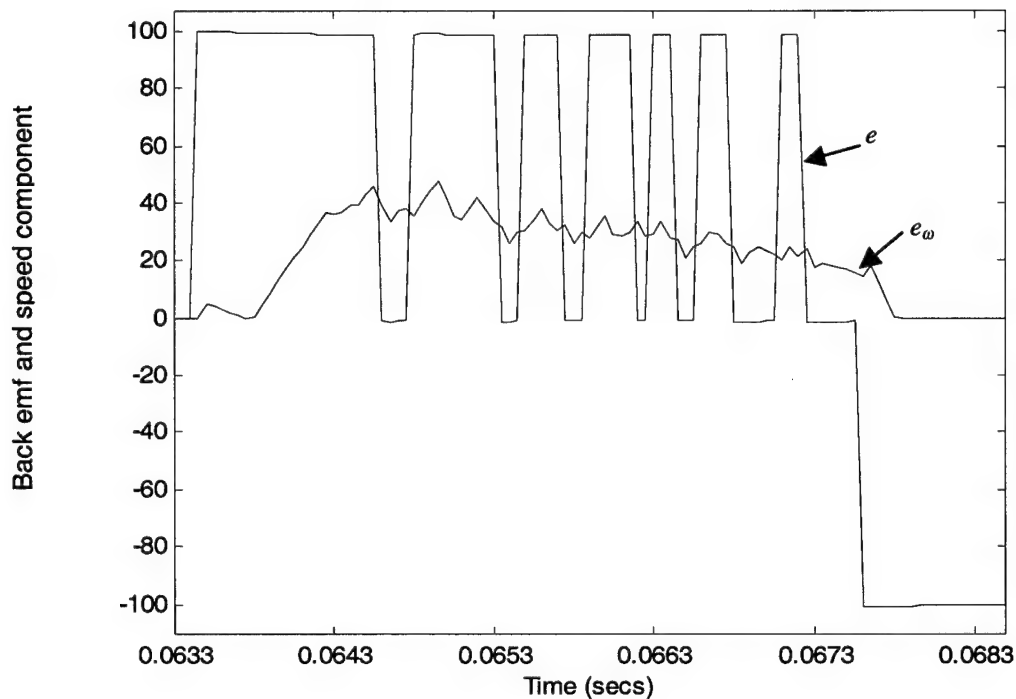


Figure 5.8. The measured back emf  $e$  and the estimated speed component  $e_w$  at 1000 rpm and 13 A (Time offset = 1 sec).

## References

- [1] M.Ehsani, B. Fahimi, G. Suresh, J. Mahdavi, "A New Approach to model Switched Reluctance Motor Drive; Application to Dynamic Performance Prediction, Control and Design", *Power Electronics Specialist Conference*, pp. 2097-2102, 1998, Fukuoka, Japan, May 17- 22.
- [2] R.B. Inderka, R.W. De Doncker, M. Krehenbrink, "On-Line Estimation of Instantaneous Torque in Switched Reluctance Motor Control", *Proceedings of the 2000 IEEE International Symposium on Industrial Electronics*, Puebla, Mexico, December 2000.
- [3] M. S.Islam, I. Husain, "Self-tuning of Sensorless Switched Reluctance Motor Drives with Online Parameter Identification", *IEEE Industry Applications Society Annual Meeting*, Rome, October 2000.
- [4] A.M. Michaelides, C.Pollock, "Modelling and design of switched reluctance motors with two phases simultaneously excited", *IEE Proceedings*, Vol. 143, No. 5, pp. 361-370, September 1996.
- [5] S. S. Ramamurthy, R.M. Schupbach, J.C. Balda, "Artificial Neural Networks based Models for the Multiply Excited Switched Reluctance Motor", *Conference Proceedings of the IEEE Applied Power Electronics Conference*, pp. 1109-1115, March 4-8 2001, Anaheim, California.
- [6] R. M. Schupbach, Switched-Reluctance Motors: Dynamic Simulation Techniques, M.S. Thesis, Department of Electrical Engineering, University of Arkansas, July 2000.
- [7] B. Fahimi, G. Suresh, M. Ehsani, "Torque Estimation in Switched Reluctance Motor Drive using Artificial Neural Networks", *Proceedings of the 1997 23rd Annual International Conference on Industrial Electronics, Control, and Instrumentation*, pp 21-26, Nov 9-14 1997, New Orleans, LA.

- [8] D. A. Hoskins, J. N. Hwang, J. Vagners, "Iterative Inversion of Neural Networks and Its Applications to Adaptive Control", *IEEE Transactions on Neural Networks*, Vol. 3, No. 2, March 1992.
- [9] L. Behera, M. Gopal, S. Chaudhury, "On Adaptive Trajectory Tracking of a Robot Manipulator Using Inversion of Its Neural Emulator", *IEEE Transactions on Neural Networks*, Vol. 7, No. 6, November 1996.

## **Chapter Six**

### **DSP IMPLEMENTATION OF ANN BASED CONTROL SOLUTIONS**

#### **6.1 Introduction**

Previous chapters have illustrated that ANN-based solutions can be applied to simplify the control tasks in SRM. The main practical problem with applying ANN till now has been that their execution speeds are limited by the capability of the available processors. However, advanced architectures such as the expressDSP™ [1-2] from Texas Instruments (TI) with multiple levels of pipelining and higher clock speeds are now available. In addition, excellent code development tools such as the Code Composer Studio (CCS) [3] support these. The chapter reports on the implementation of the ANN-based mapping solutions entirely in ANSI C using the features of CCS Version 1.2. The profiling techniques available in the CCS to aid the rapid code development are then applied to measure the execution times of the different ANN stages. The SRM input variables obtained through simulations at different operating conditions (in lieu of actual measurements being available) are then used to test the ANN operation and response. The chapter also gives an outline of the schematic for interfacing the C6701 EVM with a C240 EVM that takes care of the low-level tasks of generating the PWM signals for SRM drive control. Finally, the chapter concludes by describing the implementation of the ANN for torque mapping (see Chapter Four) as well as the obtained performance results.

#### **6.2 Description of the ANN Implementation**

From the ANN structure presented in previous chapters, one can anticipate that an important portion of the ANN computational time is due to the calculation of the weighted sums at each neuron of the hidden and output layers. The ANN were implemented on the TMS320C6701 EVM entirely in software using the C language and the features available in the CCS Ver 1.2 [3].

The first step of the code is to compute the weighted sum at each neuron of the hidden layer for the activation functions. The C language code implementing these computations has a nested loop structure. The bias at each neuron is then added to this sum to obtain the net activation input. This is then propagated through the activation function at the neuron. The code in our first implementation had the following form:

```
void comptout()
{
    int i,j;
    for (j=0;j<n1;j++) netin1[j]=bias1[j];
    for (j=0;j<n1;j++)
    {
        for (i=0;i<n0;i++) netin1[j]+=weight1[j][i]*netin0[i];
        actv1[j]=squash(netin1[j]);
    }
    netin2[0]=bias2[0];
    for (i=0;i<n1;i++) netin2[0]+=weight2[0][i]*actv1[i];
    netout=netin2[0];
}
```

where float squash(float) computes the log-sigmoid function using the functions from the math library.

Another time-consuming activity is the computation of the activation function using the following log-sigmoid expression:

$$f(x) = \frac{1}{1 + e^{-x}} \quad (6.1)$$

One can use the function “exp()” or “expf()” to implement this equation in the C program. The CCS profiler was used to measure the number of cycles required by each function and the precision of the value returned (by the exp() and expf() functions). Based on this, it was determined that the expf() function requires much lesser number of cycles (390) than the exp() function (1030) and also offers adequate precision for the application. The log-sigmoid function value, thus computed, has a value of 0 for less or equal than -15 and a value of 1.0 for greater or equal than 15. As a result, it is necessary to compute this function only in the range  $[-15 < x < 15]$ .

With the log-sigmoid computation using the expf() function, the forward propagation (computing the torque output) takes about 3900 cycles in the worst case when  $[-15 < x < 15]$ .

This is because the usage of the  $\expf()$  function leads to the disadvantage that the code contains function calls that cannot be software pipelined.

To be able to use pipelined code, we use the “lookup-table” technique for determining the log-sigmoid function values for inputs between the range  $-15$  to  $15$ ; these computed values were stored in a lookup table. For a given input value for which the function value is required, the index into the table is calculated using:

$$m = \text{round} \left\{ (x + 15) \times \frac{\text{sigPoints}}{30} \right\} \quad (6.2)$$

where *sigPoints* is the number of points in the lookup table for the log-sigmoid function. This equation was implemented in the C program using type-casting to integer value. However, it was found that direct implementation of this equation in the C program leads to the requirement of a large number of cycles (about 2800 cycles in the worst case with  $[-15 < x < 15]$ ) because the division process which is used in the index computation is very time consuming. This was overcome by replacing the fraction *sigPoints/30* by its value (say *q*) in the program; that is

$$m = \text{round} \{ (x + 15) \times q \} \quad (6.3)$$

The initial code using this formulation required about 540 cycles for the forward propagation because the code uses simple addition and multiplication that are the “least computationally expensive” for the processing. Also, the compiler was able to setup better pipelining since the number of registers required during each iteration was small. The loop structure and the arrangement of the code was further improved using the CCS Ver 1.2 features [8-11] and the final code obtained required only 217 cycles for the torque computation by forward propagation. These 217 cycles at a clock of 133 MHz mean that the C6701 requires only

$$\frac{217}{133 \times 10^6} = 1.63 \mu \text{ sec for the torque computation by forward propagation.}$$

The following features of the CCS were used for improving the code arrangement and pipelining [3]:

- The profiler was used to determine the number of cycles taken by each section of the code and thus identify the “expensive” sections.
- The `#pragma MUST_ITERATE` directive was used to pass the information about the trip count (number of loop iterations) to the compiler.
- The `#pragma UNROLL` directive was used to unroll small loops and increase the number of instructions available for execution in the pipeline.
- The `-pm` and `-mt` compiler options were respectively used to direct the compiler to use the trip count data for pipelining, and to indicate the absence of memory aliasing [4].
- The `-k` option preserved the `.asm` file for inspection. The compiler includes feedback about the pipelining in this file and also indicates better options that the user might choose. The code was rearranged till smaller iteration intervals and a larger number of parallel iterations were obtained.

The final code for the forward propagation has the following form:

```
void comptout()
{
    int j;
    int m;
    #pragma MUST_ITERATE(n1);
    for (j=0;j<n1;j++)
    {
        netin1[j]=bias1[j];
        netin1[j]+=weight1[j][0]*netin0[0]+weight1[j][1]
        netin0[1]+weight1[j][2]*netin0[2];
    }
    #pragma MUST_ITERATE(n1);
    for (j=0;j<n1;j++)
    {
        if ((netin1[j]>-15)&&(netin1[j]<15))
        {
            m=(int)((netin1[j]+15.)*80);
            actv1[j]=sigTable[m];
        }
        if (netin1[j]<-15) {actv1[j]=0.0;}
        if (netin1[j]>15) {actv1[j]=1.0;}
    }
    netin2[0]=bias2[0];
    #pragma UNROLL(n1);
    for (j=0;j<n1;j++) netin2[0]+=weight2[0][j]*actv1[j];
}
```

```

    netout=netin2[0];
}

```

where sigTable[] contains the value for the log-sigmoid function in the range -15 to 15 and has 2400 points.

The process of learning by error back-propagation involves the computation of activations at the neurons. The back-propagation algorithm was also implemented in C and the code was then optimized. The resulting code executed in 344 cycles or 2.58  $\mu$ s per iteration.

For applications involving electric drives, torque feedback at a sampling rate of about 25 kHz maybe considered to be adequate under most conditions. Since the C6701 is able to compute the torque output under multi-phase operation at a much higher speed, there is sufficient time available between the samples to schedule training of an adaptive ANN-based model (which changes with the actual motor parameters) based on on-line measurements (see Chapter Five). This can be used to schedule calculations to compute the new actual values of torque. Finally, the error between the ANN torque output and the new calculated value can be used to schedule training of the torque ANN. Thus, the C6701 can be used to implement several ANN that cannot only estimate the drive output, but also adapt to changing drive parameters.

### 6.3 Testing of the ANN using Probe Points

The CCS has the facility to connect data from files on the PC to the program running on the target DSP. This is done using probe points [3]. The SRM current and rotor position data were obtained from SIMULINK<sup>TM</sup> simulations [5] and the data corresponding to two different speeds, 100 rpm and 6000 rpm, were stored in ASCII text files in floating-point format. In a real implementation, real measurements would take the place of these ASCII files. Probe points were then used to couple these data files at runtime to the C6701. This was used to test the ANN output.

Portions of the resulting graphs for the two winding currents, the rotor position and the output torque are included as Figures 6.1 and 6.2, which are screen snapshots taken during the simulations.

With sigPoints equal to 2400, it was found that the resulting torque waveform includes additional high-frequency noise introduced by the ANN due to rounding of the index value. Increasing sigPoints to 6000 mitigated this noise.

#### **6.4 Interfacing the C6701 EVM to the C240 EVM**

The intended role of the C6701 in the SRM drive system is to provide computational support to the drive controller. The main reason is that present-day DSPs for motion control do not have the required bandwidth to implement novel control algorithms (e.g., model reference adaptive control) when the electric motor is running at high speeds (e.g., greater than 6000 rpm). In our implementation, the SRM will be controlled, at the low-level, through PWM signals generated using the C240 EVM. An interface between the two DSPs has to be designed to transfer the computed torque value to the C240 EVM as feedback. The interface between the C6701 and the C240 EVM can be implemented conveniently through the C6701 Host Port Interface (HPI) [6]. The HPI is a 16-bit-wide parallel port through which the C6701 memory space is visible to the host processor (the C240, in this case). The C240 functions as the master to the interface. The data exchange can take place using internal or external memory. The C240 can also access the memory-mapped peripherals. Connectivity to the C6701's memory space is provided through the DMA controller in the CPU.

The  $\overline{HRDY}$  pin can be used to insert a delay during a transfer and characterize the data transfer speed through the HPI. Since the C240 has a separate address bus, the  $\overline{HAS}$  can be inactive high at all times.

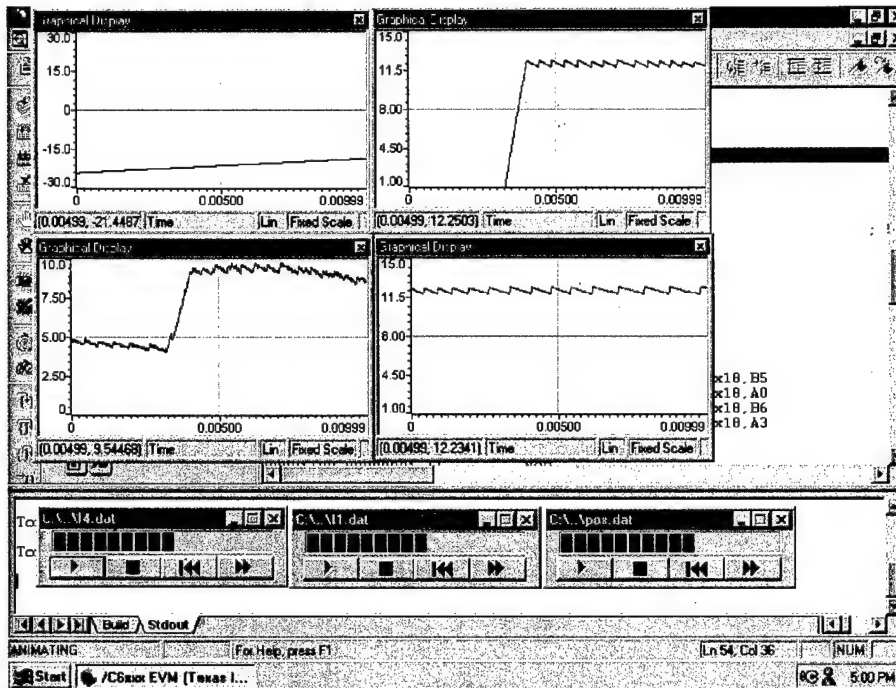


Figure 6.1. Test results of the ANN processing using probe points in CCS Ver 1.2 at 100 rpm. The graphs indicate (CCW from the top left corner) the rotor position (with respect to the working phase), the ANN torque output, the current in the leading phase, and the current in the working phase.

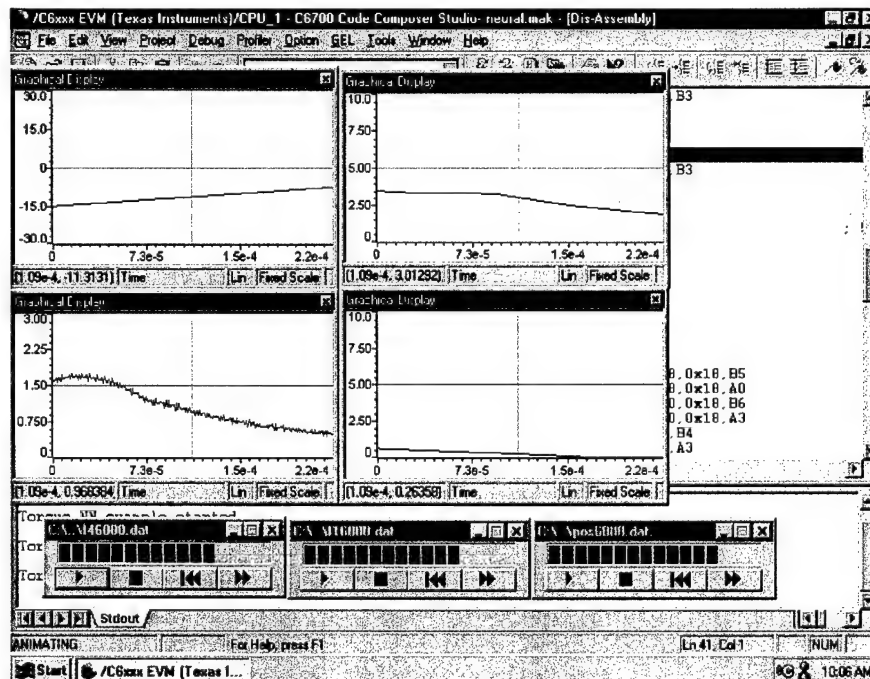


Figure 6.2. Test results of the ANN processing using probe points in CCS Ver 1.2 at 6000 rpm. The graphs indicate (CCW from the top left corner) the rotor position (with respect to the working phase), the ANN torque output, the current in the leading phase, and the current in the working phase.

HCNTL [1:0] values would be set by decoding the address of the C240. The base address is determined by the decoding logic and is chosen such that HCNTL1 = 0, HCNTL0 = 0 and HHWIL = 0.

On the C240 EVM, the RAMOE on the GAL device controls the read from external memory operation. On the other hand, RAMWE controls the write to memory operation [7]. These signals are used as separate strobes for the  $\overline{HDS\ 1}$  and  $\overline{HDS\ 2}$  for read and write. The C240  $R/\overline{W}$  signal is connected to the HPI  $HR/\overline{W}$  signal input. HWOB=1 indicates that the first write is the least significant half word. The connection diagram for the interface between the C6701 and

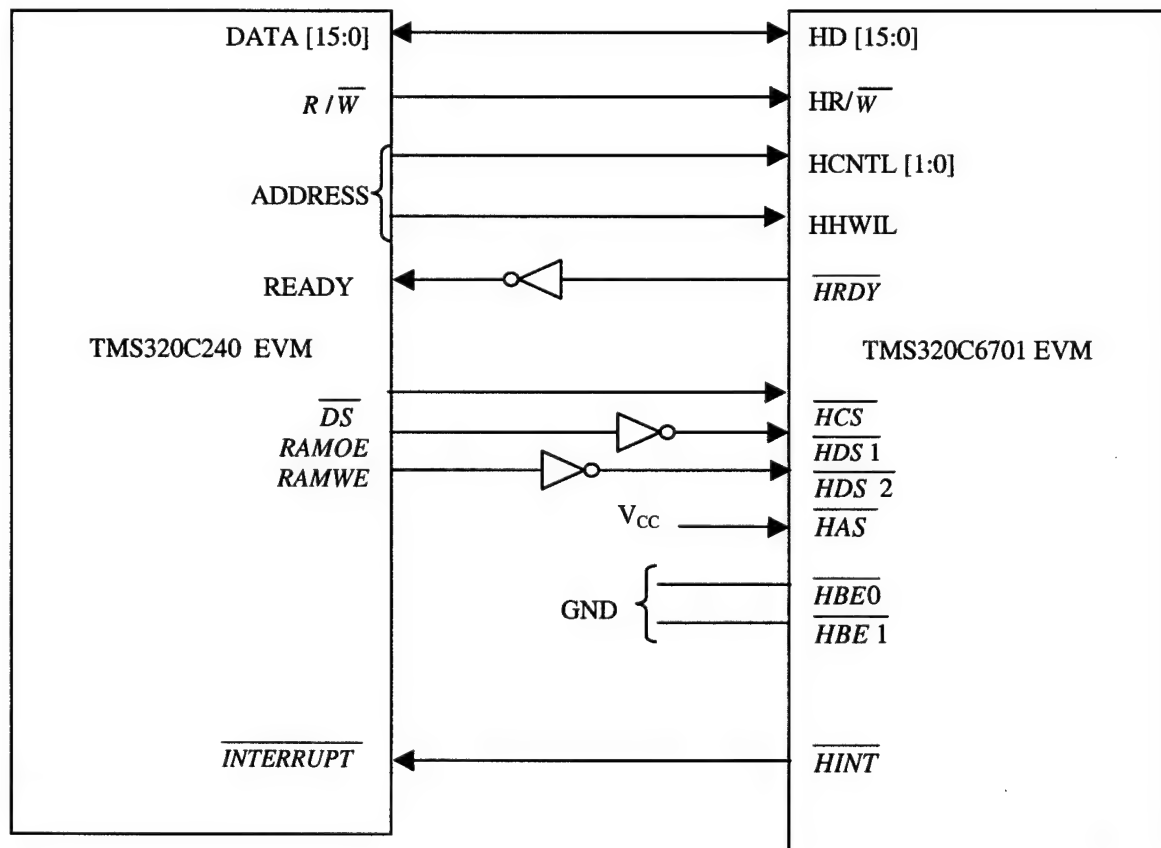


Figure 6.3 Interface between the C6701 and C240 through the HPI.

the C240 EVM is shown in Figure 6.3.

$\overline{HBE} [1:0] = 0$  since only a half word (16 bits) is written by the C240 during a write operation. The HPI Control register (HPIC) is normally the first register accessed to set the configuration bits and initialize the interface [6]. The DSPINT bit can be used by the C240 to interrupt the C6701. The FETCH bit of the HPIC is used with the  $\overline{HRDY}$  during a read or write to set up a software handshake.

The base address of the C6701 HPI is chosen during design. The addresses of the control, address and data registers of the HPI are relative displacements to this address and are thus accessible by programs written on the host C240. For example, if:

“hpiBaseAddr” denotes the base address of the C6701 HPI chosen to access the control register first half word.

Then: “hpiBaseAddr+1” accesses the second half word of the control register HPIC to change the control settings and initialize the interface.

“hpiBaseAddr+2” accesses the first half word of the address register HPIA to write the address of the C6701 address map to which access is required.

“hpiBaseAddr+3” accesses the second half word of the address register HPIA to write the address of the C6701 address map to which access is required.

“hpiBaseAddr+4” accesses the first half word of the data corresponding to the address placed in the address register through HPID.

“hpiBaseAddr+5” accesses the second half word of the data corresponding to the address placed in the address register through HPID.

## 6.5 Preliminary Implementation of the Adaptive Estimation ANN and DSP/BIOS

A first implementation of the Adaptive Torque Estimation ANN indicates that each training by back propagation would require less than 2  $\mu\text{sec}$  and each iterative search by inversion would require less than 5  $\mu\text{sec}$ .

Since the ANN for static torque mapping requires about 1.63  $\mu\text{sec}$  for forward propagation and 2.4  $\mu\text{sec}$  for training by back propagation, when the complete system is in a training mode, the estimation and computation tasks would require less than 12  $\mu\text{sec}$ . The simulations have assumed a sampling time of 50  $\mu\text{sec}$  (sampling frequency of 20 kHz).

A DSP/BIOS implementation was also done to test the execution of the torque ANN thread by simulating on the DSP conditions similar to that under which the torque ANN would execute in the final implementation (a thread is a schedulable unit of execution in a multitasking system). The results are displayed in Figure 6.4. A hardware interrupt (HWI) driven by the timer clock at intervals of 25  $\mu\text{sec}$  initiates a dummy data transfer function.

This then triggers a software interrupt that executes the torque ANN (ANN\_SWI). A load loop of 1000 instructions is also executed with the torque ANN to allow adequate margin for additional operations. After the execution of ANN\_SWI, KNL\_swi is initiated to invoke the task scheduler for executing other threads (see Figure 6.4).

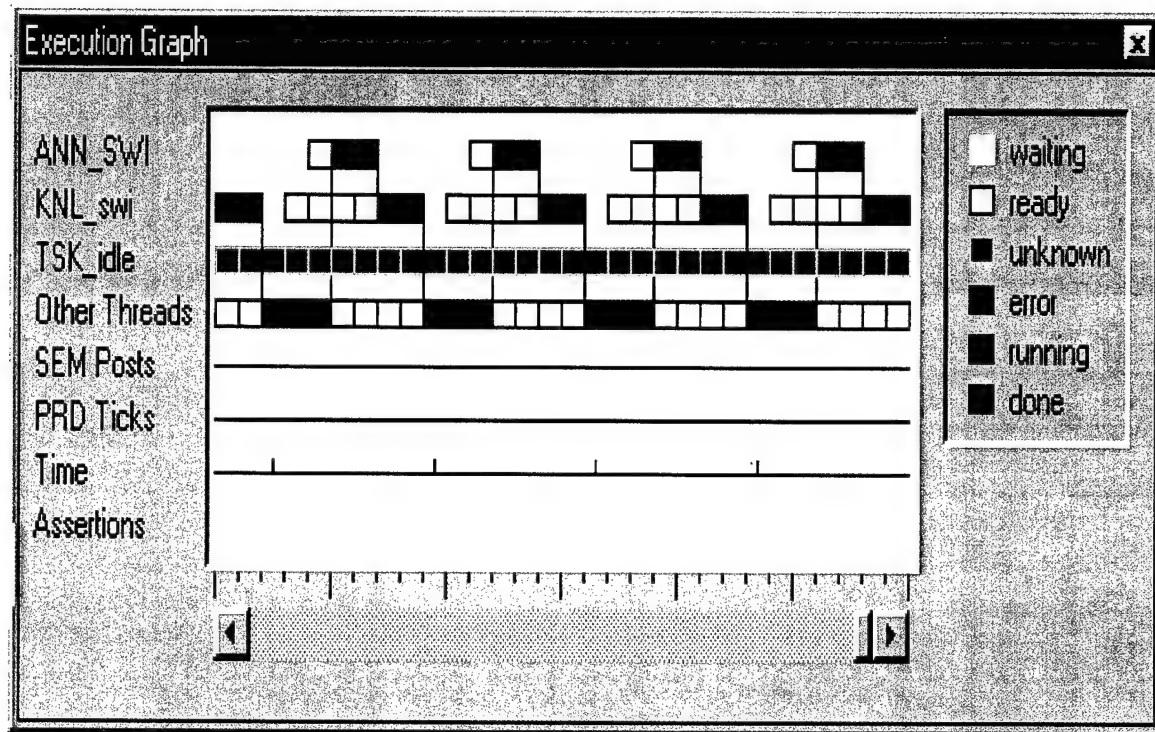


Figure 6.4. The task scheduling in the DSP/BIOS implementation; the interval between tics on the time axis is 25  $\mu$ sec.

## References

- [1] TI literature number SPRU269D: TMS320C6201/6701 Evaluation Module User's Guide, December 1998.
- [2] TI literature number SPRU189F: TMS320C6000 CPU and Instruction Set Reference Guide, September 2000.
- [3] TI literature number SPRU301C: TMS320C6000 Code Composer Studio Tutorial, February 2000.
- [4] TI literature number SPRU198C: TMS32062x/TMS32067x Programmer's Guide, May 1999.
- [5] R.M.Schupbach, Switched-Reluctance Motors: Dynamic Simulation Techniques, M.S. Thesis, Department of Electrical Engineering, University of Arkansas, July 2000.
- [6] TI literature number SPRU190C: TMS320C6000 Peripherals, April 1999.
- [7] TI literature number SPRU248A: TMS320C24x DSP Controllers Evaluation Module, August 1997.

## Chapter Seven

### CONCLUSIONS

This Part 1 of the Final Report has provided the following contributions to the fields of Switched Reluctance Motors and electric vehicle propulsion:

- Presented an approach for determining the SRM power ratings for a complete specification in an electric propulsion application. A comparison of the thermal duty of the SRM with other electric motors was also presented. The PMSM has considerably higher thermal duty as compared to the other motors. The results show that the thermal duty of the SRM can be reduced considerably by appropriate choice in the design process of the contribution by the individual loss components to the total machine losses. The SRM is comparable to the traditional motors under these conditions. Future work is the need to develop a procedure to design a SRM so that the losses are limited to the desired proportion of the total and the thermal duty is kept low.
- Developed an approach for designing SRM under multi-phase excitation mode while taking the practical loading constraints. The studies leading to the development of this approach also provided insight into the relative merits and de-merits of each of the suggested and popular SRM configurations so as to further aid in the choice of an appropriate configuration. The design results show that an improvement in torque density is obtained in those configurations that increase the number of pole pairs participating in the torque production. To this end, the full- and fractional-pitch windings do not change the number of pole pairs participating in torque production. Also, it is not possible to improve the torque density substantially by using full- and fractional-pitch windings due to the thermal constraints imposed by the maximum flux density. The apparent advantage of a better utilization of the winding area in the full- and fractional-pitch SRM is reduced by the higher value of  $K_A$  for these configurations. The short-pitch SRM use unipolar converters and the voltage applied across the windings is twice of that for the full- and fractional-pitch SRM which may use bipolar converters and start-connected windings. The peak current for the converter switches thus

remains unchanged. The choice of a particular SRM configuration should be also based on other factors such as high-speed operation, use of readily available standard inverters, ease of manufacturing, requirement of low torque ripple using current profiling between phases, noise-reduction needs and system losses. In case of SRM having odd number of phases, continuous operation in the short-flux-path mode can be sustained by simple re-connection of phase leads to get the appropriate current directions. Thus in the case of the 10/8 five-phase SRM, simple uni-polar converters can be employed while still getting all the benefits of the short-flux-path mode such as lower acoustic noise, vibrations and core losses. All other suggested solutions for obtaining this mode of operation in the 10/8 SRM require bipolar converters. Even the shared bridge configuration suggested in reference [1] of Chapter Three will not lead to continuous short-flux-path-mode operation.

- Developed a simple FF ANN model for the multiply excited SRM that can be applied in simulations as well as for real-time implementations. The proposed techniques require small measured data sets and simple ANN topologies. The feasibility of implementing these techniques was demonstrated through implementation on the TI TMS320C6701 eXpressDSP™. The implementation shows that these techniques can be applied for the real-time estimation tasks, while leaving adequate room for other on-line adaptive ANN based solutions.
- A simple method that can be applied for direct on-line estimation of the electromagnetic torque developed in the SRM was also proposed. The technique can be scheduled in a training mode during commissioning of the drive or occasionally during the drive life-time to identify the current electromagnetic torque characteristics of the SRM and train another ANN that would then provide torque feedback. The technique is simple and feasible to implement and can be easily extended to account for interactions in the multiply excited case. This method does not work well at high speeds (greater than rated speed of the SRM drive) due to reduction in the value of  $(i_k - i_{k-1})$ . However, this method can be applied for estimating the low speed or static torque characteristics of the SRM.

- It may be possible to fit the measured data using non-linear ARMA models characterizing the SRM non-linear characteristics. However, this approach was not adopted since it was expected that it might be more computational expensive to do the model fitting in order to allow on-line adaptation as compared to the proposed ANN solutions. Future work may investigate the feasibility of this approach.
- The current models for torque mapping and on-line estimation (including those of this report) do not consider the influence of losses (due to eddy currents at high speeds) on the electromagnetic torque output and flux at a given phase current and rotor position. It is essential to subtract the loss component of current from the net phase current to get the component contributing to electromagnetic torque production. This requires further work to introduce models for the loss component of the current in order to perform this correction.
- The studies of the report indicated the feasibility of implementing several ANNs to aid in tackling different aspects of the SRM control problem. A scheme for interfacing the C6701 EVM and the C240 EVM was also presented.
- At the present time, the cost of the C6701 may make it unfeasible for low-power low-cost drives. However, the control benefits obtained by applying ANN aids makes it attractive for the higher-power drives. The feasibility of incorporating high speeds ANNs as control aids when they are implemented on the C6xxx architecture may also indicate the direction for possible enhancements in the architecture of DSPs such as the C240, that are specialized for motion control. It might be useful to incorporate some of the features of express-DSPs such as the C6xxx on the motion control DSPs to allow the implementation of more advanced and adaptive control techniques based on ANNs. The report has shown the adequacy of present day processors to implement the complete ANN based system. Further work is required to implement and apply this ANN based system and test the suggested communication scheme between the two DSPs .

## Appendix A

### DERIVATIONS OF SIZING EQUATIONS

#### A.1 Estimation of Power Losses in a SRM

The SRM is controlled by applying a current pulse to a phase winding whose inductance variation as a function of rotor position is positive. Assuming an ideal rectangular current pulse, Figure A.1 shows the current waveform, the ideal inductance variation of the torque producing phase and the stator-pole flux waveform for two different current levels. The flux waveforms in other regions of the magnetic circuit are related to the flux waveform in the stator pole [1]. The current pulse either occupies the full feasible region for torque production (i.e., from rotor angle  $\theta_1$  to rotor angle  $\theta_2$ ) or the dwell angle is changed so that it occupies a smaller region. This is illustrated by the current pulse  $I'$  from rotor angle  $\theta_1$  to rotor angle  $\theta_{off}$  in Figure A.1. For the same average torque, the amplitude  $I'$  has to be greater than that of  $I$ ; the two currents are related by  $I'^2 (\theta_{off} - \theta_1) = I^2 (\theta_2 - \theta_1)$ .

One can get an idea of the meaning of the difference  $(\theta_2 - \theta_1)$  by noting that it is equal to  $30^\circ$  for the three-phase 6/4 SRM. So the number of phase current pulses per revolutions (i.e., in this case, 4) multiplied by the number of phases (i.e., 3) and  $[\theta_2 - \theta_1]$  (i.e.,  $30^\circ$ ) is equal to  $360^\circ$ ; the angle corresponding to one full revolution of the rotor.

The relationships relating the variations of the power losses as function of output power and motor speed are necessary in order to determine the continuous power rating of the SRM in Chapter Two. Unfortunately, it is not possible to determine the exact variations unless the SRM is already designed and built; therefore, an estimation of these loss variations will be used instead. The following assumptions are made in estimating these variations of power losses with the SRM output power and speed:

- 1) Effects of magnetic saturation are neglected.
- 2) The formulation relating the power output  $P_{di}$  and speed to the losses is only valid as long as the current pulse is restricted to the region  $(\theta_2 - \theta_1)$  or, in general, to the torque producing zone

(see Figure A.1). In an actual case, the decaying trailing edge of the current pulse will be present in the region immediately after  $(\theta_2 - \theta_1)$ ; this decaying-current pulse is neglected.

- 3) It is assumed that the current pulse applied to the winding always has a rectangular-wave shape. This is only true at low-speed operation of the SRM. For high-speed operation, the applied current pulse is "peaky".

Such a waveform will not lead to any additional error in the estimation of copper losses

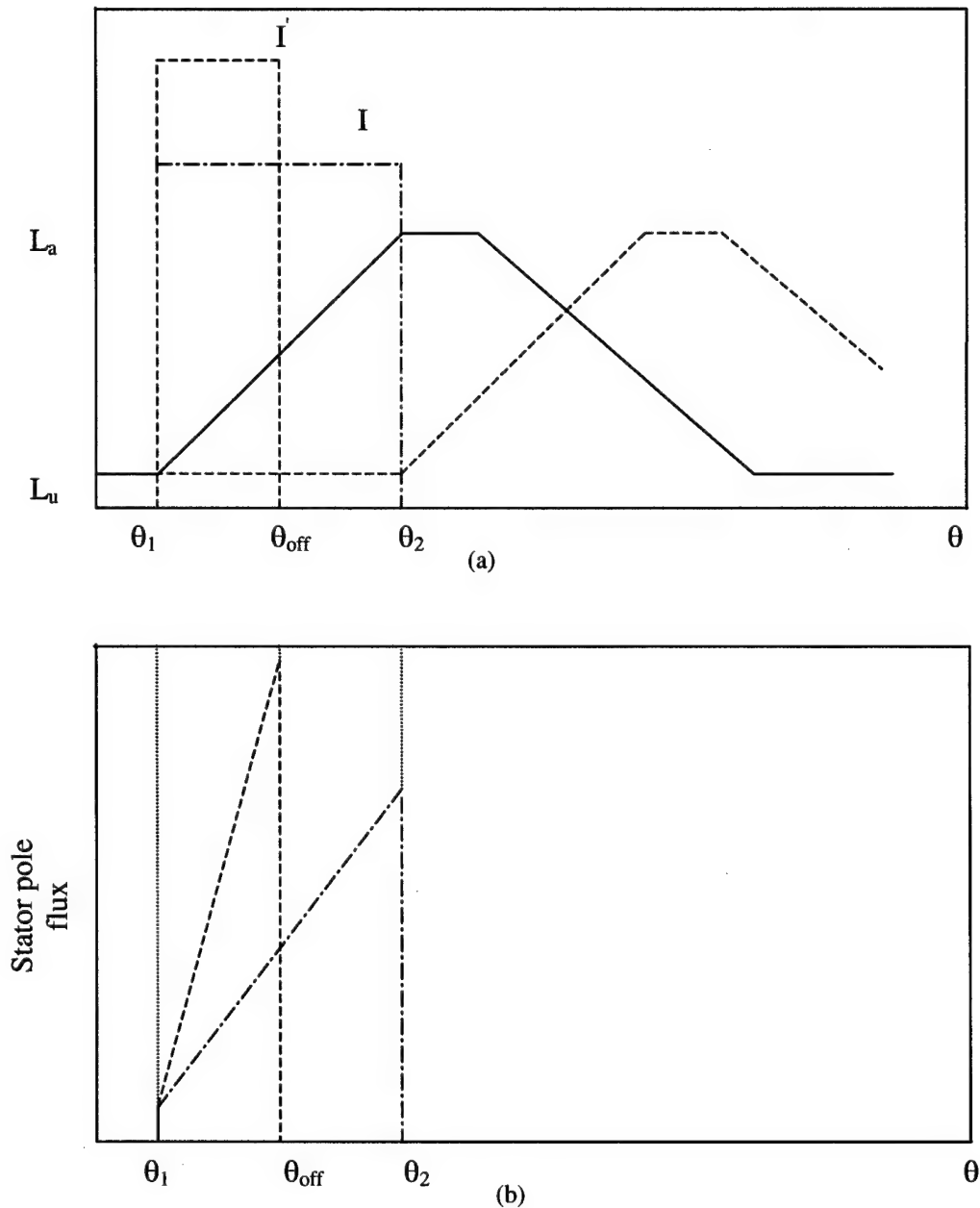


Figure A.1 (a) The ideal phase inductance and current. (b) The stator-pole flux waveform. The effect of reducing dwell-angle on the current and the stator-pole flux is illustrated in (b).

as long as its rms value is identical to that of the rectangular-wave shape case. The equations for eddy-current loss and hysteresis loss are only valid as long as the current waveform is flat-topped (i.e., constant amplitude). The error in the estimated losses will not be high as long as the periods when  $(di/dt)$  is large are small [2].

- 4) The equation for the copper loss is not valid for zero motor speed.
- 5) As per the Steinmetz equation, the hysteresis loss is determined by  $W_h \propto B_{\max}^n \omega$ , where Steinmetz found that “n” has a value of 1.6 for a wide variety of materials [3]. For the new ferromagnetic alloys, “n” may vary from 1.5 to 2.5. In fact, “n” is not a constant except for a limited range. By taking “n” constant, we are assuming that the shape of the hysteresis curve remains unchanged. This assumption is necessary to be able to simplify the formulation for the hysteresis loss in the absence of knowledge for  $B_m$ . Therefore, we decided to use the hysteresis-loss equation  $W_h \propto B_{\max}^{1.6} \omega$ . It should be noted that this Steinmetz equation based approach has been applied only to the case of the hysteresis loss as a function of the peak flux-density under each condition. Since the complete Steinmetz equation that also accounts for eddy-current losses [1] is applicable only to the case of sinusoidal excitation, we have developed an alternate approach for the eddy-current loss based on the basic laws governing eddy-current loss.

From the driving schedules and the EV main specifications, we know the required output power and speed of the motor drive at various time instants. In order to calculate the equivalent continuous power rating  $P_{cont,i}$  of the SRM, we will relate the losses in the SRM at known output power and speed (i.e., only one operating point) to the required output powers and speeds at various time instants in the considered driving schedule (i.e.,  $P_a$  and  $\omega$ ). The following analysis illustrates this procedure.

#### A.1.1 Variation of the copper loss

Consider a SRM producing torque  $T_1$  at speed  $\omega_1$  and torque  $T_2$  at speed  $\omega_2$ . Since the SRM torque varies as a function of the square of the current under the assumption of magnetic linearity, the copper loss is then directly proportional to the output torque. Thus, the copper loss at these two points are related by :

$$\frac{W_{cu1}}{W_{cu2}} = \frac{T_1}{T_2}.$$

Since  $T = \frac{P}{\omega}$ , the copper losses at two different output powers and speeds are related as :

$$\frac{W_{cu1}}{W_{cu2}} = \frac{P_1 \omega_2}{P_2 \omega_1} \quad (A.1)$$

Now, consider that the torque required at a particular speed is produced by applying a current pulse throughout the angle range  $(\theta_2 - \theta_1)$  and the same torque is produced by applying a current pulse throughout the smaller angle range  $(\theta_{off} - \theta_1)$  as illustrated in Figure A.1. The copper loss is then given by:

- Current pulse throughout the angle range  $(\theta_2 - \theta_1)$  with amplitude  $I$ :  $W_{cu1} \propto I^2$ .
- Current pulse with reduced dwell angle  $(\theta_{off} - \theta_1)$  and amplitude  $I$ :  $W_{cu2} \propto I^2 \frac{(\theta_{off} - \theta_1)}{(\theta_2 - \theta_1)} \propto I^2$ .

Thus, the length of the dwell angle does not affect the copper loss for a given torque value.

#### A.1.2 Variation of the eddy-current loss

The flux in the stator pole is proportional to the phase flux linkages that may be expressed as

$$\lambda \propto L_u I + K(\theta - \theta_1)I$$

where  $K = \frac{L_a - L_u}{\theta_2 - \theta_1}$  with  $L_a$  being the aligned inductance and  $L_u$  the unaligned inductance.

Also, the flux density  $B$  is proportional to the flux per turn and also to the flux linkage  $\lambda$ . Then, the rate of change of the flux density can be written as follows:

$$\frac{dB}{dt} \propto \frac{d\lambda}{dt} \propto \frac{d(L_u I + K I (\theta - \theta_1))}{dt}$$

$$\therefore \frac{dB}{dt} \propto KI \omega$$

The eddy-current losses can be approximated by:

$$W_e \propto \left( \frac{dB}{dt} \right)^2$$

$$\therefore W_e \propto K^2 I^2 \omega^2$$

Now, assume that a SRM develops torque  $T_1$  at speed  $\omega_1$  and torque  $T_2$  at speed  $\omega_2$ , then we can write:

$$\frac{W_{e1}}{W_{e2}} = \frac{P_1}{P_2} \frac{\omega_2}{\omega_1} \left( \frac{\omega_1}{\omega_2} \right)^2 = \frac{P_1}{P_2} \frac{\omega_1}{\omega_2} \quad (\text{A.2})$$

It can be shown that the eddy-current loss  $W_e$  remains unchanged if the same torque at a particular speed is produced by either applying a current pulse throughout the angle range  $(\theta_2 - \theta_1)$  or by using a reduced dwell-angle since  $W_e \propto K^2 I^2 \omega^2$ .

### A.1.3 Variation of the hysteresis loss

The hysteresis loss is given by  $W_h \propto B_{\max}^{1.6} \omega$ .

Since  $B_{\max} \propto \phi_{\max} \propto \lambda_{\max} = (L_a + L_u)I$ ,

$$\begin{aligned} \frac{W_{h1}}{W_{h2}} &= \left( \frac{I_1}{I_2} \right)^{1.6} \frac{\omega_1}{\omega_2} = \left( \sqrt{\frac{\omega_2 P_1}{\omega_1 P_2}} \right)^{1.6} \frac{\omega_1}{\omega_2} \\ \frac{W_{h1}}{W_{h2}} &= \left( \frac{P_1}{P_2} \right)^{0.8} \left( \frac{\omega_1}{\omega_2} \right)^{0.2} \end{aligned} \quad (\text{A.3})$$

If the same torque at a particular speed is developed by reducing the dwell angle, then:

$$B_{\max}' \propto L_u I' + K(\theta_{\text{off}} - \theta_1) I'$$

then,

$$\frac{W_h'}{W_h} = \frac{B_{\max}'}{B_{\max}} \propto \frac{\theta_{\text{off}} - \theta_1}{\theta_2 - \theta_1} \frac{I'}{I}$$

$$\frac{W_h'}{W_h} \propto \sqrt{\frac{\theta_{\text{off}} - \theta_1}{\theta_2 - \theta_1}}$$

Above rated speed, the dwell-angle is changed such that

$$\frac{\theta_{\text{off}} - \theta_1}{\theta_2 - \theta_1} = \frac{\omega_{\text{rated}}}{\omega}$$

Hence,

$$\frac{W_h}{W_h} \propto \sqrt{\frac{\omega_{rated}}{\omega}}$$

Based on the above formulations, the efficiency contours have been determined and plotted in Figure A.2 for a SRM having an efficiency of 85% at peak output power and rated speed,  $f = 0.333$  and  $c = 0.4$ . These contours are similar in shape to those given in [4].

## A.2 Derivation of the Coefficients $K_1, K_{2e}, K_{2h}$

Let us assume that we know the copper loss  $W_{cup}$ , the hysteresis loss  $W_{hp}$  and the eddy-current loss  $W_{ep}$  of the motor at the peak output power  $P_{emp}$  and rated speed  $\omega_{emr}$ .

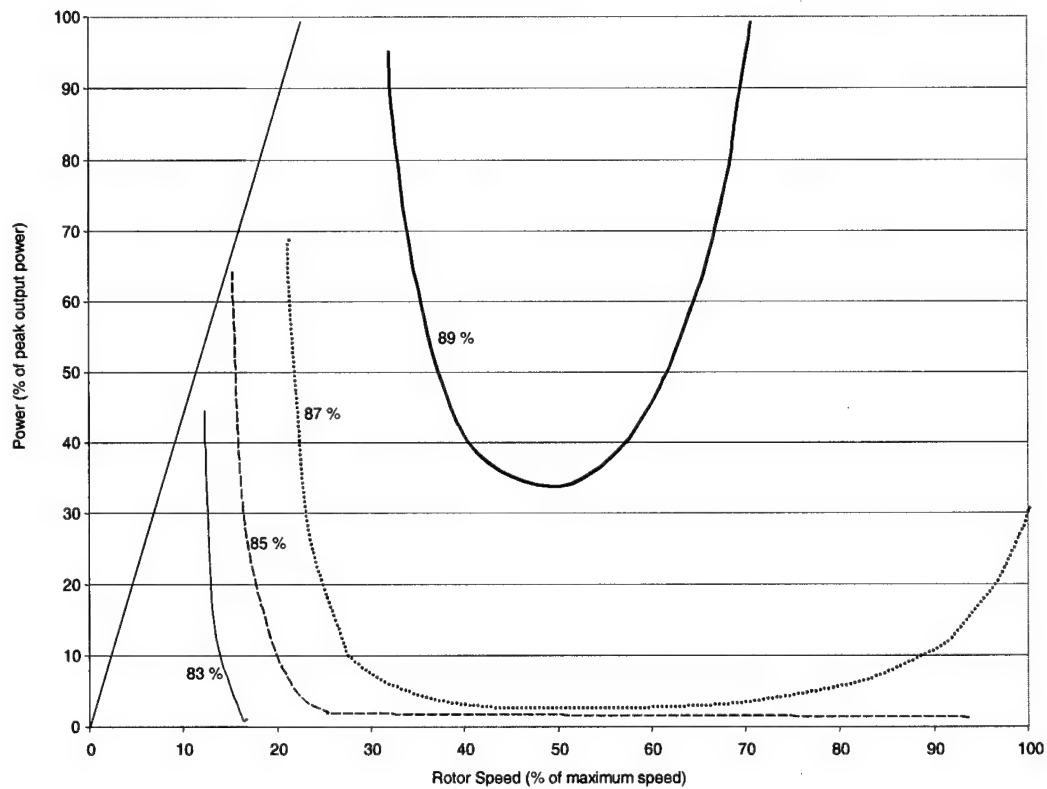


Figure A.2 Efficiency contours of a SRM.

Using the output power  $P_{di}$  required from the motor drive at the different time instants of a driving schedule, the average copper loss over the entire driving schedule, which determines the temperature rise of the electric motor, can be calculated using (A.1) as follows:

$$W_{cu} = \frac{W_{cup}}{N} \times \frac{\omega_{emr}}{P_{emp}} \times \left( \frac{P_{d1}}{\omega_1} + \frac{P_{d2}}{\omega_2} + \dots + \frac{P_{dN}}{\omega_N} \right)$$

$$\therefore W_{cu} = K_1 \times W_{cup} \quad (A.4)$$

Where

$$K_1 = \frac{1}{N} \times \frac{\omega_{emr}}{P_{emp}} \times \left( \frac{P_{d1}}{\omega_1} + \frac{P_{d2}}{\omega_2} + \dots + \frac{P_{dN}}{\omega_N} \right)$$

Using (A.2), the average eddy-current loss over the entire driving schedule is given by:

$$W_e = \frac{W_{ep}}{N} \times \frac{1}{P_{emp} \omega_{emr}} \times (P_{d1} \omega_1 + P_{d2} \omega_2 + \dots + P_{dN} \omega_N)$$

$$\therefore W_e = K_{2e} \times W_{ep} \quad (A.5)$$

Where  $K_{2e} = \frac{1}{N} \times \frac{1}{P_{emp} \omega_{emr}} \times (P_{d1} \omega_1 + P_{d2} \omega_2 + \dots + P_{dN} \omega_N)$

Using (A.3), the average hysteresis loss over the entire driving schedule is given by:

$$W_h = \frac{W_{hp}}{N} \times \frac{1}{P_{emp}^{0.8} \omega_{emr}^{0.2}} \times (C_1 + C_2 + \dots + C_N)$$

$$\therefore W_h = K_{2h} \times W_{hp} \quad (A.6)$$

Where  $K_{2h} = \frac{1}{N} \times \frac{1}{P_{emp}^{0.8} \omega_{emr}^{0.2}} \times (C_1 + C_2 + \dots + C_N)$

And  $C_i = P_{di}^{0.8} \omega_i^{0.2}$  for  $\omega_i \leq \omega_{emr}$

$$C_i = P_{di}^{0.8} \omega_i^{0.2} \times \sqrt{\frac{\omega_{emr}}{\omega_i}} \text{ for } \omega_i > \omega_{emr}$$

### A.3 Derivation of the Expression for $s_i$

Knowing the values of  $K_1$ ,  $K_{2e}$  and  $K_{2h}$  at a particular operating condition (e.g., a driving schedule), the total loss to be dissipated by the electric motor can be written using (A.4), (A.5) and (A.6) as follows:

$$W_{TOTAL} = K_1 \times W_{cup} + K_{2e} \times W_{ep} + K_{2h} \times W_{hp}$$

$$\therefore \frac{W_{TOTAL}}{W_{SRMp}} = K_1 \times (1 - c) + K_{2e} \times c \times f + K_{2h} \times c \times (1 - f)$$

The losses can be also written in terms of the continuous power rating  $P_{cont,i}$  that would result in the same losses as the operating condition under study by using (A.1), (A.2) and (A.3) as follows:

$$W_{TOTAL} = \frac{P_{cont,i}}{P_{emp}} \{W_{cup} + W_{ep}\} + \left( \frac{P_{cont,i}}{P_{emp}} \right)^{0.8} W_{hp}$$

$$\therefore \frac{W_{TOTAL}}{W_{SRMp}} = \frac{P_{cont,i}}{P_{emp}} \{(1 - c) + c \times f\} + \left( \frac{P_{cont,i}}{P_{emp}} \right)^{0.8} c \times (1 - f)$$

By setting  $s_i = \frac{P_{cont,i}}{P_{emp}}$  (2.1), the following equation results:

$$s_i \{(1 - c) + c \times f\} + s_i^{0.8} c \times (1 - f) = K_1 \times (1 - c) + K_{2e} \times c \times f + K_{2h} \times c \times (1 - f) \quad (2.2)$$

## References

- [1] T. J. E. Miller, Y. Hayashi, "A New Approach to Calculating Core Losses in the SRM", *IEEE Transactions on Industry Applications*, Vol. 31, No. 5, pp. 1039-1046, September/October 1995.
- [2] P. N. Materu, R. Krishnan, "Estimation of Switched Reluctance Motor Losses", *IEEE Transactions on Industry Applications*, Vol. 28, No. 3, pp. 668-679, May/June 1992.
- [3] S. Seely, Introduction to Electromagnetic Fields – McGraw Hill Book Company, Inc. – 3<sup>rd</sup> edition - Chapter 7.
- [4] W. F. Ray, P. J. Lawrenson, R. M. Davis, J. M. Stephenson, N. N. Fulton, R. J. Blake, "High Performance Switched Reluctance Brushless Drives", *IEEE Transactions on Industry Applications*, Vol. 22, No. 4, pp. 722-730, July/August 1986.

## Appendix B

### B.1 C++ Program for Sizing the SRM

This program was developed in C++ to take advantage of the Object Oriented Programming (OOP) features of the language. The EV and its electric motor drive are represented as two classes *vehicle* and *drive*, respectively, in which the data related to each are encapsulated. A friend function *interface* (vehicle,drive,float) enables calculation of the power ratings of the drive by implementing an interface between the vehicle and the drive for a given driving schedule. The advantage of such an OOP based code is its easy extensibility to multiple drives for one EV or multiple types of drives. For example, this code could also be easily extended for sizing the SRM drive for a *Hybrid EV*. The program is listed below:

#### srmsiz.c

/\*In this program, the drive power requirement is calculated based on the thought that for the velocity samples available, the drive power calculation will be at a instant exactly at the center of the period between the two instant where the velocity sample is available. Assuming a linear velocity profile between the two instants, the force from the road load characteristic can be calculated corresponding to the velocity at this center instant and the force for acceleration is the function of the end velocities and the time-difference\*/

```
#include <stdio.h>
#include <iostream.h>
#include <math.h>
```

```
//The parameters defined here are hard-coded and need to be changed for each case
#define kd 0.29    //dragging coefficient
#define kr 0.013   //rolling coefficient
#define mev 1172  //mass of electric vehicle
#define g 9.8      //acceleration due to gravity
#define Af 2.13    //Vehicle frontal Area
#define vhw 5.00   //Wind Velocity
#define ad 1.29    //Air Density
#define km 1.0     // rotational inertia coefficient
```

```
//The number of points in the schedule. This is identified during
//pre-processing, after reading the driving schedule file
int NumSch;
float MAX_RATIO,alpha;
```

```
//A structure for storing the time instant of the schedule and the drive
//power required
typedef struct
{
    float power;
    float time;
}
powerSch;
```

```

//Trapezoidal integrator. Takes the two end points and the step
//as input
inline float integr(float x1,float x2,float delv)
{
    float y;
    y=0.5*(x1+x2)*delv;
    return(y);
}

//Class drive pre-declared
class drive;

//Class vehicle declared and immediately defined
class vehicle
{
    float vev;//velocity of vehicle
    float fev;//force requirement of the vehicle
    float vevmax;//maximum velocity of vehicle
    float vevr;//rated velocity of vehicle
    float ta;//acceleration time to rated velocity

public:
    void inline calc_force();//function for force computation given velocity
    {
        fev=mev*g*(kr+alpha)+0.5*ad*kd*Af*(vev+vhw*0.4470)*(vev+vhw*0.4470);
    }
    void inval()
    {
        cout<<"Enter maximum velocity of car: ";
        cin >>vevmax;
        vevmax=vevmax*0.4470;
        cout<<"Enter rated velocity of car: ";
        cin>>vevr;
        vevr=vevr*0.4470;
        cout<<"Enter acceleration time of car: ";
        cin>>ta;
    }
    void calc_rat(int &k)
    {
        k=vevmax/vevr;
    }
    //Outputs the road-load characteristic
    void calc_curve()
    {
        FILE *fp;
        fp=fopen("curve","w");
        int i=0;
        float dk=vevmax/20;
        float k=0;
        float cruisePower=0;
        for (i=0;i<=20;i++)
        {
            vev=k;
            calc_force();
            cruisePower=fev*k/1000;
            fprintf(fp,"%7.2f %7.2f %7.2f\n",k/0.447,fev,cruisePower);
            k+=dk;
        }
        fclose(fp);
    }
}

//These functions do computations that require both the vehicle as

```

```

// well as the drive object
friend void cruisLoss(vehicle,drive);
friend void interface(vehicle,drive &,float);
friend void schedule(vehicle,drive &);
};

//Class drive defined
class drive
{
    float vemr;//rated speed of drive
    float pemr;//rated power of drive based on acceleration performance
    float pemrmax;//drive power requirement at maximum speed of vehicle
    powerSch *ps;//The power requirement of drive as per the schedule
public:
    void display()
    {
        cout<<"Power Rating= "<<pemr<<" kW; Rated Speed= "<<(vemr/0.4470)<<" mph"<<endl;
        cout<<endl;
    }
    void showSchedule()
    {
        int i=0;
        FILE *fp;
        fp=fopen("out","w");
        while (i<NumSch-1)
        {
            fprintf(fp,"%7.2f %7.2f\n",ps[i].time,ps[i].power);
            i++;
        }
        fclose(fp);
    }
    friend void cruisLoss(vehicle,drive);
    friend void interface(vehicle, drive &,float);
    friend void schedule(vehicle,drive &);
};

//Function calculates the drive losses at points between 0-max speed
// and stores in a file cruisLoss
void cruisLoss(vehicle c,drive m)
{
    float k=0;
    float dk=c.vevmax/200;
    float p;
    FILE *fp;
    float K1,K2E,K2H;
    fp=fopen("cruisLoss","w");
    while (k<=c.vevmax)
    {
        //Remove next two comments when you want at constant torque
        c.vev=k;/*c.vev=c.vevmax;*/
        c.calc_force();
        /*c.vev=k;*/
        p=c.fev*c.vev/1000;
        if (c.vev>0) K1=(p*m.vemr)/(c.vev*m.pemr);
        K2E=(p*c.vev)/(m.pemr*m.vemr);
        If ((c.vev>0)&&(p>0)&&(c.vev<=m.vemr)) K2H = ((exp(0.8*log(p/m.pemr)))
            *(exp(0.2*(c.vev/m.vemr))));
        if ((c.vev>0)&&(p>0)&&(c.vev>m.vemr)) K2H = ((exp(0.8*log(p/m.pemr))) *
            (exp(0.2*(c.vev/m.vemr))) * (exp(0.5*log(m.vemr/c.vev))));
        fprintf(fp,"%8.5f %8.5f %8.5f %8.5f %8.5f\n",p,(c.vev/0.4470),K1,K2E,K2H);
        k+=dk;
    }
}

```

```

        fclose(fp);
    }

//Function to calculate drive peak-power for a given vehicle performance
void interface(vehicle c,drive &m, float n)
{
    float pmr,dpmr;
    float vmr,dk;
    float vmrmax;
    float acc_time,ta;
    int k,l,flag;
    float v,vmin,x1,x2;
    ta=c.ta;
    c.vev=c.vevmax;
    vmrmax=c.vevmax;
    c.calc_force();
    pmr=c.fev*vmrmax;
    m.pemrmax=pmr;
    vmin=c.vevmax/n;
    dpmr=pmr/100;
    flag=0;
    while (!flag)
    {
        vmr=vmin;
        dk=c.vevr/1000;
        k=c.vevr/dk;
        acc_time=0.0;
        v=0.0;
        c.vev=0;
        c.calc_force();
        x2=vmr/(pmr-c.fev*vmr);
        for (l=1;l<=k;l++)
        {
            v=v+dk;
            if (v<=vmr)
            {
                c.vev=v;
                c.calc_force();
                x1=x2;
                x2=vmr/(pmr-c.fev*vmr);
                acc_time=acc_time+integr(x1,x2,dk);
            }
            else
            {
                c.vev=v;
                c.calc_force();
                x1=x2;
                x2=v/(pmr-c.fev*v);
                acc_time=acc_time+integr(x1,x2,dk);
            }
        }
        acc_time=acc_time*mev*km;
        if ((acc_time<=ta)&&(acc_time>=0))
        {
            flag=1;
            m.pemr=pmr/1000;
            m.vemr=vmr;
        }
        pmr=pmr+dpmr;
    }
}

```

```

//Function to calculate the constants K1,K2e and K2h
void schedule(vehicle c,drive &m)
{
    char drivFileName[100];
    cout<<"Please enter file-name for driving schedule:"<<endl;
    scanf("%s",drivFileName);
    FILE *fp;
    float veloc[10000];
    float time[10000];
    float driveFMax;
    float fChk;
    char ch;
    powerSch ps[10000];
    float F1,F2;
    float FEV=0;
    float K1,K2E,K2H;
    int i=0;
    NumSch=0;
    fp=fopen(drivFileName,"r");
    while ((ch=getc(fp))!=EOF)
    {
        if (ch=='\n')
        {
            NumSch++;
        }
    }
    fclose(fp);
    //ps=(powerSch *)malloc(NumSch*sizeof(powerSch));
    //veloc=(float *)malloc(NumSch*sizeof(float));
    //time=(float *)malloc(NumSch*sizeof(float));
    fp=fopen(drivFileName,"r");
    i=0;
    while (i<NumSch)
    {
        fscanf(fp,"%f %f\n",&time[i],&veloc[i]);
        i++;
    }
    for (i=0;i<NumSch;i++)
    {
        veloc[i]=veloc[i]*0.447;
    }
    fclose(fp);
    K1=0;
    K2E=0;
    K2H=0;
    for (i=0;i<(NumSch-1);i++)
    {
        F1=mev*(veloc[i+1]-veloc[i])/(time[i+1]-time[i]);
        c.vev=(veloc[i]+veloc[i+1])/2;
        c.calc_force();
        FEV=c.fev;
        F2=FEV;
        driveFMax=m.pemr*1000/m.vemr;
        if (c.vev>m.vemr) driveFMax=m.pemr*1000/c.vev;
        //The braking is always by mechanical means and motor produces
        //no power during this.
        //The above is over-ridden. Braking is always electrical now.
        ps[i].power=(F1+F2)*c.vev/1000;
        ps[i].time=(time[i]+time[i+1])/2;
        fChk=F1+F2;
        if (fChk<0) fChk=-fChk;
        if (fChk>driveFMax)

```

```

        {
            printf("At Time %7.2f",ps[i].time);
            printf(" drive capability violated\n");
        }
        if (veloc[i+1]<veloc[i])
        {
            if (ps[i].power<0) ps[i].power=-ps[i].power;
        }
        if (c.vev>0) K1=K1+(ps[i].power/c.vev);
        K2E=K2E+ps[i].power*c.vev;
        if ((c.vev>0)&&(ps[i].power>0)&&(c.vev<=m.vemr)) K2H = K2H +
            ((exp(0.8*log(ps[i].power/m.pemr))) * (exp(0.2*(c.vev/m.vemr))));
        if ((c.vev>0)&&(ps[i].power>0)&&(c.vev>m.vemr)) K2H = K2H +
            ((exp(0.8*log(ps[i].power/m.pemr))) * (exp(0.2*(c.vev/m.vemr))) * (exp(0.5*log(m.vemr/c.vev))));
    }
    m.ps=ps;
    K1=K1*m.vemr/(m.pemr*(NumSch-1));
    K2E=K2E/(m.vemr*m.pemr*(NumSch-1));
    K2H=K2H/(NumSch-1);
    printf("%7.5f %7.5f %7.5f\n",K1,K2E,K2H);
}

int main()
{
    vehicle car;
    drive srm;
    int k;
    float i;
    cout<<"Enter the maximum ratio:";
    cin>>MAX_RATIO;
    //MAX_RATIO Max. Ratio Maximum/Rated Speed upto which to compute
    i=MAX_RATIO;
    cout<<"Enter the gradient:";
    cin>>alpha;
    //alpha = Gradient
    car.inval();
    interface(car,srm,i);
    cout <<"Maximum Ratio Maximum/Rated Speed of Drive="<<i<<endl;
    srm.display();
    cruisLoss(car,srm);
    schedule(car,srm);
    car.calc_curve();
    srm.showSchedule();
}

```

## B.2 MATLAB™ Code for Sizing Other Motors

### A. PMSM

```

%Code for sizing the permanent magnet synchronous machine
clear all
clear,clc

xdr=.5; %the d-axis reactance at the rated drive speed
xqr=.66; %the q-axis reactance at the rated drive speed
vr=35; %the electric vehicle rated speed is 14 mph
vmax=70; %the electric vehicle maximum speed is 70 mph
E=0.8;
pr=1;

```

```

prated=49;%The peak power rating of the machine is known to be 28 kW at ratio
of 5 and 37 kW at ratio 2from optim.c
flag=0;
[idr,iqr]=computen(E,1,xdr,xqr,pr);
ir=sqrt(iqr^2+idr^2);
kfeer=((E+xdr*idr)/E)^2;
kfehr=((E+xdr*idr)/E)^1.6;
kcu=0;
kfee=0;
kfeh=0;
c=0.4;
f=0.3333;

%%%%%%%%%%%%%%%%%%%%%%%%%%%%%%%%%%%%%%%%%%%%%%%%%%%%%%%%%%%%%%%%%%%%%%%%%%%%%%UNCOMMENT DESIRED
%%%%%%%%%%%%%%%%%%%%%%%%%%%%%%%%%%%%%%%%%%%%%%%%%%%%%%%%%%%%%%%%%%%%%%%%%%%%%%SECTION
fid=fopen('pshwy.out','r');
[data,count]=fscanf(fid,'%f');
fclose(fid);
div=count/3;
%%%%%%%%%%%%%%%%%%%%%%%%%%%%%%%%%%%%%%%%%%%%%%%%%%%%%%%%%%%%%%%%%%%%%%%%%%%%%%UNCOMMENT DESIRED
%%%%%%%%%%%%%%%%%%%%%%%%%%%%%%%%%%%%%%%%%%%%%%%%%%%%%%%%%%%%%%%%%%%%%%%%%%%%%%SECTION
%count=3;
%data(1)=1;
%data(2)=20;
%data(3)=55*0.4470;
%count=3;
%div=count/3;
%%%%%%%%%%%%%%%%%%%%%%%%%%%%%%%%%%%%%%%%%%%%%%%%%%%%%%%%%%%%%%%%%%%%%%%%%%%%%%
for i=1:(count/3)
    k=data((i-1)*3+3)/0.4470/vr;
    if k<=1
        if k~=0
            [id,iq]=computen(E*k,k,k*xdr,k*xqr,(data((i-1)*3+2)/prated));
            i=sqrt(id^2+iq^2)/ir;
        end
        if k==0
            div=div-1;
        end
    else
        %[id,iq]=computen(E*k,1+((k-1)/4),k*xdr,k*xqr,(data((i-1)*3+2)/prated));
        [id,iq]=computen(E*k,1,k*xdr,k*xqr,(data((i-1)*3+2)/prated));
        i=sqrt(id^2+iq^2)/ir;
    end
    if k~=0
        kcu=kcu+i^2;
    end
    if k~=0
        kfee=kfee+(((E+xdr*id)/E)^2)*k^2/kfeer;
        kfeh=kfeh+(((E+xdr*id)/E)^1.6)*k/kfehr;
    end
end

kcu=kcu/div
kfee=kfee/div
kfeh=kfeh/div
w=kcu*(1-c)+kfee*c*f+kfeh*c*(1-f)
s=((w-c)/(1-c))^0.5

function [id,iq]=computen(Eb,V,Xd,Xq,P)
id=0;
delid=0.01;
iq=P/(Eb+(Xd-Xq)*id);

```

```

f=iq^2+((Xd/Xq)^2)*((id+(Eb/Xd))^2)-(V/Xq)^2;
while abs(f)>0.01
    id=id-delid;
    iq=P/(Eb+(Xd-Xq)*id);
    f=iq^2+((Xd/Xq)^2)*((id+(Eb/Xd))^2)-(V/Xq)^2;
end

```

## B. IM

```

%Code for sizing the induction machine
clear all
clear,clc

vr=35; %the electric vehicle rated speed is 14 mph
vmax=70; %the electric vehicle maximum speed is 70 mph
pr=1;
prated=49;%The peak power rating of the machine is known to be 28 kW at ratio
%%%%%%%%of 5 and 37 kW at a ratio of 2from optim.c
kcu=0;
kfee=0;
kfeh=0;
c=0.4;
f=0.3333;

%%%%%%%%For driving schedules%%%%%%%%%%%%%%%%%%%%%%%%
fid=fopen('psftp.out','r');
[data,count]=fscanf(fid,'%f');
fclose(fid);
div=count/3;
%%%%%%%%For cruising at maximum velocity%%%%%%%%%%%%%%%%
%count=3;
%data(1)=1;
%data(2)=19;
%data(3)=70*0.4470;
%count=3;
%div=count/3;
%%%%%%%%%%%%%%%%%%%%%%%%%%%%%%%%%%%%%%%%%%%%%%%%%%%%%%%%%%%%%%%%%%%%%%%%%%%%%%%%
for i=1:(count/3)
    k=data((i-1)*3+3)/0.4470/vr;
    p=data((i-1)*3+2)/prated;
    if k==0
        div=div-1;
    end
    if k<=1
        if k~=0
            kcu=kcu+(p/k)^2;
        end
    else
        kcu=kcu+p^2;
    end
    if k<=1
        if k~=0
            kfee=kfee+k^2;
            kfeh=kfeh+k;
        end
    else
        kfee=kfee+1;
        kfeh=kfeh+((1/k)^1.6)*k;
    end
end
end
kcu=kcu/div

```

```

kfee=kfee/div
kfeh=kfeh/div

w=kcu*(1-c)+kfee*c*f+kfeh*c*(1-f)
s=((w-c)/(1-c))^.5

```

### C. DC Motor

```

%Code for sizing the dc machine
clear all
clear,clc

vr=35; %the electric vehicle rated speed is 14 mph
vmax=70; %the electric vehicle maximum speed is 70 mph
pr=1;
prated=49;%The peak power rating of the machine is known to be 28 kW form
optim.c at ratio of 5
kcu=0;

%%%%%%%%%%%%%%%%%%%%%%%%%%%%%%%%%%%%%%%%%%%%%%%%%%%%%%%%%%%%%%%%%%%%%%%%
fid=fopen('psftp.out','r');
[data,count]=fscanf(fid,'%f');
fclose(fid);
div=count/3;
%%%%%%%%%%%%%%%%%%%%%%%%%%%%%%%%%%%%%%%%%%%%%%%%%%%%%%%%%%%%%%%%%%%%%%%%
%For cruising at maximum velocity%%%%%%%%%%%%%%%%%%%%%%%%%%%%%%%%%%%%%%%%%%%%%%%%%%%%%%%%%%%%%%%%%%%%%%%%
%count=3;
%data(1)=1;
%data(2)=20;
%data(3)=55*0.4470;
%count=3;
%div=count/3;
%%%%%%%%%%%%%%%%%%%%%%%%%%%%%%%%%%%%%%%%%%%%%%%%%%%%%%%%%%%%%%%%%%%%%%%%
for i=1:(count/3)
    k=data((i-1)*3+3)/0.4470/vr;
    p=data((i-1)*3+2)/prated;
    if k==0
        div=div-1;
    end
    if k<=1
        if k~=0
            kcu=kcu+(p/k)^2;
        end
    else
        kcu=kcu+p^2;
    end
end
kcu=kcu/div
w=kcu
s=kcu^.5

```

## Appendix C

### ANSYS CODE

#### C.1. 6/4 SRM

!This file calculates an electromagnetic solution of the SRM

!Written by: Shyam S.R.

!on: 11/8/99

!variables of the motor geometry:

```
sor=0.2321      !stator outside radius
smr=0.1775      !stator middle radius
sir=0.1510      !stator inside radius
ror=0.1490      !rotor outside radius
rmr=0.1043      !rotor middle radius
sr=0.0468       !shaft radius
spw=30          !stator pole width
rpw=32          !rotor pole width
theta=-30       !position of the rotor with respect to the stator (0 - -45)
nsp=6           !number of stator poles
nrp=nsp-2       !number of rotor poles
cww=360/nsp-spw !copper winding width
iagw=360/nrp-rpw !inner airgap width
mdepth=0.2981   !depth of the motor
current=258      !current applied to the windings
turns=16         !number of windings
```

!in the following, 1=phase a 2=phases a and b 3=phases a and c

phase=1 !which phases are excited

!calculate the angle from the origin to the top of the  
!small angle on the pole of the rotor

```
!numerator = num
num=tan(0*3.14159265/180)*(ror-rmr)+ror*sin(rpw/2*3.14159265/180)
phi=rpw/2!asin(num/rmr)*180/3.14159265
```

!enter the preprocessor of the program

/prep7

!define the element types to be used

et,1,plane13,0

!define the units (metric)

emunit,mks

!associate material properties (permeabilities) with element types

```
mp,murx,1,1      !air
mp,murx,2,1      !steel
mp,murx,3,1      !copper
```

!activate a data table to analyze the rotor and stator

!material properties and assign those properties a material number

TB,BH,4,,33  
TBPT,defi,771030.21,3.1  
TBPT,defi,691452.74,3.0  
TBPT,defi,611875.74,2.9  
TBPT,defi,532297.80,2.8  
TBPT,defi,452720.33,2.7  
TBPT,defi,373142.86,2.6  
TBPT,defi,293565.39,2.5  
TBPT,defi,213987.91,2.4  
TBPT,defi,134410.44,2.3  
TBPT,defi,77534.21,2.2  
TBPT,defi,43639.5,2.1  
TBPT,defi,310\*79.6,2  
TBPT,defi,190\*79.6,1.9  
TBPT,defi,100\*79.6,1.7875  
TBPT,defi,80\*79.6,1.747917  
TBPT,defi,56\*79.6,1.7  
TBPT,defi,40\*79.6,1.658333  
TBPT,defi,20\*79.6,1.6041667  
TBPT,defi,10\*79.6,1.552083  
TBPT,defi,8\*79.6,1.526042  
TBPT,defi,6.4\*79.6,1.5  
TBPT,defi,5\*79.6,1.46875  
TBPT,defi,4\*79.6,1.4479167  
TBPT,defi,3\*79.6,1.395833  
TBPT,defi,2.1\*79.6,1.3  
TBPT,defi,1.5\*79.6,1.1  
TBPT,defi,1.1\*79.6,0.9  
TBPT,defi,0.85\*79.6,0.7  
TBPT,defi,0.68\*79.6,0.5  
TBPT,defi,0.6\*79.6,.3854167  
TBPT,defi,0.54\*79.6,0.3  
TBPT,defi,0.4\*79.6,.1666667  
TBPT,defi,0.33\*79.6,0.1  
!TBPLOT,BH,4  
!define the resistivity of the copper windings

res=1.512

!associate the resistivity with the material number of copper

mp,rsvz,3,res

!activate cylindrical coordinate system

csys,1

!define nodes used in flux calculations

n,1,sor,-spw/2

n,2,sor,0

n,3,sor,spw/2

n,4,smr,-spw/2

n,5,smr,0

n,6,smr,spw/2

n,7,sor,180-spw/2

n,8,sor,180

n,9,sor,-180+spw/2

```

n,10,smr,180-spw/2
n,11,smr,180
n,12,smr,-180+spw/2

n,13,ror,rpw/2
n,14,ror,0
n,15,ror,-rpw/2

n,16,ror,180-rpw/2
n,17,ror,180
n,18,ror,-180+rpw/2

!define the keypoints of the SRM

!keypoints of the stator poles and copper windings

k,,sir,spw/2
k,,smr,spw/2
k,,sir,spw/2+cww/2
k,,smr,spw/2+cww/2
k,,sir,spw/2+cww
k,,smr,spw/2+cww
ksel,s,,,1,6
kgen,nsp,all,,,,360/nsp

!keypoints of the rotor and shaft

k,,rmr,theta-phi
k,,ror,theta-rpw/2
k,,ror,theta+rpw/2
k,,rmr,theta+phi
ksel,s,,,nsp*6+1,nsp*6+4
kgen,nrp,all,,,,360/nrp

!lines for the rotor poles

csys,0
1,6*nsp+1,6*nsp+2
1,6*nsp+3,6*nsp+4
1,6*nsp+5,6*nsp+6
1,6*nsp+7,6*nsp+8
1,6*nsp+9,6*nsp+10
1,6*nsp+11,6*nsp+12
1,6*nsp+13,6*nsp+14
1,6*nsp+15,6*nsp+16
csys,1

!select all keypoints of the SRM

ksel,all
kplot,all

!generate areas of the SRM

!areas of the stator ring

pcirc,smr,sor,0,spw
agen,2*nsp,all,,,,360/(2*nsp)

!areas of the airgap ring

pcirc,ror,sir,45+theta,135+theta
agen,nrp,2*nsp+1,,,,360/nrp

```

```

!areas of the rotor ring

pcirc,sr,rmr,theta,360/nrp+theta
agen,nrp,2*nsp+nrp+1,,,360/nrp

!area of the shaft

pcirc,,sr,theta,360+theta

!areas of the stator poles

a,1,2,nsp*6,nsp*6-1
agen,nsp,2*nsp+2*nrp+2,,,360/nsp

!areas of the copper windings

a,1,2,4,3
a,3,4,6,5
agen,nsp,3*nsp+2*nrp+2,3*nsp+2*nrp+3,,,360/nsp

!areas of the inner airgap area

a,nsp*6+3,nsp*6+4,nsp*6+5,nsp*6+6
agen,nrp,5*nsp+2*nrp+2,,,360/nrp

!areas of the rotor poles

a,nsp*6+1,nsp*6+2,nsp*6+3,nsp*6+4
agen,nrp,5*nsp+3*nrp+2,,,360/nrp

!merge coincident keypoints, lines, etc.

ksel,all
nummrg,kp

!glue all correct areas

asel,s,loc,x,smr,sor
aglu,e,all
asel,s,loc,x,sir,smr
aglu,e,all
asel,s,loc,x,rmr,smr
lsel,s,loc,x,smr
asll,u
lsel,s,loc,x,rmr
asll,u
aglu,e,all
asel,s,loc,x,rmr,ror
lsel,s,loc,x,sir
asll,u
aglu,e,all
asel,s,loc,x,0,rmr
aglu,e,all

!group common areas of the SRM together under a
!component name.

!stator ring

lsel,s,loc,x,sor
asll
cm,stator,area

```

```

aatt,4,,1

!windings

!phase=a (1)

*if,phase,eq,1,then

!positive copper windings of interest

asel,s,loc,x,sir,smr
asel,r,loc,y,spw/2+cww/4
asel,a,loc,y,180-spw/2-cww/4
asel,r,loc,x,sir,smr
cm,pwind,area
aatt,3,,1

!negative copper windings of interest

asel,s,loc,x,sir,smr
asel,r,loc,y,-spw/2-cww/4
asel,a,loc,y,-180+spw/2+cww/4
asel,r,loc,x,sir,smr
cm,nwind,area
aatt,3,,1

!non interest copper windings

asel,s,loc,x,sir,smr
asel,r,loc,y,-180+spw/2+.25*cww
*do,i,1,nsp
n=-180+spw/2+.25*cww+(360/nsp)*i
asel,a,loc,y,n,n
*enddo
asel,a,loc,y,-180+spw/2+.75*cww
*do,i,1,nsp
n=-180+spw/2+.75*cww+(360/nsp)*i
asel,a,loc,y,n,n
*enddo
asel,r,loc,x,sir,smr
cmsel,u,pwind
cmsel,u,nwind
cm,owind,area
aatt,3,,1

!phase=ab (2)

*elseif,phase,eq,2

!positive copper windings of interest

asel,s,loc,x,sir,smr
asel,r,loc,y,spw/2+cww/4
asel,a,loc,y,180-spw/2-cww/4
asel,a,loc,y,1.5*spw+1.25*cww
asel,a,loc,y,-180+spw/2+.75*cww
asel,r,loc,x,sir,smr
cm,pwind,area
aatt,3,,1

!negative copper windings of interest

asel,s,loc,x,sir,smr

```

```

asel,r,loc,y,-spw/2-cww/4
asel,a,loc,y,-180+spw/2+cww/4
asel,a,loc,y,spw/2+.75*cww
asel,a,loc,y,-180+1.5*spw+1.25*cww
asel,r,loc,x,sir,smr
cm,nwind,area
aatt,3,,1

!non interest copper windings

asel,s,loc,x,sir,smr
asel,r,loc,y,-180+spw/2+.25*cww
*do,i,1,nsp
n=-180+spw/2+.25*cww+(360/nsp)*i
asel,a,loc,y,n,n
*enddo
asel,a,loc,y,-180+spw/2+.75*cww
*do,i,1,nsp
n=-180+spw/2+.75*cww+(360/nsp)*i
asel,a,loc,y,n,n
*enddo
asel,r,loc,x,sir,smr
cmsel,u,pwind
cmsel,u,nwind
cm,owind,area
aatt,3,,1

!phase=ac (3)

*elseif,phase,eq,3

!positive copper windings of interest

asel,s,loc,x,sir,smr
asel,r,loc,y,spw/2+cww/4
asel,a,loc,y,180-spw/2-cww/4
asel,a,loc,y,180-spw/2-.75*cww
asel,a,loc,y,-1.5*spw-1.25*cww
asel,r,loc,x,sir,smr
cm,pwind,area
aatt,3,,1

!negative copper windings of interest

asel,s,loc,x,sir,smr
asel,r,loc,y,-spw/2-cww/4
asel,a,loc,y,-180+spw/2+cww/4
asel,a,loc,y,180-1.5*spw-1.25*cww
asel,a,loc,y,-.5*spw-.75*cww
asel,r,loc,x,sir,smr
cm,nwind,area
aatt,3,,1

!non interest copper windings

asel,s,loc,x,sir,smr
asel,r,loc,y,-180+spw/2+.25*cww
*do,i,1,nsp
n=-180+spw/2+.25*cww+(360/nsp)*i
asel,a,loc,y,n,n
*enddo
asel,a,loc,y,-180+spw/2+.75*cww
*do,i,1,nsp

```

```

n=-180+spw/2+.75*cww+(360/nsp)*i
asel,a,loc,y,n,n
*enddo
asel,r,loc,x,sir,smr
cmsel,u,pwind
cmsel,u,nwind
cm,owind,area
aatt,3,,1

*endif

!calculate the area of the positive windings and
!assign the value to the variable poswind

cmsel,s,pwind
asum
*get,poswind,area,,area

!calculate the area of the negative windings and
!assign the value to the variable negwind

cmsel,s,nwind
asum
*get,negwind,area,,area

!stator poles:

asel,s,loc,x,sir,smr
cmsel,u,pwind
cmsel,u,nwind
cmsel,u,owind
cmsel,u,stator
cm,spole,area
aatt,4,,1

!shaft

asel,s,loc,x,0
cm,shaft,area
aatt,2,,1

!airgap ring

lssel,s,loc,x,sir
asll
cmsel,u,spole
cmsel,u,nwind
cmsel,u,pwind
cmsel,u,owind
cm,airgap,area
aatt,1,,1

!rotor ring
lssel,s,loc,x,sr
asll
cmsel,u,shaft
cm,rotor,area
aatt,4,,1

!all inner airgap areas

asel,s,loc,x,rmr,ror

```

```

asel,r,loc,y,-180+rpw/2+iagw/2+theta
*do,i,1,nrp
n=-180+rpw/2+iagw/2+(360/nrp)*i+theta
asel,a,loc,y,n,n
*enddo
asel,r,loc,x,rmr,ror
cmsel,u,airgap
cm,inag,area
aatt,1,,1

```

```

!rotor poles
lsl,s,loc,x,rmr
asll
cmsel,u,rotor
cmsel,u,inag
cm,rpole,area
aatt,4,,1

```

```

!size lines for meshing

```

```

cmsel,s,airgap
lsla
lsl,r,loc,x,sir
lesize,all,,160
lsla
lsl,r,loc,x,ror
lesize,all,,160

```

```

cmsel,s,stator
lsla
lsl,r,loc,x,sor
lesize,all,,8
lsla
lsl,r,loc,x,smr
lesize,all,,8
lsla
lesize,all,,3,.8

```

```

cmsel,s,spole
lsla
lsl,r,loc,x,sir
lesize,all,,18
lsla
lsl,r,loc,x,smr
lesize,all,,18

```

```

cmsel,s,owind
cmsel,a,nwind
cmsel,a,pwind
lsla
lsl,r,loc,x,sir
lesize,all,,9
lsla
lsl,r,loc,x,smr
lesize,all,,9

```

```

lsl,s,loc,y,-180+spw/2+cww
*do,i,1,nsp
n=-180+spw/2+cww+(spw+cww)*i
lsl,a,loc,y,n,n
*enddo
lsl,r,loc,x,sir,smr
lesize,all,,16,.6

```

```

lsel,s,loc,y,-180+spw/2
*do,i,1,nsp
n=-180+spw/2+(spw+cwv)*i
lsel,a,loc,y,n,n
*enddo
lsel,r,loc,x,sir,smr
lesize,all,,,16,1.66667

cmsel,s,owind
cmsel,a,nwind
cmsel,a,pwind
lsla
lesize,all,,,16,.6

cmsel,s,rpole
lsla
lsel,r,loc,x,ror
lesize,all,,,20
lsla
lsel,r,loc,x,rmr
lesize,all,,,20
lsla
lesize,all,,,12

cmsel,s,inag
lsla
lsel,r,loc,x,ror
lesize,all,,,20
lsla
lsel,r,loc,x,rmr
lesize,all,,,20

cmsel,s,rotor
lsla
lsel,r,loc,x,rmr
lesize,all,,,12
lsla
lsel,r,loc,x,sr
lesize,all,,,12
lsla
lesize,all,,,5,.8

allsel
amesh,all

!constraint equations

!stator ring to poles and windings

allsel
esel,none
cmsel,s,stator
lsla
lsel,r,loc,x,smr
nsll,s
esln
cmsel,s,spole
cmsel,a,owind
cmsel,a,nwind
cmsel,a,pwind
lsla
lsel,r,loc,x,smr

```

```

nsll,a
ceintf

!airgap to stator poles and windings

allsel
esel,none
cmsel,s,spole
cmsel,a,owind
cmsel,a,nwind
cmsel,a,pwind
lsla
lsel,r,loc,x,sir
nsll,s
esln
cmsel,s,airgap
lsla
lsel,r,loc,x,sir
nsll,a
ceintf

!airgap to rotor poles and inner airgap region
allsel
esel,none
cmsel,s,rpole
cmsel,a,inag
lsla
lsel,r,loc,x,rer
nsll,s
esln
cmsel,s,airgap
lsla
lsel,r,loc,x,rer
nsll,a
ceintf

!rotor poles and inner airgap region to rotor yoke
allsel
esel,none
cmsel,s,rotor
lsla
lsel,r,loc,x,rer
nsll,s
esln
cmsel,s,rpole
cmsel,a,inag
lsla
lsel,r,loc,x,rer
nsll,a
ceintf

finish          !the preprocessor is finished

/solution

!the solution sequence is to solve the problem over two load steps
!the first load step obtains an approximate solution
!the second load step obtains a converged solution
!the analysis is static by default
!the Newton-Raphson option is by default

!unselect all components

```

```

cmsel,none

!select the components of the SRM that a current density will be applied
!to and then select all elements of those components. After this, the
!bfe command applies the current density to the selected elements.

!phase=a (1)

*if,phase,eq,1,then

cmsel,s,nwind
esla,s
bfe,all,js,3,-current*turns*2/negwind    !-Z direction
cmsel,none
cmsel,s,pwind
esla,s
bfe,all,js,3,current*turns*2/poswind      !+Z direction

!phase=ab (2)

*elseif,phase,eq,2

cmsel,s,nwind
esla,s
bfe,all,js,3,-current*turns*4/negwind    !-Z direction
cmsel,none
cmsel,s,pwind
esla,s
bfe,all,js,3,current*turns*4/poswind      !+Z direction

!phase=ac (3)

*elseif,phase,eq,3

cmsel,s,nwind
esla,s
bfe,all,js,3,-current*turns*4/negwind    !-Z direction
cmsel,none
cmsel,s,pwind
esla,s
bfe,all,js,3,current*turns*4/poswind      !+Z direction

*endif

!far-field boundary conditions

allsel
nsel,s,loc,x,sor
d,all,az,0

!select all entities of the SRM for the solution

allsel

!first load step

neqit,1                                !1 equilibrium iteration
nsubst,5                              !5 substeps
outres,all,none                        !do not save results data
solve                                  !solve the first load step

!second load step

```

```

neqit,20                !up to 20 equilibrium iterations
nsubst,1                !1 substep
cnvtol,csg,,1e-7        !convergence criteria
outres,all,last         !save converged solution
solve                   !solve the second load step

finish                  !the solution is finished

!start the postprocessing

/post1

!return results in cylindrical coordinate system

rsys,1

!calculate the stored energy of the srm

!arg1=material # of first material
!arg2=material # of last material
!arg3=increment of the material #
!units are per length

allsel

/nopr
parsav,all,sasimac
esel,s,mat,,1,4,1
etable,sene,sene
/out,scratch
ssum
/out
*get,energy,ssum,,item,sene
/gopr
menergy=energy*mdepth

esel,s,mat,,1,4,1
senergy,1,0
coen=c_eng*mdepth

esel,s,mat,,1,4,1
senergy,0,0
ener=s_eng*mdepth

lnkage=(ener+coen)/current

!calculate the airgap torque

allsel
cmsel,s,airgap
esla
torqc2d,ror+((sir-ror)/2),100
agtorque=torque*mdepth

parsav,scalar,parameters

!plots

!flux lines

allsel
!plf2d,54

```

```

!azr
cmsel,s,rpole
cmsel,a,rotor
cmsel,a,shaft
nsla
nsel,a,loc,x,0,rmr
plnsol,a,z

```

## C.2. 8/6 SRM

The code for constructing the geometry and executing the run is almost the same as for the three-phase 6/4 SRM. The difference is in the initial assignment of dimensions, angle, number of stator and rotor poles, the selection of winding areas, meshing and assignment of negative or positive *current sheets*. By current sheet, we mean the product of coil turns and coil current that will be encountered in the cross-section of the coil in the 2D FEA model.

### A. Assignment of Dimensions and Other Values

```

sor=0.1851      !stator outside radius
smr=0.1524      !stator middle radius
sir=0.1195      !stator inside radius
ror=0.1183      !rotor outside radius
rmr=0.0828      !rotor middle radius
sr =0.0477      !shaft radius
spw=22.5        !stator pole width
rpw=24.5        !rotor pole width
nsp=8           !number of stator poles
nrp=nsp-2       !number of rotor poles
cww=360/nsp-spw !copper winding width
iagw=360/nrp-rpw !inner airgap width
mdepth=0.2366   !depth of the motor
arg2=131.1517    !current working-|current in two adjacent phases
arg3=131.1517    !current leading-|under short-flux-path mode
theta=-22.5      !angle of rotor pole wrt stator pole
turns=25         !number of windings

```

### B. Selection of Winding Areas

```

!windings

!positive copper windings of interest

asel,s,loc,x,sir,smr
asel,r,loc,y,spw/2+cww/4
asel,a,loc,y,180-spw/2-cww/4
asel,r,loc,x,sir,smr
cm,pwind2,area
aatt,3,,1

asel,s,loc,x,sir,smr
asel,r,loc,y,spw/2+.75*cww
asel,a,loc,y,-180+1.5*spw+1.25*cww
asel,r,loc,x,sir,smr
cm,pwind3,area

```

```

aatt,3,,1

!negative copper windings of interest

asel,s,loc,x,sir,smr
asel,r,loc,y,-spw/2-cww/4
asel,a,loc,y,-180+spw/2+cww/4
asel,r,loc,x,sir,smr
cm,nwind2,area
aatt,3,,1

asel,s,loc,x,sir,smr
asel,r,loc,y,1.5*spw+1.25*cww
asel,a,loc,y,-180+spw/2+.75*cww
asel,r,loc,x,sir,smr
cm,nwind3,area
aatt,3,,1

!non interest copper windings

asel,s,loc,x,sir,smr
asel,r,loc,y,-180+spw/2+.25*cww
*do,i,1,nsp
n=-180+spw/2+.25*cww+(360/nsp)*i
asel,a,loc,y,n,n
*enddo
asel,a,loc,y,-180+spw/2+.75*cww
*do,i,1,nsp
n=-180+spw/2+.75*cww+(360/nsp)*i
asel,a,loc,y,n,n
*enddo
asel,r,loc,x,sir,smr
cmsel,u,pwind2
cmsel,u,pwind3
cmsel,u,nwind2
cmsel,u,nwind3
cm,owind,area
aatt,3,,1

!calculate the area of the positive windings and
!assign the value to the variable poswind

cmsel,s,pwind2
asum
*get,poswind,area,,area

!calculate the area of the negative windings and
!assign the value to the variable negwind

cmsel,s,nwind2
asum
*get,negwind,area,,area

```

### C. Meshing

```

!size lines for meshing

cmsel,s,stator
lsla
lsel,r,loc,x,sor

```

```

lesize,all,,10
lsla
lsel,r,loc,x,smr
lesize,all,,10

cmsel,s,spole
lsla
lsel,r,loc,x,sir
lesize,all,,2
lsla
lsel,r,loc,x,smr
lesize,all,,2

cmsel,s,owind
cmsel,a,nwind2
cmsel,a,nwind3
cmsel,a,pwind2
cmsel,a,pwind3
lsla
lsel,r,loc,x,sir
lesize,all,,2
lsla
lsel,r,loc,x,smr
lesize,all,,2

lsel,s,loc,y,-180+spw/2+cww
*do,i,1,nsp
n=-180+spw/2+cww+(spw+cww)*i
lsel,a,loc,y,n,n
*enddo
lsel,r,loc,x,sir,smr
lesize,all,,,12,.6

lsel,s,loc,y,-180+spw/2
*do,i,1,nsp
n=-180+spw/2+(spw+cww)*i
lsel,a,loc,y,n,n
*enddo
lsel,r,loc,x,sir,smr
lesize,all,,,12,1.6667

lsel,s,loc,y,-180+spw/2+cww/2
*do,i,1,nsp
n=-180+spw/2+cww/2+(spw+cww)*i
lsel,a,loc,y,n,n
*enddo
lsel,r,loc,x,smr,sor
lesize,all,,,3

lsel,s,loc,y,-180
*do,i,1,nsp
n=-180+(spw+cww)*i
lsel,a,loc,y,n,n
*enddo
lsel,r,loc,x,sir,smr
lesize,all,,,12,.6

cmsel,s,owind
cmsel,a,nwind2
cmsel,a,nwind3
cmsel,a,pwind2
cmsel,a,pwind3
lsla

```

```

lesize,all,,,12,.6

cmsel,s,rpole
lsla
lsel,r,loc,x,rer
lesize,all,,3
lsla
lsel,r,loc,x,rer
lesize,all,,3

cmsel,s,rpole
lsla
lsel,u,loc,x,rer
lsel,u,loc,x,rer
k=1
*do,i,1,nrp
lsel,u,line,k,k
k=k+2*nrp
*enddo
lesize,all,,,12,1.25

cmsel,s,rpole
lsla
lsel,u,loc,x,rer
lsel,u,loc,x,rer
k=2
*do,i,1,nrp
lsel,u,line,k,k
k=k+2*nrp
*enddo
lesize,all,,,12,.8

cmsel,s,inag
lsla
lsel,r,loc,x,rer
lesize,all,,3
lsla
lsel,r,loc,x,rer
lesize,all,,3

cmsel,s,inag
lsla
lsel,u,loc,x,rer
lsel,u,loc,x,rer
k=1
*do,i,1,nrp
lsel,u,line,k,k
k=k+2*nrp
*enddo
lesize,all,,,12,1.1

cmsel,s,inag
lsla
lsel,u,loc,x,rer
lsel,u,loc,x,rer
k=2
*do,i,1,nrp
lsel,u,line,k,k
k=k+2*nrp
*enddo
lesize,all,,,12,.9

cmsel,s,rotor

```

```

lsla
lsel,r,loc,x,rmr
lesize,all,,5
lsla
lsel,r,loc,x,sr
lesize,all,,5

cmsel,s,rotor
lsla
lsel,u,loc,x,rmr
lsel,u,loc,x,sr
lesize,all,,8

cmsel,s,airgap
lsla
lsel,r,loc,x,sir
lesize,all,,.25
lsla
lsel,r,loc,x,rer
lesize,all,,0.25
lsla
lsel,u,loc,x,sir
lsel,u,loc,x,rer
lesize,all,,2

allsel
amesh,all

```

#### *D. Assignment of Current Sheets*

```

!unselect all components

cmsel,none

!select the components of the SRM that a current density will be applied
!to and then select all elements of those components. After this, the
!bfe command applies the current density to the selected elements.

cmsel,s,nwind2
esla,s
bfe,all,js,3,-arg2*turns*2/negwind    !-Z direction
cmsel,none
cmsel,s,pwind2
esla,s
bfe,all,js,3,arg2*turns*2/poswind      !+Z direction

cmsel,s,nwind3
esla,s
bfe,all,js,3,-arg3*turns*2/negwind    !-Z direction
cmsel,none
cmsel,s,pwind3
esla,s
bfe,all,js,3,arg3*turns*2/poswind      !+Z direction

```

### **C.3. 10/8 SRM**

The code is similar to that for the four-phase 8/6 SRM. The main difference is in the assignment of values and meshing section.

### A. Assignment of Dimensions and Other Values

|                  |                         |
|------------------|-------------------------|
| sor=0.1856       | !stator outside radius  |
| smr=0.1594       | !stator middle radius   |
| sir=0.1195       | !stator inside radius   |
| ror=0.1183       | !rotor outside radius   |
| rmr=0.0828       | !rotor middle radius    |
| sr =0.054        | !shaft radius           |
| spw=18           | !stator pole width      |
| rpw=20           | !rotor pole width       |
| nsp=10           | !number of stator poles |
| arg1=-18         | !Theta                  |
| arg2=131.153     | !Current working        |
| arg3=131.153     | !Current leading        |
| nrp=nsp-2        | !number of rotor poles  |
| cww=360/nsp-spw  | !copper winding width   |
| iagw=360/nrp-rpw | !inner airgap width     |
| mdepth=0.2366    | !depth of the motor     |
| turns=25         | !number of windings     |

### B. Meshing

!size lines for meshing

```
cmsel,s,airgap
lsla
lsel,r,loc,x,sir
lesize,all,,0.25
lsla
lsel,r,loc,x,ror
lesize,all,,0.25
lsla
lesize,all,,2
```

```
cmsel,s,stator
lsla
lsel,r,loc,x,sor
lesize,all,,10
lsla
lsel,r,loc,x,smr
lesize,all,,10
```

```
cmsel,s,spole
lsla
lsel,r,loc,x,sir
lesize,all,,2
lsla
lsel,r,loc,x,smr
lesize,all,,2
```

```
cmsel,s,owind
cmsel,a,nwind2
cmsel,a,nwind3
cmsel,a,pwind2
cmsel,a,pwind3
lsla
lsel,r,loc,x,sir
lesize,all,,2
lsla
lsel,r,loc,x,smr
lesize,all,,2
```

```

lsel,s,loc,y,-180+spw/2+cww
*do,i,1,nsp
n=-180+spw/2+cww+(spw+cww)*i
lsel,a,loc,y,n,n
*enddo
lsel,r,loc,x,sir,smr
lesize,all,,12,.6

lsel,s,loc,y,-180+spw/2
*do,i,1,nsp
n=-180+spw/2+(spw+cww)*i
lsel,a,loc,y,n,n
*enddo
lsel,r,loc,x,sir,smr
lesize,all,,12,1.6667

lsel,s,loc,y,-180+spw/2+cww/2
*do,i,1,nsp
n=-180+spw/2+cww/2+(spw+cww)*i
lsel,a,loc,y,n,n
*enddo
lsel,r,loc,x,smr,sor
lesize,all,,3

lsel,s,loc,y,-180
*do,i,1,nsp
n=-180+(spw+cww)*i
lsel,a,loc,y,n,n
*enddo
lsel,r,loc,x,sir,smr
lesize,all,,12,.6

cmsel,s,owind
cmsel,a,nwind2
cmsel,a,nwind3
cmsel,a,pwind2
cmsel,a,pwind3
lsla
lesize,all,,12,.6

cmsel,s,rpole
lsla
lsel,r,loc,x,rer
lesize,all,,3
lsla
lsel,r,loc,x,rnr
lesize,all,,3

cmsel,s,rpole
lsla
lsel,u,loc,x,rer
lsel,u,loc,x,rnr
k=1
*do,i,1,nrp
lsel,u,line,k,k
k=k+2*nrp
*enddo
lesize,all,,12,1.25

cmsel,s,rpole
lsla
lsel,u,loc,x,rer

```

```

lssel,u,loc,x,rmr
k=2
*do,i,1,nrp
lssel,u,line,k,k
k=k+2*nrp
*enddo
lesize,all,,,12,.8

cmsel,s,inag
lsla
lssel,r,loc,x,ror
lesize,all,,3
lsla
lssel,r,loc,x,rmr
lesize,all,,3

cmsel,s,inag
lsla
lssel,u,loc,x,ror
lssel,u,loc,x,rmr
k=1
*do,i,1,nrp
lssel,u,line,k,k
k=k+2*nrp
*enddo
lesize,all,,,12,1.1

cmsel,s,inag
lsla
lssel,u,loc,x,ror
lssel,u,loc,x,rmr
k=2
*do,i,1,nrp
lssel,u,line,k,k
k=k+2*nrp
*enddo
lesize,all,,,12,.9

cmsel,s,rotor
lsla
lssel,r,loc,x,rmr
lesize,all,,5
lsla
lssel,r,loc,x,sr
lesize,all,,5

cmsel,s,rotor
lsla
lssel,u,loc,x,rmr
lssel,u,loc,x,sr
lesize,all,,,8

allsel
amesh,all

```

#### C.4. 12/8 SRM

The main difference in the code for the single-phase-excited three-phase 12/8 SRM is that quadrature current sheets carry same direction of current resulting in local short paths for the flux.

The assignment, meshing, winding areas selection and the current sheet application code are listed below.

#### A. Assignment of Dimensions and Other Values

```
!This file calculates an electromagnetic solution of the SRM
!This is the file for the 12/8 SRM using single-phase excitation
!Quadrature current sheets carry same direction current. This
!corresponds to single phase excitation case of 6/4 SRM.
!The self and mutual inductances in these quadrature phases together
!contribute to the net torque.

!Written by: Shyam S.R.
!on: 11/6/99

!variables of the motor geometry:

sor=0.1876      !stator outside radius
smr=0.1657      !stator middle radius
sir=0.1195      !stator inside radius
ror=0.1183      !rotor outside radius
rmr=0.0828      !rotor middle radius
sr=0.0583       !shaft radius
spw=15          !stator pole width
rpw=17          !rotor pole width
theta=-15       !position of the rotor with respect to the stator (0 - -
22.5)
nsp=12          !number of stator poles
nrp=nsp-4       !number of rotor poles
cww=360/nsp-spw !copper winding width
iagw=360/nrp-rpw !inner airgap width
mdepth=0.2366   !depth of the motor
current=131.1527 !current applied to the windings
turns=25        !number of windings
```

#### B. Selection of Winding Areas

```
!windings

!phase=a (1)

*if,phase,eq,1,then

!positive copper windings of interest

asel,s,loc,x,sir,smr
asel,r,loc,y,spw/2+cww/4
asel,a,loc,y,90-spw/2-cww/4
asel,a,loc,y,180+spw/2+cww/4
asel,a,loc,y,-90-spw/2-cww/4
asel,r,loc,x,sir,smr
cm,pwind,area
aatt,3,,1

!negative copper windings of interest

asel,s,loc,x,sir,smr
asel,r,loc,y,-spw/2-cww/4
asel,a,loc,y,90+spw/2+cww/4
asel,a,loc,y,180-spw/2-cww/4
```

```

asel,a,loc,y,-90+spw/2+cww/4
asel,r,loc,x,sir,smr
cm,nwind,area
aatt,3,,1

!non interest copper windings

asel,s,loc,x,sir,smr
asel,r,loc,y,-180+spw/2+.25*cww
*do,i,1,nsp
n=-180+spw/2+.25*cww+(360/nsp)*i
asel,a,loc,y,n,n
*enddo
asel,a,loc,y,-180+spw/2+.75*cww
*do,i,1,nsp
n=-180+spw/2+.75*cww+(360/nsp)*i
asel,a,loc,y,n,n
*enddo
asel,r,loc,x,sir,smr
cmsel,u,pwind
cmsel,u,nwind
cm,owind,area
aatt,3,,1

!phase=ab (2)

*elseif,phase,eq,2

!positive copper windings of interest

asel,s,loc,x,sir,smr
asel,r,loc,y,spw/2+cww/4
asel,a,loc,y,180-spw/2-cww/4
asel,a,loc,y,1.5*spw+1.25*cww
asel,a,loc,y,-180+spw/2+.75*cww
asel,r,loc,x,sir,smr
cm,pwind,area
aatt,3,,1

!negative copper windings of interest

asel,s,loc,x,sir,smr
asel,r,loc,y,-spw/2-cww/4
asel,a,loc,y,-180+spw/2+cww/4
asel,a,loc,y,spw/2+.75*cww
asel,a,loc,y,-180+1.5*spw+1.25*cww
asel,r,loc,x,sir,smr
cm,nwind,area
aatt,3,,1

!non interest copper windings

asel,s,loc,x,sir,smr
asel,r,loc,y,-180+spw/2+.25*cww
*do,i,1,nsp
n=-180+spw/2+.25*cww+(360/nsp)*i
asel,a,loc,y,n,n
*enddo
asel,a,loc,y,-180+spw/2+.75*cww
*do,i,1,nsp
n=-180+spw/2+.75*cww+(360/nsp)*i
asel,a,loc,y,n,n
*enddo

```

```

asel,r,loc,x,sir,smr
cmsel,u,pwind
cmsel,u,nwind
cm,owind,area
aatt,3,,1

!phase=ac (3)

*elseif,phase,eq,3

!positive copper windings of interest

asel,s,loc,x,sir,smr
asel,r,loc,y,spw/2+cww/4
asel,a,loc,y,180-spw/2-cww/4
asel,a,loc,y,180-spw/2-.75*cww
asel,a,loc,y,-1.5*spw-1.25*cww
asel,r,loc,x,sir,smr
cm,pwind,area
aatt,3,,1

!negative copper windings of interest

asel,s,loc,x,sir,smr
asel,r,loc,y,-spw/2-cww/4
asel,a,loc,y,-180+spw/2+cww/4
asel,a,loc,y,180-1.5*spw-1.25*cww
asel,a,loc,y,-.5*spw-.75*cww
asel,r,loc,x,sir,smr
cm,nwind,area
aatt,3,,1

!non interest copper windings

asel,s,loc,x,sir,smr
asel,r,loc,y,-180+spw/2+.25*cww
*do,i,1,nsp
n=-180+spw/2+.25*cww+(360/nsp)*i
asel,a,loc,y,n,n
*enddo
asel,a,loc,y,-180+spw/2+.75*cww
*do,i,1,nsp
n=-180+spw/2+.75*cww+(360/nsp)*i
asel,a,loc,y,n,n
*enddo
asel,r,loc,x,sir,smr
cmsel,u,pwind
cmsel,u,nwind
cm,owind,area
aatt,3,,1

*endif

!calculate the area of the positive windings and
!assign the value to the variable poswind

cmsel,s,pwind
asum
*get,poswind,area,,area

!calculate the area of the negative windings and
!assign the value to the variable negwind

```

```

cmsel,s,nwind
asum
*get,negwind,area,,area

```

### C. Meshing

```

!size lines for meshing

```

```

cmsel,s,spole
lsla
lsl,r,loc,x,sir
lesize,all,,6
lsla
lsl,r,loc,x,smr
lesize,all,,6

```

```

cmsel,s,owind
cmsel,a,nwind
cmsel,a,pwind
lsla
lsl,r,loc,x,sir
lesize,all,,6
lsla
lsl,r,loc,x,smr
lesize,all,,6

```

```

cmsel,s,stator
lsla
lsl,r,loc,x,sor
lesize,all,,3
lsla
lsl,r,loc,x,smr
lesize,all,,3

```

```

lsl,s,loc,y,0
*do,i,1,2*nsp
n=spw*i
lsl,a,loc,y,n,n
*enddo
lsl,r,loc,x,smr,sor
lesize,all,,3,.8

```

```

lsl,s,loc,y,-180+spw/2+cww
*do,i,1,nsp
n=-180+spw/2+cww+(spw+cww)*i
lsl,a,loc,y,n,n
*enddo
lsl,r,loc,x,sir,smr
lesize,all,,16,.6

```

```

lsl,s,loc,y,-180+spw/2
*do,i,1,nsp
n=-180+spw/2+(spw+cww)*i
lsl,a,loc,y,n,n
*enddo
lsl,r,loc,x,sir,smr
lesize,all,,16,1.66667

```

```

cmsel,s,owind
cmsel,a,nwind
cmsel,a,pwind

```

```

lsla
lesize,all,,16,.6

cmsel,s,rpole
lsla
lsel,r,loc,x,ror
lesize,all,,10
lsla
lsel,r,loc,x,rnr
lesize,all,,10
lsla
lesize,all,,12

cmsel,s,inag
lsla
lsel,r,loc,x,ror
lesize,all,,10
lsla
lsel,r,loc,x,rnr
lesize,all,,2

cmsel,s,rotor
lsla
lsel,r,loc,x,rnr
lesize,all,,6
lsla
lsel,r,loc,x,sr
lesize,all,,6
lsla
lesize,all,,5,.8

cmsel,s,airgap
lsla
lsel,r,loc,x,sir
lesize,all,,.25
lsla
lsel,r,loc,x,ror
lesize,all,,0.25
lsla
lsel,u,loc,x,sir
lsel,u,loc,x,ror
lesize,all,,2

allsel
amesh,all

```

#### *D. Assignment of Current Sheets*

```

!unselect all components

cmsel,none

!select the components of the SRM that a current density will be applied
!to and then select all elements of those components. After this, the
!bfe command applies the current density to the selected elements.

!phase=a (1)

*if,phase,eq,1,then

cmsel,s,nwind
esla,s
bfe,all,js,3,-current*turns*4/negwind    !-Z direction

```

```

cmshel,none
cmshel,s,pwind
esla,s
bfe,all,js,3,current*turns*4/poswind      !+Z direction

!phase=ab (2)

*elseif,phase,eq,2

cmshel,s,nwind
esla,s
bfe,all,js,3,-current*turns*4/negwind      !-Z direction
cmshel,none
cmshel,s,pwind
esla,s
bfe,all,js,3,current*turns*4/poswind      !+Z direction

!phase=ac (3)

*elseif,phase,eq,3

cmshel,s,nwind
esla,s
bfe,all,js,3,-current*turns*4/negwind      !-Z direction
cmshel,none
cmshel,s,pwind
esla,s
bfe,all,js,3,current*turns*4/poswind      !+Z direction

*endif

```

## C.5. FRSRM

This code differs in the assignment of variables, winding area selection and assignment of current sheets. These different sections of the code are listed below.

### A. Assignment of Dimensions and Other Values

```

!This file calculates an electromagnetic solution of the SRM
!This is the file for the 12/8 SRM using fractional windings
!The correct areas are selected to get the windings for the phase a,b,c
!so that body-force current load can be applied to that area to get
!frsrm operation as desired.
!The areas are pwnda,nwnda-----> Phase a
!                pwndb,nwndb-----> Phase b
!                pwndc,nwndc-----> Phase c
!Written by: Shyam S.R.
!on: 11/6/99

!variables of the motor geometry:

sor=0.1786                !stator outside radius
smr=0.1567                !stator middle radius
sir=0.1195                !stator inside radius
ror=0.1183                !rotor outside radius
rmr=0.0828                !rotor middle radius
sr=0.0583                !shaft radius
spw=15                    !stator pole width
rpw=17                    !rotor pole width

```

```

theta=-7.5           !position of the rotor with respect to the stator (0
- -22.5)
nsp=12               !number of stator poles
nrp=nsp-4            !number of rotor poles
cww=360/nsp-spw      !copper winding width
iagw=360/nrp-rpw     !inner airgap width
mdepth=0.2366       !depth of the motor
currenta=136.6174    !current applied to the phase a -Make 0 for Quasi
currentb=136.6174    !current applied to the phase b
currentc=-136.6174   !current applied to the phase c
turns=12             !number of windings

```

## B. Selection of Winding Areas

```
!windings
```

```
!phase=a
```

```
!negative copper windings of interest
```

```

asel,s,loc,x,sir,smr
asel,r,loc,y,spw/2+cww/4
asel,a,loc,y,60-spw/2-cww/4
asel,a,loc,y,180+spw/2+cww/4
asel,a,loc,y,240-spw/2-cww/4
asel,r,loc,x,sir,smr
cm,nwinda,area
aatt,3,,1

```

```
!positive copper windings of interest
```

```

asel,s,loc,x,sir,smr
asel,r,loc,y,-30-spw/2-cww/4
asel,a,loc,y,-90+spw/2+cww/4
asel,a,loc,y,150-spw/2-cww/4
asel,a,loc,y,90+spw/2+cww/4
asel,r,loc,x,sir,smr
cm,pwinda,area
aatt,3,,1

```

```
!phase=b
```

```
!negative copper windings of interest
```

```

asel,s,loc,x,sir,smr
asel,r,loc,y,-spw/2-cww/4
asel,a,loc,y,120+spw/2+cww/4
asel,a,loc,y,180-spw/2-cww/4
asel,a,loc,y,-60+spw/2+cww/4
asel,r,loc,x,sir,smr
cm,nwindb,area
aatt,3,,1

```

```
!positive copper windings of interest
```

```

asel,s,loc,x,sir,smr
asel,r,loc,y,30+spw/2+cww/4
asel,a,loc,y,90-spw/2-cww/4
asel,a,loc,y,-150+spw/2+cww/4
asel,a,loc,y,-90-spw/2-cww/4
asel,r,loc,x,sir,smr

```

```

cm,pwindb,area
aatt,3,,1

!phase=c

!negative copper windings of interest

asel,s,loc,x,sir,smr
asel,r,loc,y,60+spw/2+cww/4
asel,a,loc,y,120-spw/2-cww/4
asel,a,loc,y,-120+spw/2+cww/4
asel,a,loc,y,-60-spw/2-cww/4
asel,r,loc,x,sir,smr
cm,nwindc,area
aatt,3,,1

!positive copper windings of interest

asel,s,loc,x,sir,smr
asel,r,loc,y,30-spw/2-cww/4
asel,a,loc,y,-30+spw/2+cww/4
asel,a,loc,y,150+spw/2+cww/4
asel,a,loc,y,-150-spw/2-cww/4
asel,r,loc,x,sir,smr
cm,pwindc,area
aatt,3,,1

!calculate the area of the positive windings and
!assign the value to the variable poswind

cmsel,s,pwinda
asum
*get,poswinda,area,,area

!calculate the area of the negative windings and
!assign the value to the variable negwind

cmsel,s,nwinda
asum
*get,negwinda,area,,area

!calculate the area of the positive windings and
!assign the value to the variable poswind

cmsel,s,pwindb
asum
*get,poswindb,area,,area

!calculate the area of the negative windings and
!assign the value to the variable negwind

cmsel,s,nwindb
asum
*get,negwindb,area,,area

!calculate the area of the positive windings and
!assign the value to the variable poswind

cmsel,s,pwindc
asum

```

```
*get,poswindc,area,,area
```

```
!calculate the area of the negative windings and  
!assign the value to the variable negwind
```

```
cmsel,s,nwindc
```

```
asum
```

```
*get,negwindc,area,,area
```

### *C. Assignment of Current Sheets*

```
!unselect all components
```

```
cmsel,none
```

```
!select the components of the SRM that a current density will be  
applied
```

```
!to and then select all elements of those components. After this, the  
!bfe command applies the current density to the selected elements.
```

```
!phase=a
```

```
cmsel,s,nwinda
```

```
esla,s
```

```
bfe,all,js,3,-currenta*turns*4/negwinda    !-Z direction
```

```
cmsel,none
```

```
cmsel,s,pwinda
```

```
esla,s
```

```
bfe,all,js,3,currenta*turns*4/poswinda    !+Z direction
```

```
!phase=b
```

```
cmsel,s,nwindb
```

```
esla,s
```

```
bfe,all,js,3,-currentb*turns*4/negwindb    !-Z direction
```

```
cmsel,none
```

```
cmsel,s,pwindb
```

```
esla,s
```

```
bfe,all,js,3,currentb*turns*4/poswindb    !+Z direction
```

```
!phase=c
```

```
cmsel,s,nwindc
```

```
esla,s
```

```
bfe,all,js,3,-currentc*turns*4/negwindc    !-Z direction
```

```
cmsel,none
```

```
cmsel,s,pwindc
```

```
esla,s
```

```
bfe,all,js,3,currentc*turns*4/poswindc    !+Z direction
```

### **C.6. Full-Pitch SRM**

Again, this code differs in the assignment of variables, winding area selection and assignment of current sheets. These different sections of the code are listed below.

#### A. Assignment of Dimensions and Other Values

```
!This file calculates an electromagnetic solution of the SRM
!This is the file for the 12/8 SRM using fractional windings
!The correct areas are selected to get the windings for the phase a,b,c
!so that body-force current load can be applied to that area to get
!frsrm operation as desired.
!The areas are pwnda,nwnda-----> Phase a
!           pwndb,nwndb-----> Phase b
!           pwndc,nwndc-----> Phase c
!Written by: Shyam S.R.
!on: 11/6/99

!variables of the motor geometry:

sor=0.1721           !stator outside radius
smr=0.1502           !stator middle radius
sir=0.1195           !stator inside radius
ror=0.1183           !rotor outside radius
rmr=0.0828           !rotor middle radius
sr=0.0583            !shaft radius
spw=15               !stator pole width
rpw=17               !rotor pole width
theta=-15            !position of the rotor with respect to the stator (0
- -22.5)
nsp=12                !number of stator poles
nrp=nsp-4             !number of rotor poles
cww=360/nsp-spw       !copper winding width
iagw=360/nrp-rpw      !inner airgap width
mdepth=0.2366         !depth of the motor
current=136.6174      !current applied to the phase a
turns=12              !number of turns per pole
```

#### B. Selection of Winding Areas

```
!windings

!positive copper windings of interest

asel,s,loc,x,sir,smr
asel,r,loc,y,spw/2+cww/4
asel,a,loc,y,30-spw/2-cww/4
asel,a,loc,y,90-spw/2-cww/4
asel,a,loc,y,60+spw/2+cww/4
asel,a,loc,y,180+spw/2+cww/4
asel,a,loc,y,210-spw/2-cww/4
asel,a,loc,y,270-spw/2-cww/4
asel,a,loc,y,240+spw/2+cww/4
asel,r,loc,x,sir,smr
cm,pwind,area
aatt,3,,1

!negative copper windings of interest

asel,s,loc,x,sir,smr
asel,r,loc,y,-spw/2-cww/4
```

```

asel,a,loc,y,-30+spw/2+cww/4
asel,a,loc,y,90+spw/2+cww/4
asel,a,loc,y,120-spw/2-cww/4
asel,a,loc,y,180-spw/2-cww/4
asel,a,loc,y,150+spw/2+cww/4
asel,a,loc,y,-90+spw/2+cww/4
asel,a,loc,y,-60-spw/2-cww/4
asel,r,loc,x,sir,smr
cm,nwind,area
aatt,3,,1

```

!non interest copper windings

```

asel,s,loc,x,sir,smr
asel,r,loc,y,-180+spw/2+.25*cww
*do,i,1,nsp
n=-180+spw/2+.25*cww+(360/nsp)*i
asel,a,loc,y,n,n
*enddo
asel,a,loc,y,-180+spw/2+.75*cww
*do,i,1,nsp
n=-180+spw/2+.75*cww+(360/nsp)*i
asel,a,loc,y,n,n
*enddo
asel,r,loc,x,sir,smr
cmsel,u,pwind
cmsel,u,nwind
cm,owind,area
aatt,3,,1

```

!calculate the area of the positive windings and  
!assign the value to the variable poswind

```

cmsel,s,pwind
asum
*get,poswind,area,,area

```

!calculate the area of the negative windings and  
!assign the value to the variable negwind

```

cmsel,s,nwind
asum
*get,negwind,area,,area

```

### *C. Assignment of Current Sheets*

!unselect all components

```
cmsel,none
```

!select the components of the SRM that a current density will be applied  
!to and then select all elements of those components. After this, the  
!bfe command applies the current density to the selected elements.

```

cmsel,s,nwind
esla,s
bfe,all,js,3,-current*turns*8/negwind    !-Z direction
cmsel,none

```

```

cmsel,s,pwind
esla,s
bfe,all,js,3,current*turns*8/poswind    !+Z direction

```

## C.7. Writing Code for Automated Looping

Using ANSYS™, it is possible to set up the code to perform automated looping with variation of file variables in each run. The code should be re-written as a *.mac* file and is run under the control of another file that invokes the *.mac file*. The variables that must be varied are re-named as arg1, arg2,....., arg18.

For example, the 6/4 ANSYS code file is re-written as a *.mac* file *srminduc.mac* to determine the flux-linkage at different rotor positions and phase current values. At the start of the *.mac* file, the “/clear,nostart” operation is performed. A file is opened in the controlling file using the command \*CFOPEN and the calculated values during each run are written into it using the \*VWRITE command. In the *.mac* file, arg1 is the rotor position and arg2 and arg3 are the currents in the working and leading phases, respectively.

### Controlling File *srmc*

```

*CFOPEN,linkage86,out,/home/ssr2/

arg3=0

*DO,arg1,-30,0,2
*DO,arg2,13.5,135,13.5
srminduc,arg1,arg2,arg3 !srminduc.mac invoked
*ENDDO
*ENDDO
!This file enables calculation of the solution for 8/6 SRM characteristics
!to determine the coenergy and flux-linkages which can be used to get a
!multi-phase model of the SRM
!At the end of calculation for each arg1 value, *VWRITE command is used
!to write arg1,arg2,arg3,coenergy and torque values to file linkagesfp.out

!Written by Shyam S.R. on 11/11/99

```

### Skeleton of *.mac* file *srminduc.mac*

```

/clear,nostart

```

!This file calculates an electromagnetic solution of the SRM

!Written by: Shyam S.R.

!on: 11/11/99

!variables of the motor geometry:

```
sor=0.1851    !stator outside radius
smr=0.1524    !stator middle radius
sir=0.1195    !stator inside radius
ror=0.1183    !rotor outside radius
rmr=0.0828    !rotor middle radius
sr =0.0477    !shaft radius
spw=22.5      !stator pole width
rpw=24.5      !rotor pole width
nsp=8         !number of stator poles
nrp=nsp-2     !number of rotor poles
cww=360/nsp-spw    !copper winding width
iagw=360/nrp-rpw    !inner airgap width
mdepth=0.2366    !depth of the motor
turns=25        !number of windings
```

!calculate the angle from the origin to the top of the  
!small angle on the pole of the rotor

```
!numerator = num
num=tan(5*3.14159265/180)*(ror-rmr)+ror*sin(rpw/2*3.14159265/180)
phi=asin(num/rmr)*180/3.14159265
```

!enter the preprocessor of the program

/prep7

!define the element types to be used

et,1,plane13,0

.  
.  
.

!keypoints of the stator poles and copper windings

```
k,,sir,spw/2
k,,smr,spw/2
k,,sir,spw/2+cww/2
k,,smr,spw/2+cww/2
k,,sir,spw/2+cww
k,,smr,spw/2+cww
ksel,s,,,1,6
kgen,nsp,all,,,360/nsp
```

!keypoints of the rotor and shaft

```
k,,rmr,arg1-phi
k,,ror,arg1-rpw/2
k,,ror,arg1+rpw/2
k,,rmr,arg1+phi
ksel,s,,,nsp*6+1,nsp*6+4
kgen,nrp,all,,,360/nrp
```

!lines for the rotor poles

```

csys,0
1,6*nsp+1,6*nsp+2
1,6*nsp+3,6*nsp+4
1,6*nsp+5,6*nsp+6
1,6*nsp+7,6*nsp+8
1,6*nsp+9,6*nsp+10
1,6*nsp+11,6*nsp+12
1,6*nsp+13,6*nsp+14
1,6*nsp+15,6*nsp+16
1,6*nsp+17,6*nsp+18
1,6*nsp+19,6*nsp+20
1,6*nsp+21,6*nsp+22
1,6*nsp+23,6*nsp+24
csys,1

!select all keypoints of the SRM

ksel,all
kplot,all

!generate areas of the SRM

!areas of the stator ring

pcirc,smr,sor,0,spw
agen,2*nsp,all,,,360/(2*nsp)

.

.

.

cmsel,none

!select the components of the SRM that a current density will be applied
!to and then select all elements of those components. After this, the
!bfe command applies the current density to the selected elements.

cmsel,s,nwind2
esla,s
bfe,all,js,3,-arg2*turns*2/negwind    !-Z direction
cmsel,none
cmsel,s,pwind2
esla,s
bfe,all,js,3,arg2*turns*2/poswind      !+Z direction

cmsel,s,nwind3
esla,s
bfe,all,js,3,-arg3*turns*2/negwind    !-Z direction
cmsel,none
cmsel,s,pwind3
esla,s
bfe,all,js,3,arg3*turns*2/poswind      !+Z direction

!far-field boundary conditions

.

.

.

```

```

/nopr
parsav,all,sasimac
esel,s,mat,,1,4,1
etable,sene,sene
/out,scratch
ssum
/out
*get,energy,ssum,,item,sene
/gopr
menergy=energy*mdepth

esel,s,mat,,1,4,1
senergy,1,0
coen=c_eng*mdepth

esel,s,mat,,1,4,1
senergy,0,0
ener=s_eng*mdepth

!calculate the airgap torque

allsel
cmsel,s,airgap
esla
torqc2d,ror+((sir-ror)/2),100
agt=torque*mdepth

*VWRITE,arg1,arg2,arg3,agt,coen,ener
(F6.1,F6.1,F8.1,F8.2,F9.5,F9.5)

finish

```

## SIMULINK MODELS

### D.1 SIMULINK Model for the SRM using ANN

This Section describes the changes to the SIMULINK™ implementation of the SRM single-phase model in [1] when using the ANN to account for the multi-phase excitation. The ANN suggested in this Report map the rotor position with respect to a phase, the current in the same phase (called the working phase) and the one ahead of it in the direction of rotation (called the leading phase) to the electromagnetic torque and mutual flux interaction functions. The overall system and the SIMULINK blocks for torque and mutual flux computations are shown in Figures D.1, D.2 and D.3 for the simulation of a four-phase 8/6 SRM.

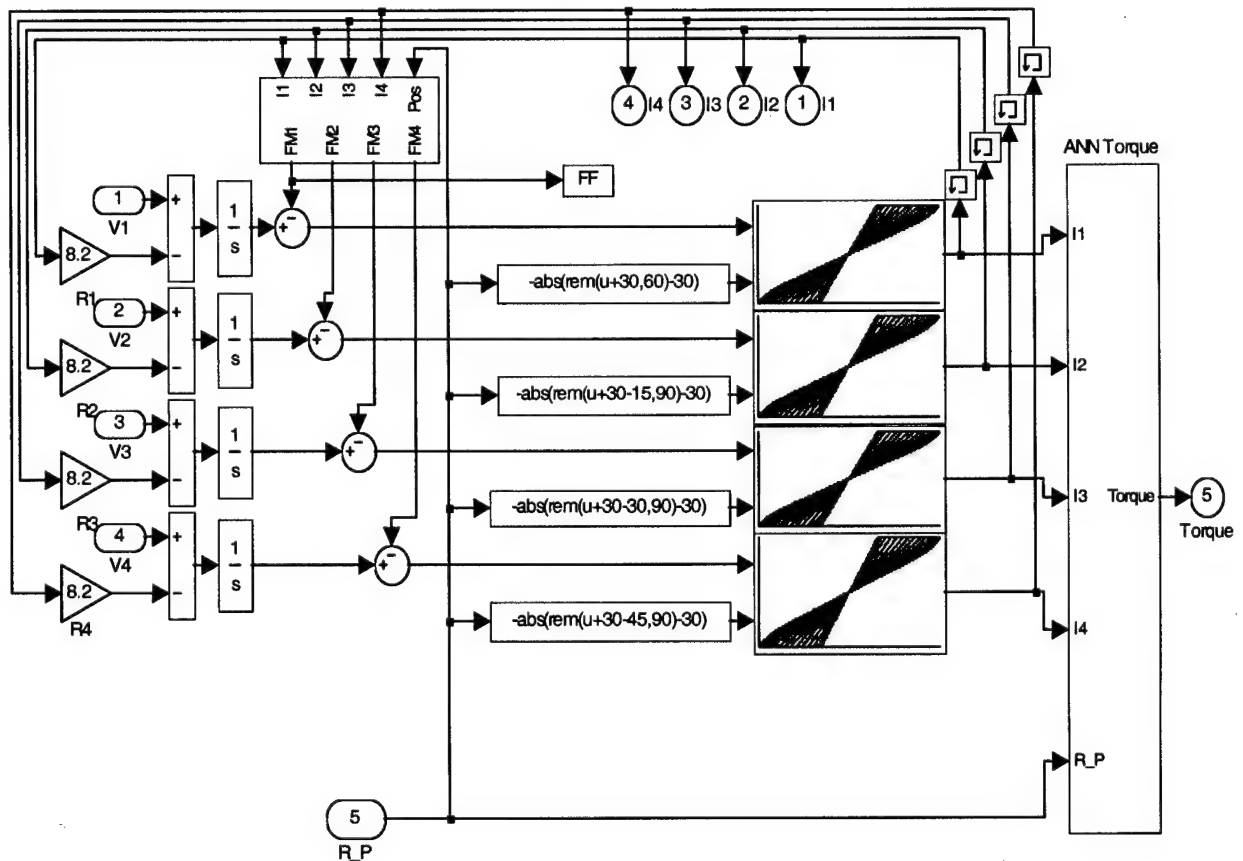


Figure D.1 SIMULINK<sup>TM</sup> model of the four-phase 8/6 SRM.

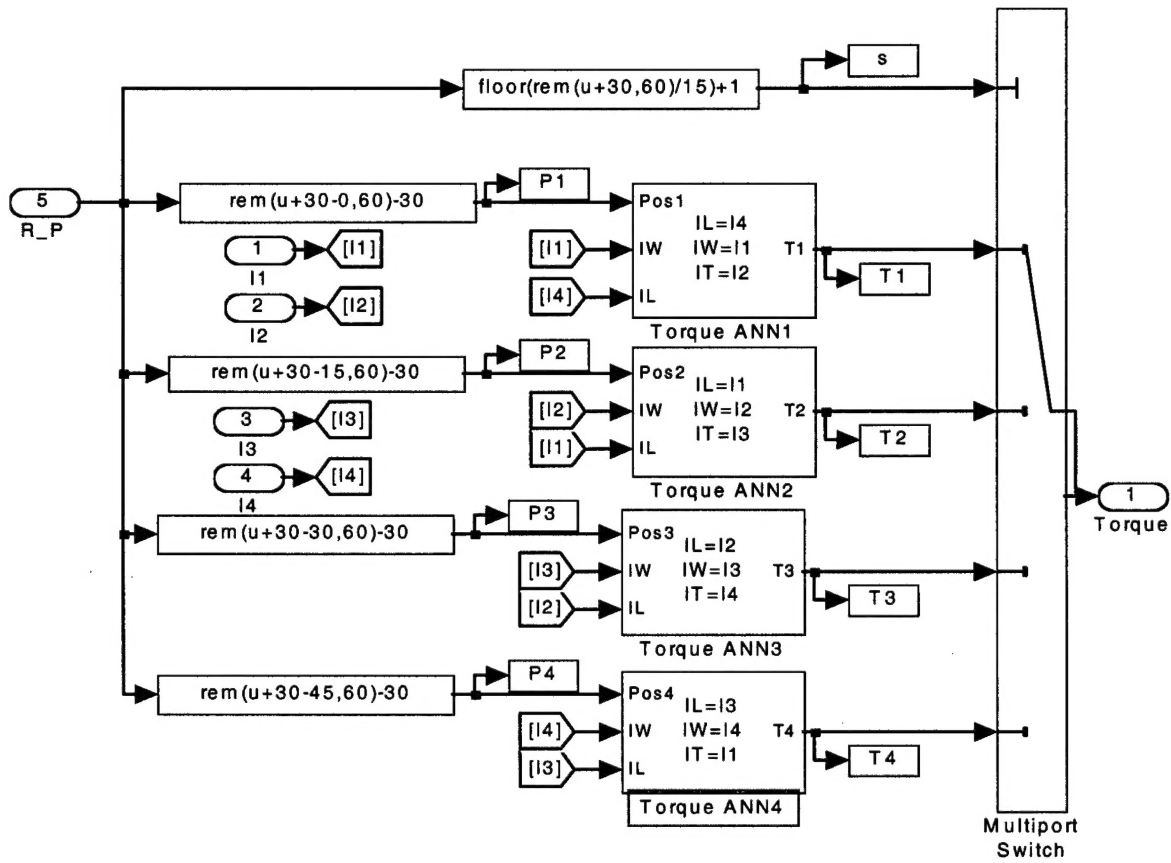


Figure D.2 ANN-based torque computation block.

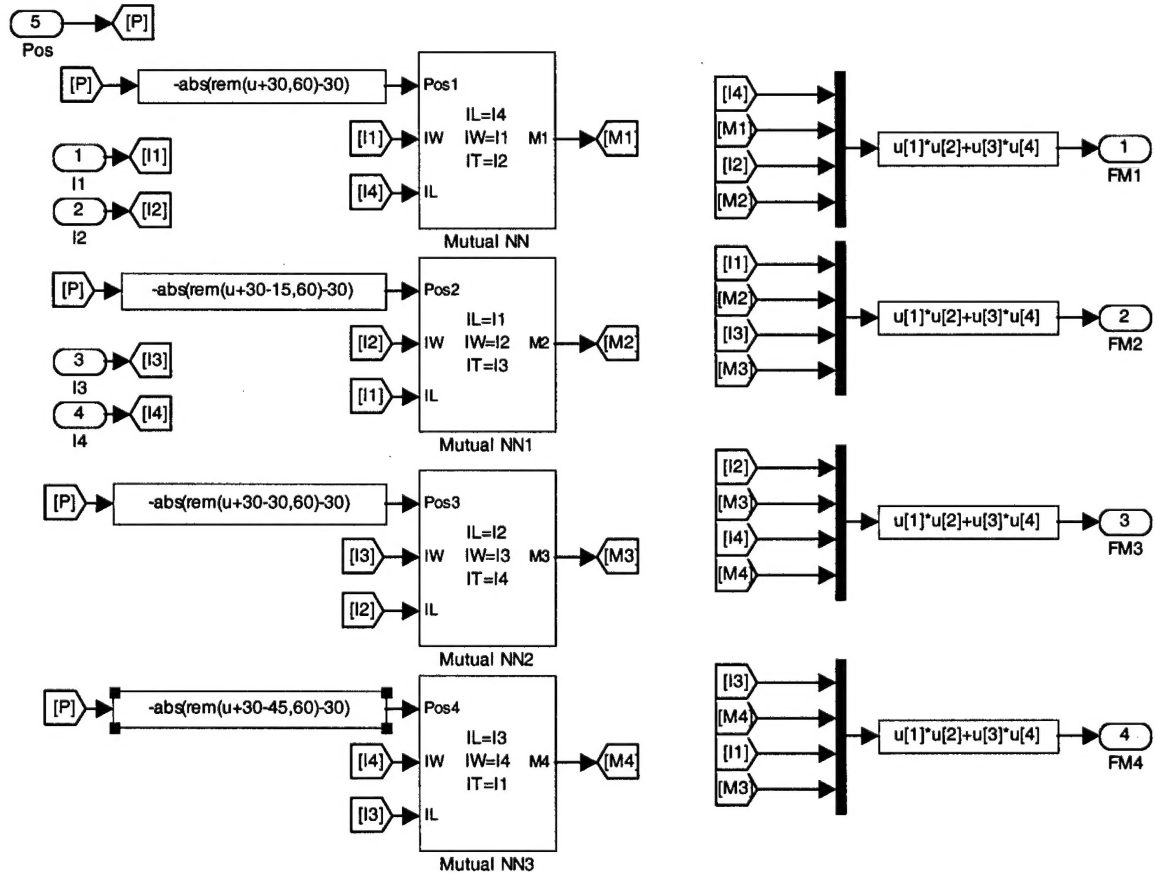


Figure B.3 The ANN-based mutual flux computation block.

In the development of this simulation approach, the assumption is that more than two phases do not operate simultaneously. The torque computation block uses selective switching at the output to select the phase which is currently the working phase and derive the torque output with respect to that phase. In Figure D.3, FM1, FM2, FM3 and FM4 denote respectively the mutual flux component of the net flux for each phase. Hence, this component is used to correct the phase flux for the mutual interactions.

## D.2 SIMULINK™ Model for On-Line Torque Estimation

The simulation of the on-line torque estimation system is based on measurements of SRM SIMULINK model variables. The phase current  $i_k$ , phase rotor position  $\theta_k$  and the terminal voltage  $v_k$  are measured quantities. The SRM model of [1] has one time step of delay between the terminal voltage and actual phase current. To account for this, a delayed value of the terminal voltage is considered in the estimation system. The shift register is used to store sampled values over several time steps as determined by a buffer size specified in the initialization stage. Several values of the buffer size were tried out to see the performance of the estimation system when it is trained to greater accuracy near the current operating point of the SRM. However, it was found that a buffer size of 1 results in the best performance since the ANN is able to train to represent the system completely. Figure D.4 shows the portion of the model that is used for on-line estimation. The MATLAB function used for the ANN and its inversion is also included.

### MATLAB Function for ANN Training and Inversion in the Adaptive Torque Estimation Simulation:

```
function [out]=randcots2ialt(inik,inik1,inthk,inthk1,inv1)
global net net1 bufsize vw numIn
T= 5.0e-5 ;           %the sampling time
Inp=4;                %number of inputs
totB=numIn+1;
for i=1:bufsize
    P(1,i)=inik(i);
    P(2,i)=inv1(i);
    P(3,i)=inthk(i);
    P(4,i)=inthk(i)-inthk1(i);
```

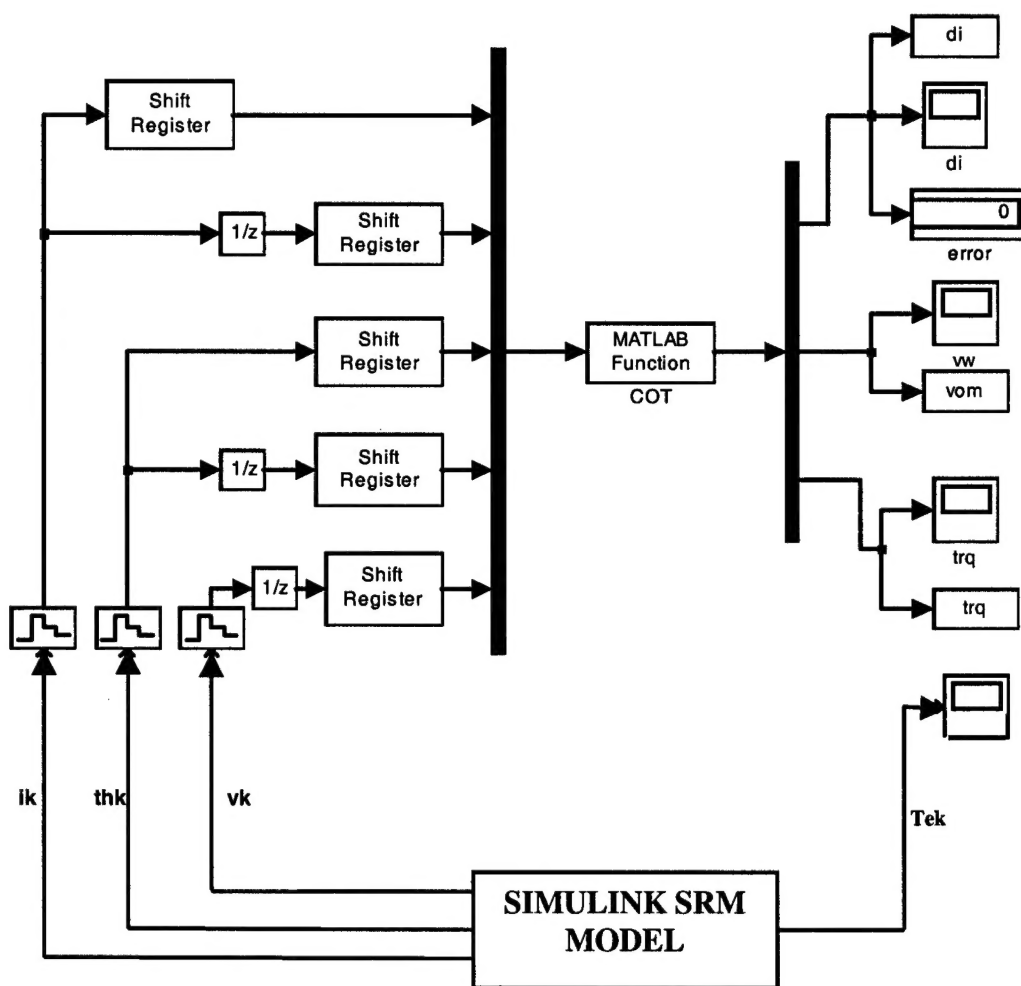


Figure D.4 On-line torque estimation system

```

Tr(i)=inik(i)-inik1(i);
end
net=train(net,P,Tr);

B=cell2mat(net.b);

test(1)=inik(bufsize);
test(2)=inv1(bufsize);
test(3)=inthk(bufsize);
test(4)=inthk(bufsize)-inthk1(bufsize);

%Determining the network output for the last case
iw=sim(net,test'); % Rate of current rise

f1=200000;
if vw>5
    min=vw-5;
    max=vw+5;
elseif vw < 1
    min=1;

```

```

        max=6;
    else
        min=vw
        max=vw+5;
    end
    for i=min:0.25:max
        test(1)=inik(bufsize);
        test(2)=i-1;
        test(3)=inthk(bufsize);
        test(4)=inthk(bufsize)-inthk1(bufsize);
        f=sim(net,test');
        if abs(f)<f1
            vw=i-1;
            f1=abs(f);
        end
    end
end

Tr=vw*inik(bufsize)*180*T/(inthk(bufsize)-inthk1(bufsize))/pi;

out=[iw,vw,Tr];

```

## References

- [1] R.M.Schupbach, Switched-Reluctance Motors: Dynamic Simulation Techniques, M.S. Thesis, Department of Electrical Engineering, University of Arkansas, July 2000.